CHALLENGES AND CURRENT QUESTIONS IN COSMOLOGY

by

Tilek Zhumabek

A Thesis Submitted to the Faculty of the

DEPARTMENT OF PHYSICS

In Partial Fulfillment of the Requirements
For the Degree of

DOCTOR OF PHILOSOPHY IN PHYSICS

In the School of Sciences and Humanities

NAZARBAYEV UNIVERSITY

2025

NAZARBAYEV UNIVERSITY, SCHOOL OF SCIENCES AND HUMANITIES

As members of the thesis committee, we certify that we have read the thesis prepared by Tilek Zhumabek entitled

CHALLENGES AND CURRENT QUESTIONS IN COSMOLOGY

and recommend that it be accepted as fulfilling the thesis requirement for the degree of Doctor of Philosophy in Physics.

_____ Date: May 5, 2025

Prof. Daniele Malafarina, Lead Supervisor
Nazarbayev University, Kazakhstan

_____ Date: May 5, 2025

Prof. Ernazar Abdikamalov, Internal Co-Supervisor
Nazarbayev University, Kazakhstan

_____ Date: May 5, 2025

Prof. Eric V. Linder, External Co-Supervisor
University of California, Berkeley, USA

_____ Date: May 5, 2025

Prof. Michael Good, Internal Examiner
Nazarbayev University, Kazakhstan

_____ Date: May 5, 2025

Prof. Salvatore Capozziello, External Examiner
Università di Napoli, Italy

Final approval and acceptance of this thesis is contingent upon the candidate's submission of the final copies of the thesis to the Department of Physics.

I hereby certify that I have read this thesis prepared under my direction and recommend that it be accepted as fulfilling the thesis requirement.

_____ Date: May 5, 2025

Thesis Director: Daniele Malafarina

Contents

List of Figures

List of Figures

Abstract

The last several decades proved to be a golden age for cosmology. From the observational front, we have significant breakthroughs including the discovery of Cosmic Microwave Background (CMB), detection of late time cosmic acceleration, and the mapping of Large Scale Structure (LSS) formation. From the theoretical front, a robust Λ-dominated Cold Dark Matter (ΛCDM) model was developed to explain those phenomena with remarkable precision. However, there remain considerable challenges and questions to address within each front. On the one hand, there are persistent tensions in different observational datasets such as σ_8 tension arising from the conflicting measurements of the amount of matter clustering in the universe. On the other hand, theoretical frameworks still grapple in explaining the true nature of the dark sectors of ΛCDM model: dark energy and dark matter. This thesis consists of three separate studies that aim to address these issues by investigating the shared mechanism of two cosmic accelerations, the dark matter properties, and the σ_8 tension.

In the first study, we explore a quintessential inflation within an α-attractor formalism that connects inflation with dark energy. Cosmic acceleration in the early universe, known as inflation, is essential to explain the observed properties of CMB and predicts the existence of primordial gravitational waves. Cosmic acceleration in the late universe, driven by dark energy, is again essential for understanding the universe's geometry and structure formation. We demonstrate a robust relation between the present value of dark energy equation of state w_0 and the strength of the primordial gravitational waves r, $1 + w_0 \approx 4/(3N^2 r)$, valid for a broad range of initial conditions. With the chosen α-attractor potential, we identify the scalar field as the thawing field thus explaining the large time gap between the two cosmic accelerations and revealing a tight relation $w_a \approx -1.53(1 + w_0) \approx -0.2\,(4 \times 10^{-3}/r)$ between the observables of dark energy and inflation. Thus, we established a medium where a likelihood of observing a dynamical

dark energy $w_a \neq 0$ increases at the expense of detecting primordial gravitational wave r and vice versa.

The second study examines deviations of dark matter properties from the standard model. ΛCDM assumes the dark matter to cluster with the same gravitational strength as baryons and evolve with the pressureless equation of state. However, any deviations in both characteristics, if observed by future cosmic growth measurements, may shed light on the origin of the longstanding tensions. We take a model-independent approach by binning the deviations in redshift and computing the constraints by three different cosmic surveys, which combined, can cover $z = [0, 4]$. The analysis shows $3 - 14\%$ and $3 - 23\%$ level constraints on the clustering and equation of state deviations, respectively. In obtaining these results, we neglected the general sound speed along with the viscous sound speed and leave these effects for future work.

The third study investigates the implication of a modified gravity model on the structure growth, in particular, on σ_8 tension. With this model, we derived the modified background quantities and perturbation equation. Using redshift space distortion data, we performed MCMC analysis, successfully demonstrating the decrease in the σ_8 tension from 3σ, as observed between the Planck mission and galaxy redshift measurements, to 1σ. It must be stressed that any proposal to alleviate one tension should not aggravate the other. However, we left the model implications on the Hubble tension for future work.

This thesis explores theoretical and observational challenges by offering new insights into the cosmic acceleration, dark matter properties, and persistent σ_8 tension. Together, we believe these studies may contribute a glimpse of comprehension to the mysteries of our universe and possibly point towards new research directions.

Acknowledgment

This turning point in my career presents me a brief and proper time to write down my sincere gratitude to all those who happened to be in my past "PhD light cone", especially to those who have guided, inspired, and supported me.

First and foremost, I am grateful to have Prof. Eric V. Linder as my supervisor who introduced me to cosmology. Under his guidance, I had the privilege to co-author two research articles within a year. His style of preparing a student to dive into new topics with rigor and understanding was challenging and rewarding at the same time. I still vividly remember my little "eurika" moments while studying phase space dynamics of quintessence. An integral part of this story is Dr. Mikhail Denissenya, who was immensely helpful in navigating through technical details of the research and I owe much of my success to his critical intermediary role.

Special thanks goes to my leading supervisor, Prof. Daniele Malafarina, whose courses were most enjoyable experiences of my Master's and PhD studies. Thanks to him and Dr. Hrishikesh Chakrabarty, I completed my third article. Beyond an academic role, Prof. Malafarina is genuinely kind and supportive person which makes the collaboration with him a pleasure.

I am deeply indebted to my co-supervisor, Prof. Ernazar Abdikamalov for providing much of the support in technical aspects such as, securing funding for my projects and providing access to technical resources like computers. He demonstrated resourcefulness in offering guidance whenever I had requests for advice.

A special mention in my acknowledgment is warranted to my colleague, peer, and roommate, Azamat Mukhamediya. We often had a long, late-night discussions about many things (if not everything) which led to the successful interdisciplinary collaboration on two projects. I am grateful for his friendship and support.

Finally, I wish to extend my heartfelt gratitude to my parents for the sacrifices they made to make my PhD journey possible. I am also thankful to my friends whose companionship makes me feel a lucky person to have them as friends.

Declaration

I hereby declare that this thesis is my own original work and has been written by me in its entirety. It has not been submitted previously, in whole or in part, to qualify for any other academic award.

This work is based on the following three research papers authored by me, with co-authors:

1. **Connecting primordial gravitational waves and dark energy**
   Tilek Zhumabek, Mikhail Denissenya, and Eric V. Linder, *Journal of Cosmology and Astroparticle Physics*, Vol. 2023, No. 09, Page 013 (2023).

2. **Model-independent dark matter properties from cosmic growth**
   Tilek Zhumabek, Mikhail Denissenya, and Eric V. Linder, *Journal of Cosmology and Astroparticle Physics*, Vol. 2024, No. 02, Page 018 (2024).

3. **Running gravitational constant induced dark energy as a solution to σ_8 tension**
   Tilek Zhumabek, Azamat Mukhamediya, Hrishikesh Chakrabarty, and Daniele Malafarina, *arXiv:2411.05965* (2024).
   Available online: https://arxiv.org/abs/2411.05965.

Chapter 2 is based on the first research article. This chapter builds upon the original publication by extending its content to include detailed derivations, discussions, and additional results.

Chapter 3 is built upon the second research paper.

Chapter 4 draws upon the results of the third paper which has been submitted to *[Physical Review D]* and is currently under review at the time of writing this thesis. This chapter extends the original work by including additional material in the Theory section.

All the figures used for illustration purposes are properly credited in the associated captions.

Signed:  Date: May 7, 2025

Chapter 1

Introduction

Current understanding of the cosmos has its challenges and questions. Investigating them prompts us to consider the key developments in the history of cosmology. In this vein, we should mention that the earliest scientific form of this discipline is known as "celestial mechanics" which focused on the study of the heavens. The radical change in the celestial mechanics happened with Newton's discovery of the law of universal gravitation in 1687 uniting the stellar and terrestrial phenomena. However, it is widely believed that modern cosmology began in 1917 with Einstein's last modification of his new theory of gravity [1]. General relativity enhanced the astronomers' ability to study distant objects paving the way for the era of observational cosmology and culminating in Edwin Hubble's discovery of the universe's expansion as predicted by George Lemaitre and described by Alexander Friedmann[2]. This observation inspired the Big Bang model in the 1930s [3]. Not long after, the discovery of the cosmic microwave background (CMB) confirmed the prediction of the Big Bang model [4]. These dramatic changes transformed cosmology from a speculative science into a predictive science. Since then, cosmological measurements have seen a consistent increase in precision. These advances include the CMB measurements by satellite observations (COBE[5], WMAP[6–8], Planck [9]) and the ground-based telescopes (Atacama Cosmology Telescope [10], BICEP/Keck [11], South Pole Telescope [12]). Additionally, structure growth measurements such as those based on the Lyman-α forest [13–16], galaxy clustering [17] and weak lensing measurements [18–20], the evidence of the universe's accelerated expansion from Type Ia supernovae [21, 22] and Baryon Acoustic Oscillation (BAO) measurements [23, 24], all have fundamentally reshaped our understanding of the universe's origin, evolution, composition, and ultimate fate.

Currently, we have the standard ΛCDM model that exhibits strong agreement with all the cosmological measurements. It is a framework that includes a cosmological constant Λ to account for dark energy, cold dark matter to explain the unseen matter, and general relativity (GR) as the theory of gravity. These few assumptions were enough to explain the origin of CMB, galaxy distributions, and the expansion history of the universe. According to this model, small inhomogeneity ($\sim 10^{-5}$ level) in the CMB power spectrum is attributed to tiny quantum fluctuations during the early universe which were stretched apart by the exponential expansion of the universe. This period is known as inflation [25, 26]. However, what happens during inflation is beyond the scope of ΛCDM. An entirely new mechanism and a new matter are attributed to cause this exponential cosmic expansion. From the ΛCDM's perspective, inflation only provides initial conditions to solve the evolution equations. These initial conditions or initial seeds will grow, under gravitational instability, into non-linear structures including galaxies and galaxy clusters [27].

Despite the success of ΛCDM in interpreting the observational findings, it relies on indirectly detected ingredients. For instance, we still don't know the true nature of the cosmological constant and we can't explain its near-zero energy density observed by cosmic surveys. The fundamental essence of dark matter remains elusive with little understanding of its particle nature. While observational tensions, such as the discrepancy in the measured value of Hubble constant H_0 and inconsistencies in the growth measurements leading to σ_8 tension, might indicate that ΛCDM is incomplete. Inflation is often considered an extension to the standard model, but the reheating process which explains the transition to the hot Big Bang is not addressed in ΛCDM.

This thesis consists of three complementary research works that explore the above issues. In the ensuing Chapters, we will present the findings. But first, we shall introduce the standard cosmology, discuss the inflationary paradigm and dark energy, address dark matter properties and structure growth before concluding this Chapter with the outline of the thesis.

1.1 FRW Model As the Standard Cosmology

The foundation of the standard Big Bang theory is based on the cosmological principle that suggests homogeneity and isotropy on large scales. This assumption is elegantly encapsulated in the Robertson-Walker (RW) metric

$$ds^2 = -dt^2 + a^2(t)\left[\frac{dr^2}{1-kr^2} + r^2\left(d\theta^2 + \sin^2\theta\, d\phi^2\right)\right], \tag{1.1}$$

where s corresponds to the proper distance, t is the coordinate time, a is the scale factor representing the cosmic expansion, and (r, θ, ϕ) corresponds to the comoving coordinates. We have the dimensionless parameter k representing the spacetime curvature: if $k > 0$ we live in a closed universe, $k = 0$ corresponds to an infinite and flat universe, while $k < 0$ represents open and infinite universe. Substituting the metric (1.1) into the Einstein field equation gives the time-like (00) and space-like (ij) components which results in the Friedman's first and second equations, respectively

$$\begin{aligned} H^2 &= \frac{8\pi G}{3}\rho - \frac{k}{a^2}, \\ \frac{\ddot{a}}{a} &= -\frac{4\pi G}{3}\left(\rho + 3p\right), \end{aligned} \tag{1.2}$$

where $H = \dot{a}/a$ is the Hubble parameter, G represents Newton's constant, ρ and p are the energy density and pressure of the matter. Thus, if the condition $p < -\rho/3$ is satisfied then the expansion is accelerating ($\ddot{a} > 0$) with pressure p acting as an "anti-gravity" term. There is a type of "matter" that has a pressure that can oppose gravity's attraction. To see this, we observe, from Bianchi identity or energy conservation for a perfect fluid $T^{\mu}_{\nu,\mu} = 0$, the following density evolution equation

$$\dot{\rho} + 3H(\rho + p) = 0. \tag{1.3}$$

A matter with constant energy density implies $p = -\rho$ satisfying the condition for accelerated expansion and this matter is called cosmological constant Λ.

We can introduce an equation of state parameter $w = \frac{p}{\rho}$ between the energy density and pressure of the corresponding matter component. Then the dynamic behavior of matter will be captured in this single parameter. Table 1.1 displays the parameter evolutions of each matter component given the equation of states.

In cosmology, we often write the Friedmann's first equation as

$$H^2 = H_0^2\left[\Omega_r a^{-4} + \Omega_m a^{-3} + \Omega_k a^{-2} + \Omega_\Lambda\right], \tag{1.4}$$

Content	**EoS**	**a (Scale Factor)**	$\boldsymbol{\rho}$ **(Density)**	$\boldsymbol{H(t)}$
Matter	$w = 0$	$a \sim t^{2/3}$	$\rho \sim a^{-3}$	$H(t) = \frac{2}{3t}$
Radiation	$w = \frac{1}{3}$	$a \sim t^{1/2}$	$\rho \sim a^{-4}$	$H(t) = \frac{1}{2t}$
Λ	$w = -1$	$a = \exp(H(t - t_0))$	$\rho \sim$ const	$H(t) =$ const

Table 1.1: Evolution of scale factor, energy density, and Hubble parameter for different matter contents.

where the fractional energy density Ω is defined as the ratio of present matter energy density to the critical energy density $\Omega_i = \rho_i/\rho_{\text{crit}}$ (here $i = m, r, \Lambda$) with $\rho_{\text{crit}} = \frac{3H_0^2}{8\pi G}$. Given this concept, the flatness $k = 0$ is often represented by $\Omega_r + \Omega_m + \Omega_\Lambda = 1$, also consistent with the observations [8].

1.2 Inflation and Dark Energy

Inflation and dark energy are thought to be responsible for two major epochs in the universe's history. Inflation, a short period of rapid exponential expansion of spacetime driven by a high-energy vacuum state or scalar field, generates matter density perturbations and tensor perturbations of spacetime itself. The latter is believed to be the origin of the primordial gravitational waves, an important signature of inflation. Dark energy, on the other hand, started to dominate the matter content of the universe only recently, leading to an accelerated cosmic expansion and suppression of structure growth that had been going on since the onset of matter domination [28]. While the two epochs share a similar fate – accelerated expansion, they are separated by billions of years or by some 60 e-folds in expansion. As can be seen in Fig. 1.1, the dark energy-dominated epoch started only a few billion years ago marking the end of the matter-dominated epoch.

The idea of inflation originated during the 1980s to address several theoretical difficulties and experimental findings. In particular, the CMB discovery put stringent constraints on our understanding of the cosmic evolution by stipulating flat universe and homogeneous background temperature coming from the surface of last scattering. A new mechanism was needed to address these issues. In the following, we will consider these problems.

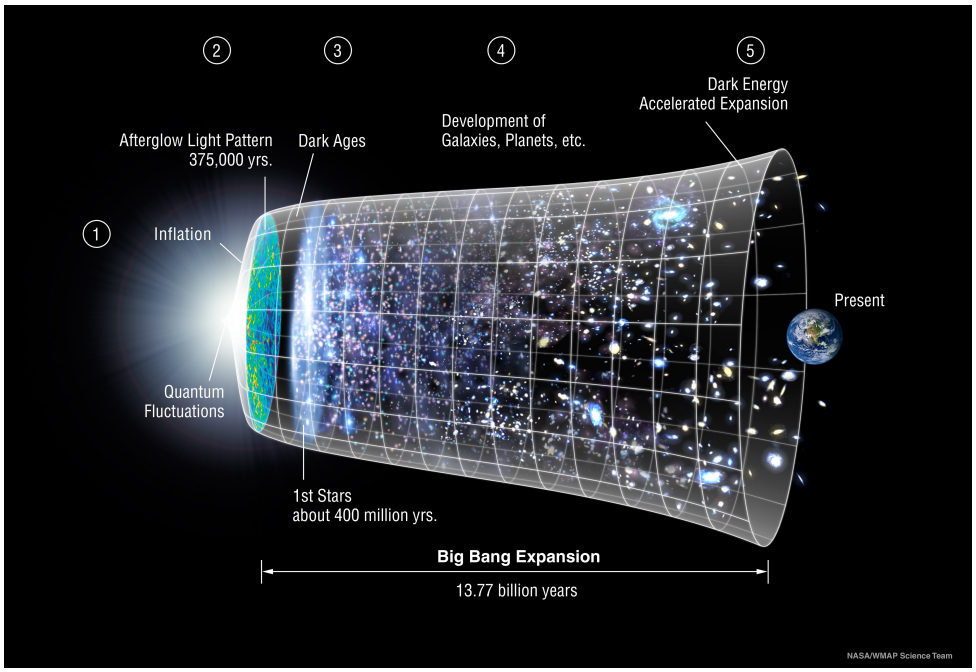

Figure 1.1: Brief history of universe. Figure taken from [29].

1.2.1 Problems In The Absence Of Inflation

1.2.1.1 Horizon Problem

The analysis of CMB temperature fluctuations showed a remarkable uniformity, the temperature anisotropy remaining below $\triangle T/T \sim 10^{-5}$ (Fig. 1.2). This presented a challenge since it meant the CMB photons coming at us from all parts of the sky were in thermal equilibrium in the past. However, this should not have happened according to the ΛCDM and to see why, we have to understand the concept of Hubble horizon. In standard cosmology, it is characterized by a scale beyond which objects recede faster than light. So the scales inside the Hubble horizon can interact, but the scales outside are, so to speak, "frozen". This is a crucial point to understand that the scales outside can't "talk to" scales inside. To give a quantitative picture, we want to show what fraction of the night sky corresponds to those scales that could interact to average out their temperature. In the following, we want to evaluate the angular size of portions of the CMB that were able to reach thermal equilibrium according to the ΛCDM model.

Let us introduce another horizon concept – the sound horizon. At early times, the universe was in a state of primordial plasma and photons couldn't travel far due to the Compton scattering off the free streaming electrons. In other words, photons were coupled to baryons to form a single medium subject to two competing forces: the gravitational

force trying to pull everything together and the pressure force of the medium trying to push everything apart. As a result, the system oscillates producing sound waves. The maximum distance these sound waves can travel until the time of recombination is usually referred to as the sound horizon. We can compute it in the comoving coordinate as

$$d_H = c_s \int_0^t \frac{dt'}{a(t')} = c_s \int_0^{\tau_{recom}} d\tau = c_s \tau_{recom} = \frac{1}{\sqrt{3}} \tau_{recom}. \tag{1.5}$$

where we used $c_s = 1/\sqrt{3}$ as the sound speed of the medium. The general formula to compute the sound speed is $c_s^2 = dp/d\rho$ and during radiation, we have $p_r = 1/3\rho_r$ substitution of which yields the above value. Next, we compute the comoving distance from the last scattering surface to the present time using the same formula with only different integral bounds,

$$d_{co} = \int_{\tau_{recom}}^{\tau_{now}} d\tau = \tau_{recom} = \tau_{now} - \tau_{recom}. \tag{1.6}$$

Once a comoving scale is given, we can project it onto the surface of the last scattering characterized by the angular scale,

$$\theta \simeq \frac{d_H}{d_{co}} = \frac{\frac{1}{\sqrt{3}}\tau_{recom}}{\tau_{now} - \tau_{recom}} \approx \frac{\tau_{recom}}{\sqrt{3}\tau_{now}}, \tag{1.7}$$

in using this formula, we assumed flat spacetime neglecting the curvature effect. As a further step, we notice that during the matter domination, the following relation holds between the scale factor, comoving time, and the temperature $a \sim \tau^2 \sim T^{-1}$. However, the matter domination lasted longer (with Λ starting to dominate only recently), so for rough estimation, we assume that relation to be valid even at present τ_{now}, to find

$$\theta_{\text{hor}} \simeq \frac{\tau_{recom}}{\sqrt{3}\tau_{now}} \simeq \frac{1}{\sqrt{3}} \left(\frac{T_0}{T_{recom}} \right)^{\frac{1}{2}} \simeq 1^\circ. \tag{1.8}$$

Thus, the patch of the universe at the CMB where any interaction could occur to produce thermal equilibrium accroding to ΛCDM amounts to just 1° angular scale in the night sky. In other words, two photons that were separated by more than $\theta > 1^\circ$ were not in causal contact. To account for this dilemma, some unknown processes must have occurred before the radiation epoch. The most simple solution one can provide is the shrinking Hubble horizon before the radiation era. This idea is the backbone of the cosmic inflation theory and according to it all the physical scales that we observe today were in a causal contact in the beginning of time. Fig. 1.3 shows the density fluctuation during

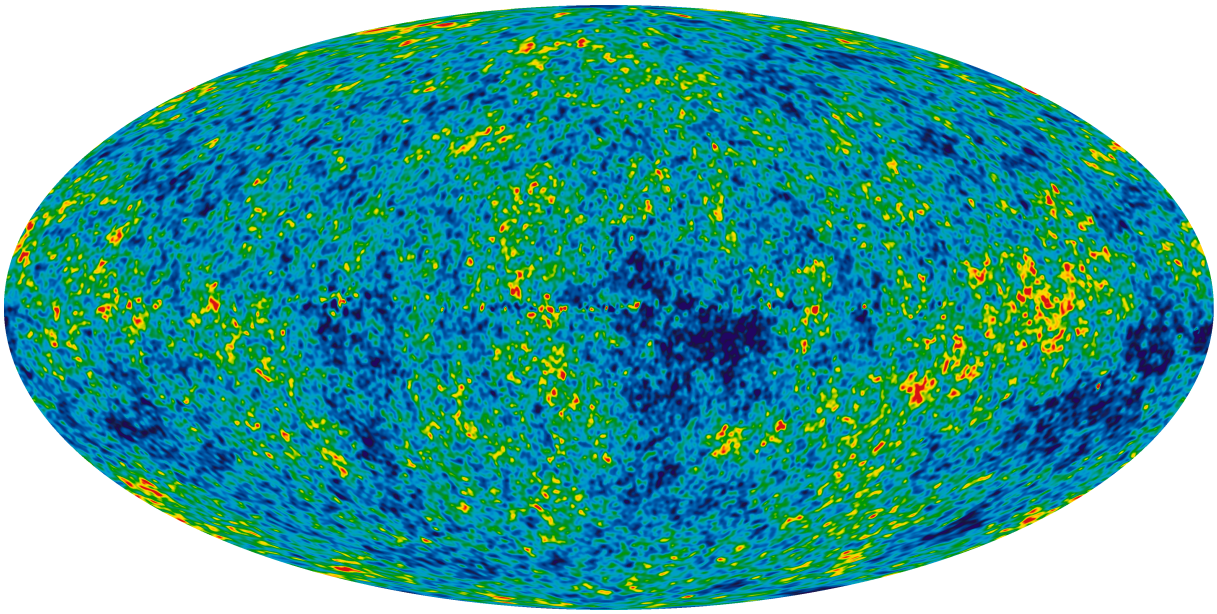

Figure 1.2: CMB Temperature Fluctuation. The picture was created from nine-year WMAP data [30].

inflation and its exit out of the shrinking Hubble horizon. Upon exiting, it freezes and re-enters the Hubble horizon once the radiation takes over. Therefore, all the scales were in causal contact during inflation giving rise to the uniform CMB temperature fluctuation.

To understand this argument more clearly, let us observe what happens to the co-moving particle horizon. This is a horizon or a region of space where two events sending signals to each other at a certain initial time t_i can receive it at a later time t. It can be written as an integral of the comoving Hubble horizon,

$$d_p = \int_{a_i}^{a} \frac{d \ln a'}{a' H(a')}, \tag{1.9}$$

where a_i is the initial scale factor, $\frac{1}{aH(a)}$ represents the comoving Hubble horizon. In the radiation epoch $H \propto a^{-2}$, the integral in Eq. 1.9 converges when taking the limit $a_i \to 0$. This means we can find a scale larger than the horizon since the latter is finite as shown in Fig. 1.3. However, notice that if H decreases more slowly than a^{-1}, the integral diverges resulting in an infinite horizon. In turn, this allows us to speculate that all scales were in causal contact before radiation. Assuming a power law expansion $a \propto t^p$, we would have

$$H = \frac{p}{t} \propto a^{-1/p}, \tag{1.10}$$

which transforms the above integral as

$$d_p \propto \int_{a_i}^{a} \frac{da'}{a'^{2-1/p}} \propto \frac{1}{a'^{1-1/p}} \Big|_{a_i}^{a}, \tag{1.11}$$

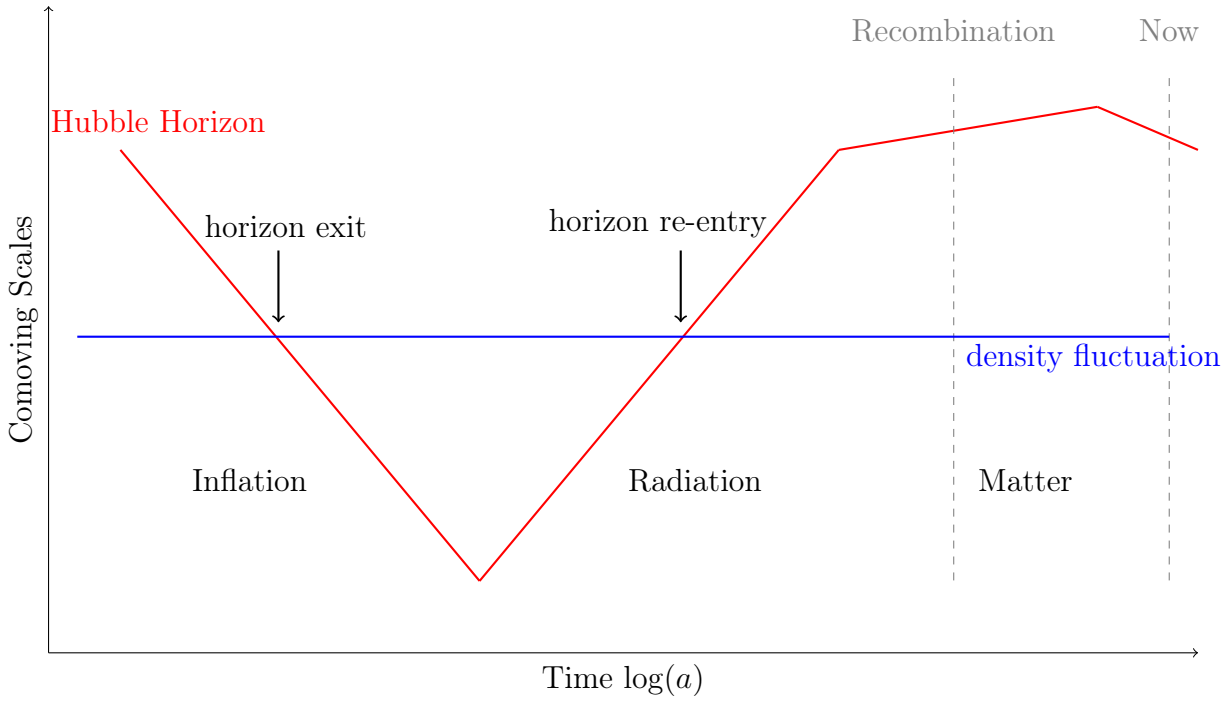

Figure 1.3: All scales that are relevant to cosmological observations were bigger than the Hubble horizon just at the onset of the radiation epoch. Only those scales that entered the horizon could interact and evolve according to physical laws.

then the condition of an infinitely large horizon corresponds to $p > 1$ when taking the limit $a_i \to 0$. Meanwhile, given the expression for the cosmic acceleration $\ddot{a} \propto p(p-1)t^{p-2}$, we can notice the condition $p > 1$ corresponds to the accelerated expansion of the universe. Once we assume it happened before radiation, the shrinking Hubble horizon (or infinitely large particle horizon) follows as a consequence. Thus, we have a simple mechanism to explain the uniform temperature of the CMB.

This leads us to ask: "How long did inflation last?". The answer to this question is significant since all the observed scales on the night sky exited the Hubble horizon over a specific interval of time during inflation, with the largest scales only now re-entering, as seen in Fig.1.3. As a result, we are interested in a period from the end of inflation (t_{end}) to an earlier time (t_i) when the smallest and the largest scales we observe today were created, respectively. What happened before the creation of the observed largest scale is an irrelevant question as long as the observational objective is concerned. As discussed earlier, the comoving particle horizon during inflation is much larger than the particle horizon of the radiation, dust, and dark energy-dominated epochs. Then, we can write

$$|\tau_{infl}| > \tau_0, \tag{1.12}$$

where $\tau_{infl} = \int_{t_i}^{t_f} \frac{dt}{a} = \int_{a_i}^{a_f} \frac{da}{a^2 H}$ is the duration of inflation and τ_0 represents the period from the onset of radiation until now. The absolute value of τ_{infl} indicates that we start the time counting from the end of inflation so that the accelerated expansion happens at some negative comoving time $-\tau_{infl}$.

If we recall Friedmann's first equation in Eq. 1.2, we notice the flatness of potential (the dominant term during inflation) translates to the Hubble parameter being almost constant,

$$\tau_{infl} = \int_{a_i}^{a_f} \frac{da}{a^2 H} = \frac{1}{H_{infl}}(\frac{1}{a_i} - \frac{1}{a_f}) \approx \frac{1}{a_i H_{infl}}, \tag{1.13}$$

the last approximation comes from $a_i \ll a_f$ due to inflation. Next, when computing τ_0, a key point to consider is that most of the expansion after the end of inflation happened during radiation dominated era. Between the time radiation ended and now, space expanded by about 8 e-folds which is much smaller than the expansion that took place before. Thus, the approximate statement that only the radiation domination happened after inflation is a valid as long as the spacetime expansion is concerned. During that time, the Hubble parameter changes as $H \propto a^{-2}$, so that $a^2 H = const = a_f H_{infl}$. Then the proper time from the end of inflation until now becomes

$$\tau_0 = \int_{a_f}^{a_0} \frac{da}{a^2 H} = \frac{1}{a_f^2 H_{infl}}(a_0 - a_f) \approx \frac{1}{a_f^2 H_{infl}}, \tag{1.14}$$

where we used $a_f \ll a_0 = 1$. During radiation, the temperature changes with the expansion of space as $T^{-1} \propto a$. Therefore we can write,

$$\frac{a_f}{a_i} > \frac{a_0}{a_f} = \frac{T_f}{T_0}. \tag{1.15}$$

The current average temperature of the universe is about $T_0 \sim 10^{-4} eV$ as provided by CMB measurements. While the reheating temperature is considered on the order of the Grand Unified Theory (GUT) scale $T_f \sim 10^{16}$ GeV giving us $\frac{a_f}{a_i} > \frac{a_0}{a_f} > 10^{29}$. On the other hand, notice that Hubble parameter $Hdt = \frac{da}{a}$ implies

$$\int H dt = \ln \frac{a}{a_{const}}. \tag{1.16}$$

We recognize this integral as the number of e-folds N_e the universe has to expand from its initial size a_{const} to a final size a. This number is usually referred to as the duration of inflation. With this new concept, we have

$$N_e = \ln \frac{a_f}{a_i} > 66, \tag{1.17}$$

a minimal duration, inflation has to occur to resolve the horizon problem.

1.2.1.2 Flatness Problem

It was mentioned earlier that CMB favors flat spacetime. However, a tremendous fine-tuning is required for spacetime to remain flat since any small deviation can grow very rapidly. We will show this, first, by recalling Friedmann's equation,

$$H^2 = \frac{\rho}{3M_P^2} - \frac{k}{a^2}, \tag{1.18}$$

where $M_p = (8\pi G)^{-1/2}$ is the reduced Planck mass. We can transform the above equation using the density parameter or the total abundance $\Omega = \frac{\rho}{3M_p^2 H^2}$,

$$\Omega^{-1} - 1 = -\frac{3M_P^2 k}{\rho a^2}. \tag{1.19}$$

If the universe is flat $k = 0$, we would have $\Omega = 1$. However, should there exist an initial small perturbation, it would grow fast. To show this, we observe that during the matter-dominated universe $\rho \propto a^{-3}$, the scale dependence of the density parameter is

$$\Omega^{-1} - 1 \propto a, \tag{1.20}$$

and during radiation-dominated universe $\rho \propto a^{-4}$, it is

$$\Omega^{-1} - 1 \propto a^2. \tag{1.21}$$

Therefore, any small deviation from unity at early times would become enormous at late times. The initial value of Ω must be fine-tuned very carefully. To give a rough estimation, one requires at the Planck scale

$$|\Omega(M_p)^{-1} - 1| \lesssim 10^{-60} \tag{1.22}$$

to have a flat spacetime now. Even if everything started at the Big Bang Nucleosynthesis (BBN), when the universe was 1 sec old, it still requires an incredible fine-tuning of Ω on the order of 10^{-16}. It suggests that the universe's flatness observed by CMB would not be possible unless some very special initial conditions are assumed.

Now, going back to Eq. 1.19 we can observe that the small deviation from flatness would not grow if the dominant energy content evolve as $\rho \propto a^{-2}$. On the other hand, from the continuity equation, we have $\rho \propto a^{-3(w+1)}$ implying the upper bound for the equation of state of the dominant matter content:

$$w < -1/3. \tag{1.23}$$

Again, this statement corresponds to the accelerated expansion of the universe at early times.

Thus, there is a solution for both the horizon and flatness problems – accelerated cosmic expansion. The inflation period allows for $\Omega^{-1} - 1$ to decrease significantly so that even at the current epoch we can have $\Omega^{-1} - 1 \simeq 0$ regardless of pre-inflation value.

Although, all the characteristics of this process closely resemble the properties of the Λ-dominated expansion of the universe, we can't assume that it was the cosmological constant preceding the radiation-dominated epoch. The most compelling reason against it is that Λ does not redshift away, its energy density remains constant. Therefore, radiation and matter domination cannot follow after the Λ-dominated universe. We need to have a matter content that has a dynamic behavior, i.e. a fluid that acts as Λ for a short period and then decays very quickly.

1.2.2 Inflationary Mechanism

As observed previously, we cannot rely on the cosmological constant to explain the accelerated expansion before the radiation epoch. We need a new mechanism to account for the shrinking Hubble horizon at early times. It should necessarily be a fluid with negative pressure and with non-trivial dynamic behavior to decay after producing enough cosmic expansion.

At the level of quantum field theory, all the particles are manifestations of some field in space and correspond to the relativistic generalization of the Schrodinger wavefunction. The quantization of a field's excitation corresponds to a particle's state and the properties of a field translate to the properties of a particle like its mass, charge or spin, etc. From the field theory point of view, a scalar field is the simplest field belonging to the class of relativistic bosons with spin zero. Other fields corresponding to photons (boson with a unit spin) and fermions such as electrons are characterized by vector and spinor fields, respectively. The situation with scalar fields is different since they don't change under rotation reflecting the isotropic nature of the universe. In the 1980's, several prominent physicists including Alan Guth, Andrei Linde, Paul Steinhardt, and Andreas Albrecht proposed an inflationary framework based on this scalar field called inflaton [31–33]. As of now, we discovered only one fundamental scalar field – the Higgs field. This thesis work focuses solely on the consequences of a single scalar field inflation. The Lagrangian

involves a minimally coupled scalar field ϕ that participates passively in the interaction with gravity through spacetime and has a self-interacting property through its potential energy $V(\phi)$. The action is simple, in the sense, that the kinetic term ($\frac{1}{2}\partial_\mu\phi\partial^\mu\phi$) appears in linear order which is not the case for more complicated models. We have

$$S_\phi = \int d^4x\sqrt{-g}\left[-\frac{1}{2}\partial_\mu\phi\partial^\mu\phi - V(\phi)\right]. \tag{1.24}$$

where the first term in the square bracket corresponds to the kinetic energy of the inflaton field, while the second term is its potential energy.

The Lagrangian has a dual role in the field theory. On the one hand, it acts as a source of the conserved quantities giving rise to physical observables such as the energy-momentum tensor $T_{\nu\mu}$. To that end, one needs to vary the action with respect to the metric to obtain the system's thermodynamic properties. In a sense, this process gives us macroscopic information about the system. On the other hand, Lagrangian encodes the equation of motion of the field in itself which is obtained by varying it with respect to the field. The situation is similar to what we do with thermodynamics to understand "what happens" macroscopically and in statistical physics to comprehend "why it happens" microscopically. We will do both procedures to obtain a complete understanding of the field and its consequences for conventional cosmological evolution.

1.2.2.1 Macroscopic Properties of Inflaton

As mentioned earlier, obtaining the energy density or the pressure of the single fluid system amounts to the metric variation of the corresponding Lagrangian as

$$\begin{aligned}
\delta S_\phi &= \int d^4x\left[\delta\left(\sqrt{-g}\right)\left(-\frac{1}{2}\partial_\mu\phi\partial^\mu\phi - V(\phi)\right) + \sqrt{-g}\left(-\frac{1}{2}\partial_\mu\phi\partial_\nu\phi g^{\mu\nu}\right)\right] \\
&= \int d^4x\left[\frac{1}{2}\sqrt{-g}g^{\mu\nu}\delta g_{\mu\nu}\left(-\frac{1}{2}\partial_\alpha\phi\partial^\alpha\phi - V(\phi)\right) + \sqrt{-g}\left(-\frac{1}{2}\partial_\mu\phi\partial_\nu\phi\right)\left(-g^{\mu\alpha}g^{\nu\beta}\delta g_{\alpha\beta}\right)\right] \\
&= \int d^4x\frac{\sqrt{-g}}{2}\left[\left(-\frac{1}{2}\partial_\alpha\phi\partial^\alpha\phi - V(\phi)\right)g^{\mu\nu} + \partial^\mu\phi\partial^\nu\phi\right]\delta g_{\mu\nu}.
\end{aligned}$$

By recalling the definition of $T_{\nu\mu}$, the stress-energy tensor becomes

$$T^{\mu\nu}_\phi = \frac{2}{\sqrt{-g}}\frac{\delta S_\phi}{\delta g_{\mu\nu}} = \left(-\frac{1}{2}\partial_\alpha\phi\partial^\alpha\phi + V(\phi)\right)g^{\mu\nu} + \partial^\mu\phi\partial^\nu\phi. \tag{1.25}$$

We use the FRW metric and separate the spatial and time-like components to obtain

$$T_{00} = \frac{1}{2}\dot{\phi}^2 + \frac{1}{2}\frac{(\nabla\phi)^2}{a^2} + V(\phi), \tag{1.26}$$

$$T_{ij} = \partial_i\phi\partial_j\phi - a^2 g_{ij}\left(\frac{1}{2}\dot{\phi}^2 + \frac{1}{2}\frac{(\nabla\phi)^2}{a^2} - V(\phi)\right), \tag{1.27}$$

where the gradient $(\nabla\phi)^2 = g^{ij}\partial_i\phi\partial_j\phi$ is taken with respect to the comoving coordinates. In the perfect fluid form, we have the energy density $\rho_\phi = T_{00}$ and pressure $p_\phi = \frac{1}{3}g^{ij}T_{ij}$ as

$$\rho_\phi = \frac{1}{2}\dot{\phi}^2 + \frac{1}{2}\frac{(\nabla\phi)^2}{a^2} + V(\phi), \tag{1.28}$$

$$p_\phi = \frac{1}{2}\dot{\phi}^2 - \frac{1}{6}\frac{(\nabla\phi)^2}{a^2} - V(\phi). \tag{1.29}$$

In the discussion of the flatness problem, we showed the condition $w < -1/3$ for the accelerated expansion to occur. However, we can realize rich possibilities within this new framework since the equation of state for the inflaton field is

$$w = \frac{\rho_\phi}{p_\phi} = \frac{\frac{1}{2}\dot{\phi}^2 - \frac{1}{6}\frac{(\nabla\phi)^2}{a^2} - V(\phi)}{\frac{1}{2}\dot{\phi}^2 + \frac{1}{2}\frac{(\nabla\phi)^2}{a^2} + V(\phi)}. \tag{1.30}$$

If the kinetic term $(\dot{\phi}^2)$ dominates, $w = 1$, there will be no inflationary scenario; the gradient energy $(\nabla\phi)$ dominance requires $w = -1/3$ which lies at the boundary between expansion with or without acceleration; lastly, the potential energy $(V(\phi))$ dominance corresponds to $w = -1$. The last case can produce all the theoretical and experimental implications of the cosmological constant. However, the possibility of the gradient energy dominance will be absent from our discussion. This is because, during inflation, any inhomogeneities in the energy will be diluted away with the exponential stretching of the spacetime and this is characterized by the division of the scale factor in the expression above.

The ultimate goal is a transient Λ-like behavior in the early universe. One way to accomplish this is to have the kinetic term subdominant. In that case, the potential is approximately flat mirroring the behavior of the cosmological constant. Still, as soon as the potential steepens, the field acquires more kinetic energy exiting the acceleration phase thus ending the inflation. This is one of the attractive features of the scalar field to be able to accommodate the transient state of the acceleration of the universe with relatively simple dynamics.

The next stepping stone to narrate the universe's history is to explain how to get the radiation era. Originally, Guth proposed a scenario where the scalar field is trapped

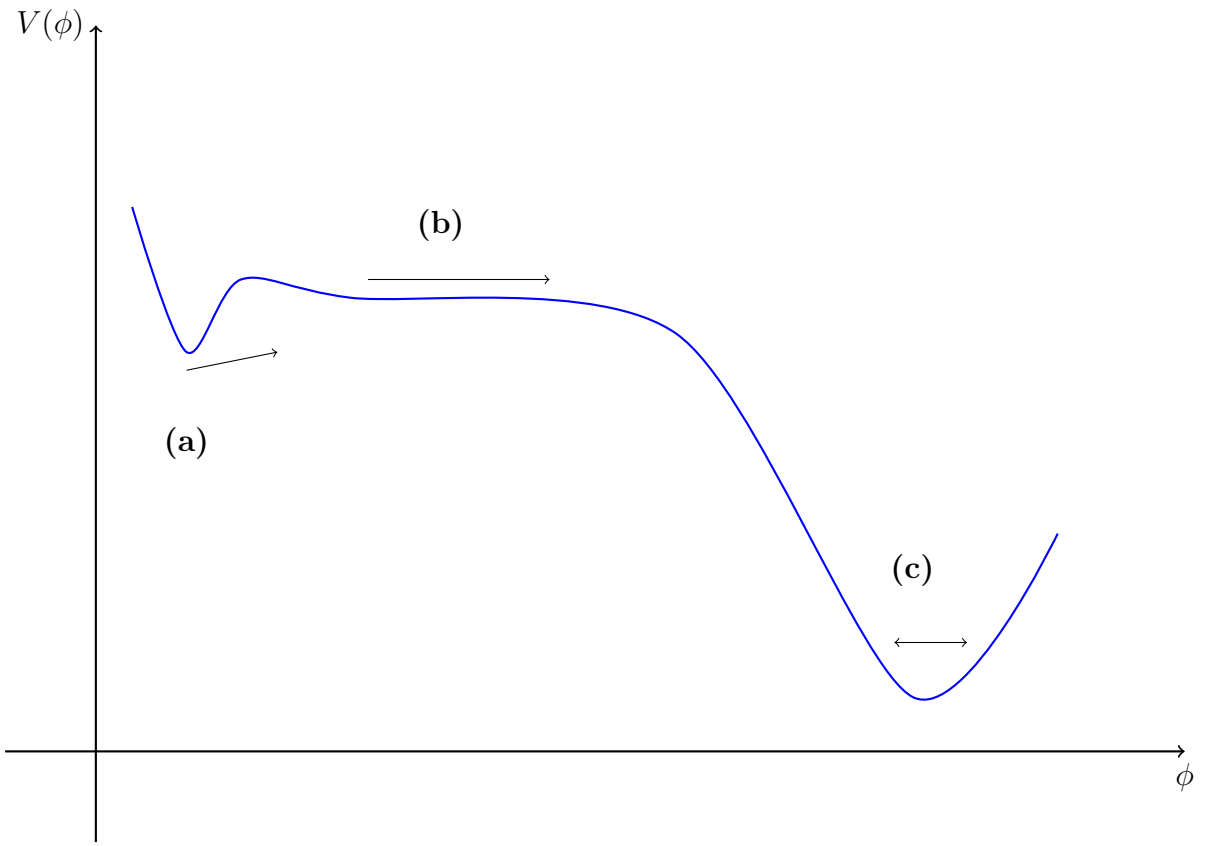

Figure 1.4: Scalar field and Inflation. Case (a) corresponds to a scenario where the field is trapped in a local minimum of the potential and decays through quantum tunneling. However, this is ineffective in producing reheating. Another inflationary scenario consists of two phases. In phase (b), the field tunnels to a shallow region of the potential and rolls slowly toward the true minimum establishing the inflation period. In phase (c), the kinetic energy dominates the field energy and marks the beginning of the reheating period where the field oscillates and transfers its energy to other relativistic fields which starts the conventional cosmological evolution.

in a false minimum of the potential so that the kinetic energy completely vanishes to give way to inflation. To exit this state, the field has to undergo quantum tunneling to reach the true minimum of the potential. This is probabilistic and difficult to realize how to transition to the radiation epoch. This is the "old inflation" model. The new model proposed by Linde suggests that the field rolls down its potential slowly until it becomes steep driving the field toward the true minimum. As a result, the field cannot climb over its potential barrier since it is the global minimum. Here the field oscillates with its huge energy storage. Eventually, the field loses all its energy and transfers it to other fields starting the reheating period.

1.2.2.2 Microscopic Properties of Inflaton

Until now, we presented a qualitative picture of the field dynamics that result in cosmic inflation. What we have done is to probe the response of the scalar field system to the spacetime geometry in a macroscopic way. However, the field itself is the primary variable of the system described by the Lagrangian in Eq. 1.24. We have to know the intricacies of the field's interaction with itself and with other fields to have a quantitative picture of the whole inflationary process. To completely characterize the field at this microscopic level, we derive the governing dynamical equations of this field. To do that, we vary the action with respect to the field

$$\begin{aligned}\delta S_\phi &= \int d^4x\sqrt{-g}\left[-g^{\mu\nu}\partial_\mu\phi\partial_\nu(\delta\phi) - V'(\phi)\delta\phi\right] \\ &= \int d^4x\left[\partial_\nu\left(\sqrt{-g}g^{\mu\nu}\partial_\mu\phi\right)(\delta\phi) - \sqrt{-g}V'(\phi)\delta\phi\right] \\ &= \int d^4x\sqrt{-g}\left[\frac{1}{\sqrt{-g}}\partial_\nu\left(\sqrt{-g}g^{\mu\nu}\partial_\mu\phi\right) - V'(\phi)\right]\delta\phi,\end{aligned} \tag{1.31}$$

where we used the integration by parts for the first term and set the field variation at infinity to zero. We require $\delta S_\phi = 0$ which gives us

$$\frac{1}{\sqrt{-g}}\partial_\nu\left(\sqrt{-g}g^{\mu\nu}\partial_\mu\phi\right) - V'(\phi) = 0. \tag{1.32}$$

As discussed earlier, any inhomogeneity in the field and in the geometry of the spacetime will be diluted. Then using the homogeneous and isotropic RW metric $g_{\nu\mu} = diag(-1, a^2(t), a^2(t), a^2(t))$, we obtain

$$\frac{1}{a^3}\partial_t\left(-a^3\dot{\phi}\right) + \frac{1}{a^2}\nabla^2\phi - V'(\phi) = 0. \tag{1.33}$$

After a simple algebraic manipulation, we have the equation of motion for the inflaton field

$$\ddot{\phi} + 3H\dot{\phi} - \frac{1}{a^2}\nabla^2\phi + V'(\phi) = 0, \tag{1.34}$$

or simply

$$\ddot{\phi} + 3H\dot{\phi} + V'(\phi) = 0, \tag{1.35}$$

where we ignored the gradient energy of the field. Assuming inflaton was the only dominant component in the early universe, we can write the first Friedmann equation as

$$H^2 = \frac{8\pi G}{3}\rho_\phi = \frac{1}{3M_P^2}\left(\frac{1}{2}\dot{\phi}^2 + V(\phi)\right) \tag{1.36}$$

As one can see from Eq. 1.35, the field's motion depends on the two competing forces. The slope of potential energy sources the motion of the field. However, due to spacetime response to the field's motion, we have a friction term due to Hubble expansion which is proportional to the field velocity and damps any variation in the field.

1.2.2.3 Slow-roll Inflation

Once we know the general equation of motion for the scalar field, we can impose several constraints on the field's microscopic characteristics to acquire the inflationary phase.

1) The field potential should be much larger than its kinetic energy to act as a cosmological constant that accelerates cosmic expansion,

$$\frac{1}{2}\dot{\phi}^2 \ll V(\phi), \tag{1.37}$$

ensuring $w_\phi \approx -1$ during inflation.

2) The acceleration of the field should be small, otherwise, the field reaches a faster pace in a short amount of time violating the first constraint.

$$\ddot{\phi} \ll 3H\dot{\phi}. \tag{1.38}$$

These are called the slow-roll conditions. With these constraints, the inflaton's equation of motion and Friedmann's equation are simplified as

$$\begin{aligned} 3H\dot{\phi} &\simeq -V'(\phi), \\ H^2 &\simeq \frac{V(\phi)}{3M_P^2}. \end{aligned} \tag{1.39}$$

Conventionally, slow-roll parameters are expressed as

$$\begin{aligned} \epsilon_\phi &= \frac{1}{2}M_P^2\left(\frac{V'(\phi)}{V(\phi)}\right)^2, \\ \eta_\phi &= M_P^2\frac{V''(\phi)}{V(\phi)}. \end{aligned} \tag{1.40}$$

With the slow-roll conditions, we can write the general formula for N_e in Eq. 1.16 as

$$\begin{aligned} N_e &= \int_{t_i}^{t_e} H(t)dt \\ &= \int_{\phi_i}^{\phi_e} \frac{H}{\dot{\phi}}d\phi \\ &\approx -\frac{1}{M_p}\int_{\phi_i}^{\phi_e} \frac{1}{\sqrt{2\epsilon_\phi}}d\phi. \end{aligned}$$

One needs to ensure that these parameters are indeed "slow". From Friedmann's second equation, we have

$$\dot{H} = -\frac{1}{2M_p^2}\dot{\phi}^2, \tag{1.41}$$

then dividing by H^2, while assuming $H^2 \approx \frac{M_p^2}{3}V$, and substituting Eq. 1.40 gives

$$-\frac{\dot{H}}{3H^2} \simeq \frac{M_P^2}{6}\left(\frac{V'(\phi)}{V(\phi)}\right)^2 = \frac{\epsilon_\phi}{3} \ll 1, \tag{1.42}$$

where we used $1/2\,\dot{\phi} << V(\phi)$. Therefore, requiring $\epsilon_\phi \ll 1$ satisfies our demand that the fluid acts as the cosmological constant. On the other hand, we can compute the field acceleration by taking the derivative of the simplified inflaton equation of motion

$$\ddot{\phi} \simeq \partial_t\left(-\frac{V'(\phi)}{3H}\right) \simeq -\frac{V''(\phi)\dot{\phi}}{3H} + \frac{V'(\phi)}{3H}\frac{\dot{H}}{H^2}, \tag{1.43}$$

the last term is negligible since $\epsilon_\phi = \frac{\dot{H}}{H^2} \ll 1$, then

$$\left|\frac{\dot{\phi}}{3H\phi}\right| \simeq \left|\frac{V'''(\phi)}{9H^2}\right| = \frac{1}{3}M_P^2\frac{V''(\phi)}{V(\phi)} = \left|\frac{\eta_\phi}{3}\right| \ll 1. \tag{1.44}$$

Thus, we see that the slow-roll conditions translate to the conditions on the slope $V'(\phi)$ and curvature $V''(\phi)$ of the filed potential. Therefore, we say the inflation ends when the following conditions are broken:

$$\epsilon_\phi \ll 1, \quad |\eta_\phi| \ll 1. \tag{1.45}$$

Here, it is relevant to say a few more words on the curvature of the potential by noticing its direct relation with the effective mass of the scalar field as

$$m_{eff}^2 = \frac{d^2V_\phi}{d\phi^2}. \tag{1.46}$$

This mass should be small due to the flat scalar field potential to produce inflation. In other words, to ensure the scalar field motivated inflation, we must have an almost massless field compared to the Planck mass scale.

Despite the importance of the slow roll parameters, they are not physical observables and we are not interested in them from the observational point of view. As it will be shown in due time, they determine the actual physical quantities such as the spectral index n_s and the tensor to scalar ratio r. These quantities will be discussed in detail later. The slow-roll parameters are related to the physical observables as

$$\begin{aligned} r &= 16\epsilon_H \\ n_s &= 2\eta_H - 4\epsilon_H + 1, \end{aligned} \tag{1.47}$$

where the subscript indicates the Hubble slow-roll parameters that describe the kinematics of inflation and defined as

$$\begin{aligned}\epsilon_H &= \frac{1}{4\pi G}\left(\frac{H'(\phi)}{H(\phi)}\right)^2 = -\frac{\dot{H}}{H^2} = 4\pi G\frac{\dot{\phi}^2}{H^2} \\ \eta_H &= \frac{1}{4\pi G}\left(\frac{H''(\phi)}{H(\phi)}\right) = -\frac{1}{2}\frac{\ddot{H}}{\dot{H}H} = -\frac{\ddot{\phi}}{H\dot{\phi}}\end{aligned} \tag{1.48}$$

The relation to the potential slow-roll parameters is $\epsilon_\phi = \epsilon_H, \eta_\phi = \eta_H + \epsilon_H$.

We have certain observational bounds for these quantities, obtained by several cosmic surveys. For example, the spectral index has the bound of $n_s = 0.9649 \pm 0.0042$ at the 68% confidence level following the Planck 18 results [34]. Meanwhile, the tensor-to-scalar ratio is constrained to $r_{0.002} < 0.1$ at 95% confidence level by the BICEP measurements [35], where the subscript in r corresponds to the pivot scale $k = 0.002$ Mpc^{-1} at which the measurement was carried out. When combined with the Planck 18 data the upper bound for tensor-to-scalar ratio gets even lower $r < 0.056$, making it even more difficult to detect.

1.2.2.4 Slow-roll Inflationary Models

There are several classes of inflationary models developed during the 1980s. The motivation behind them was either finding a natural extension of the Standard Model or just finding the functional form for the potential that satisfies the slow-roll conditions. The potential of single scalar field models can generally be represented as a series expansion

$$V(\phi) = \sum_{n=0}^{\infty} c_n \left(\frac{\phi}{\lambda}\right)^n \tag{1.49}$$

where λ is some constant associated with ultraviolet (UV) cutoff and the constant should be $c_n = O(1)$ unless there is a good argument for why these coefficients must be large. However, the Planck scale is believed to be the high energy physics limit so that $\lambda < M_p = 1$. Then the series diverges for $\phi > 1$ and may converge for $\phi < 1$. The former is associated with the large field and the latter with small-field models. In the following, we will briefly consider these two models.

1. Large field models

This model corresponds to chaotic inflation as introduced by Linde [36]. It is called chaotic because one doesn't need to choose any special initial conditions to drive the inflation. As long as the field is large, we are guaranteed to have inflation, and any

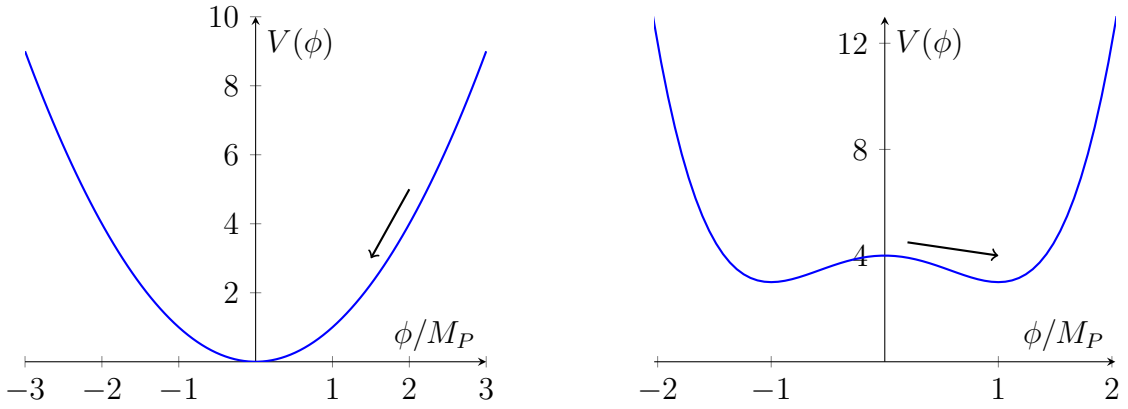

(a) Large field model.

(b) Small field model.

Figure 1.5: Different models with potential energy $V(\phi)$. [Left panel] The field starts to roll down to the true minimum of the potential from an initially high energy position, which corresponds to the large field model. This scenario is conventionally characterized as chaotic inflation. [Right panel] Small field model has a local maximum in the center where the field is located initially. Since this state is unstable, the field starts to move to the global minimum producing inflation along the way.

specificity of the initial condition is "washed out". Given the potential of the model (refer to panel (a) of Fig. 1.5),

$$V(\phi) = \lambda\phi^n, \tag{1.50}$$

we can find the slow-roll parameters as

$$\epsilon_\phi = \frac{n^2}{2}\left(\frac{M_P}{\phi}\right)^2, \quad \eta_\phi = n(n-1)\left(\frac{M_P}{\phi}\right)^2, \tag{1.51}$$

giving us the number of e-folds

$$N_e \simeq \frac{1}{2n}\frac{\phi_i^2}{M_P^2}. \tag{1.52}$$

To satisfy $N_e \approx 50 - 60$ e-folds, one requires $\phi >> M_p$. From the observational perspective, it is interesting to show the impact of the free parameter n of the model on the $r - n_s$ plane (see Fig. 1.6). As one can see as the potential gets steep with the higher power n, the spectral index starts to deviate from 1 more and more while overproducing the tensor-to-scalar ratio. Therefore constraints put by Planck 18 and BICEP results disfavor monomial potential with big power law relations. However, active research is currently underway to push for large field models by claiming that in supergravity theories the scalar field has a geometric structure that can naturally accommodate inflation like α-attractor models.

2. **Small field models**

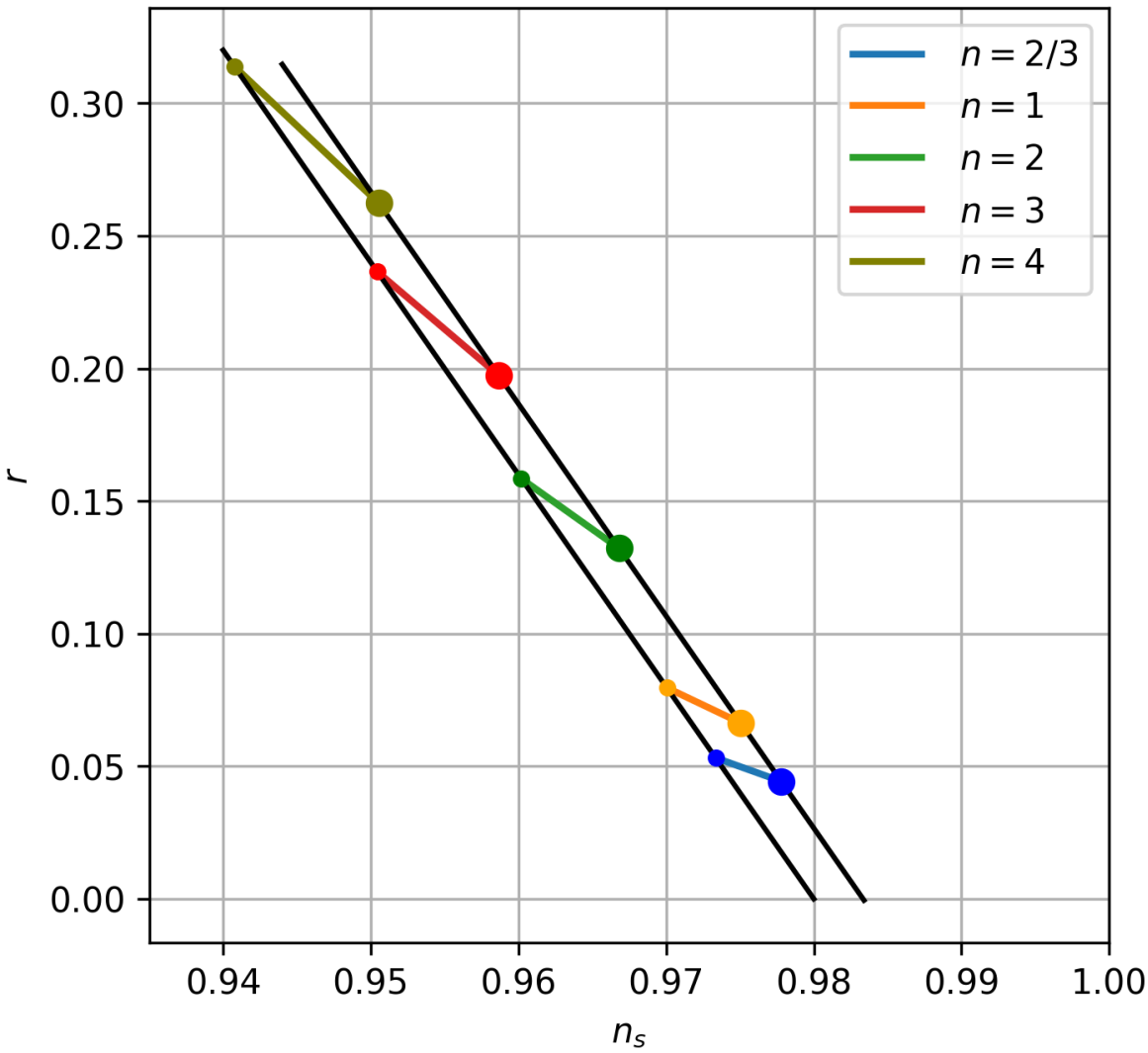

Figure 1.6: Large field model and its impact on r and n_s. Thick and thin dots correspond to 60 and 50 e-folds, respectively. As can be seen, the free parameter n will have a stronger imprint on the observables as its value increases.

In this scenario, a field is initially located on top of a local maximum of the potential and starts to move towards the plateau producing the inflationary phase (see panel (b) of Fig. 1.5). The attractive feature of this model is its subplanckian scale, unlike chaotic inflation. However, the field's state on the local maximum is a disadvantage since it requires fine-tuning of the initial conditions. Field's initial velocity might be slightly bigger/less to stop/sustain inflation.

A particular example of the small field model is given by a hilltop potential,

$$V(\phi) = V_0 \left(1 - \left(\frac{\phi}{\mu}\right)^n\right). \tag{1.53}$$

Considering the special case when $p = 4$, we plug this potential into Eq. 1.41 and integrate

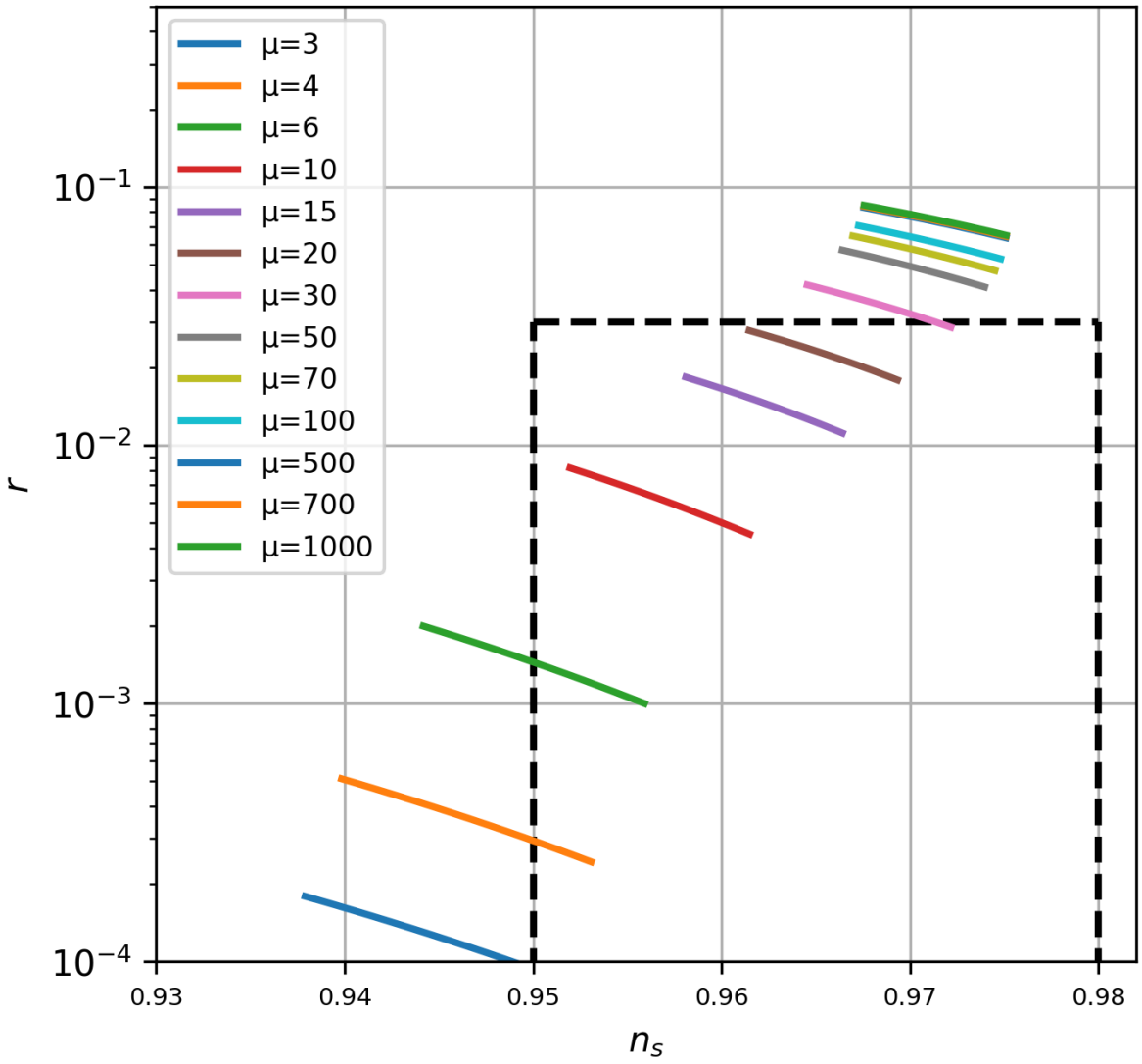

Figure 1.7: Hilltop potential with $p = 4$. The dashed black box is the constraint we have from the experimental observations. With $\mu > 30$, the potential overproduces the tensor perturbation while in the case of $\mu < 6$, potential shows a higher scale variation of the spectral index.

to obtain

$$N = -\frac{1}{M_p}\int_{\phi_i}^{\phi_e}\frac{V}{V'}d\phi = \frac{1}{8M_p}\left[\phi_i^2 - \phi_e^2 + \mu^4(\frac{1}{\phi_i^2} - \frac{1}{\phi_e^2})\right]. \tag{1.54}$$

If the range for the number of e-folds is $N_e \in [46, 60]$, we can check its consequences on the observables. We use the relation between N_e and ϕ_i, ϕ_f – field's initial and final states during inflation. From Fig. 1.7, we can see an optimal range for μ within which the field value can change to produce the right amount of inflation. The dashed black box corresponds to the observationally viable ranges for n_s and r.

1.2.2.5 Quantum Fluctuation of Inflaton Field

Before discussing any quantum effects, we note that the classical GR still holds even during inflation. The reason is that the threshold energy density for quantum gravity is on the order of $\sim M_P^4 = (10^{18}\text{GeV})^4$ while inflationary energy density is estimated to be $\rho \sim H^2 M_P^2 = (10^{16}\text{GeV})^4$ which is significantly smaller. Furthermore, flat and homogeneous FRW is still believed to apply due to the exponential stretching of spacetime during inflation. However, small curvature fluctuations persist in the background which will be the seed for the structure growth.

Earlier, we demonstrated how single-field inflation can solve the horizon and flatness problems in a detailed manner. However, one can do even more to explain the origin of the cosmological structure and its imprint on the CMB power spectrum. To accomplish that, one has to simply recall that the scalar field is the quantum field. The latter is subject to quantum fluctuations due to Heisenberg's uncertainty principle: a field in its ground state cannot stay motionless. Therefore, we consider a small fluctuation of the field $\delta\phi(\tau, x)$ around its homogeneous background $\bar{\phi}(\tau)$. We assume the fluctuation to be small compared to the background field value $\delta\phi \ll \bar{\phi}$ such that

$$\phi = \bar{\phi} + \delta\phi, \tag{1.55}$$

and to investigate the evolution of this small fluctuation, we perturb Eq. 1.34. This time we don't neglect the gradient energy of the field since the new fluctuation term contains spatial dependence. However, the term involving the second derivative of the potential is negligible due to the small mass scale of the field $m_\phi \ll H$. Then, we have

$$\delta\ddot{\phi} + 3H\delta\dot{\phi} - \frac{1}{a^2}\nabla^2\delta\phi = 0, \tag{1.56}$$

which, in the conformal coordinate system, becomes

$$\delta\phi'' + 2\frac{a'}{a}\delta\phi' - \nabla^2\delta\phi = 0. \tag{1.57}$$

where prime denotes derivatives w.r.t conformal time τ. The modes are coupled by the Laplacian operator ∇^2. The homogeneity and isotropy of the universe dictate that there is no preferred location or direction in the universe. This assumption naturally leads to Fourier transformation $\delta\phi = \int \frac{d^3k}{2\pi^3}\delta\phi_k(\tau)e^{i\mathbf{k}\cdot\mathbf{x}}$, a linear system where each mode evolves independently $\nabla^2 \to -k^2$, that is, it depends only on the mode k not on its location or

direction. Then investigating just one of these modes is enough to have a general picture of the fluctuation. In Fourier basis, we have

$$\delta\phi_k'' + 2\frac{a'}{a}\delta\phi_k' + k^2\delta\phi_k = 0, \tag{1.58}$$

now, we move the field fluctuation itself to the conformal coordinate and write

$$\chi_k(\tau) = a(\tau)\delta\phi_k(\tau), \tag{1.59}$$

then the above equation transforms into

$$\chi_k'' - \frac{a''}{a}\chi_k + k^2\chi_k = 0. \tag{1.60}$$

It is convenient to have a context to compare k^2 with $\frac{a''}{a}$ directly. To do that, we relate it to the conformal time. First, we observe that during inflation $H \approx const$, therefore

$$\tau = \int \frac{dt}{e^{Ht}} = -\frac{1}{aH}, \tag{1.61}$$

then it follows that $\frac{a''}{a} = \frac{2}{\tau^2}$. Finally, we obtain

$$\chi_k'' + k^2\left(1 - \frac{2}{(k\tau)^2}\right)\chi_k = 0. \tag{1.62}$$

The comoving scale has an inverse relation with the wave-number $\lambda_c = \frac{2\pi}{k}$, at the same time, it is bigger than the Hubble radius $\lambda_c > (aH)^{-1}$ during inflation since all scales will be stretched beyond the horizon sooner or later. Then considering Eq. 1.61, we have $|k\tau| \ll 1$ for scales outside the horizon and $|k\tau| \gg 1$ inside the horizon while $|k\tau| \approx 1$ marks the horizon crossing. For subhorizon scales, Eq. 1.62 reduces to an ordinary harmonic oscillator with the solution $\chi_k = e^{\pm ik\tau}$. Therefore, we look for solutions in the form,

$$\chi_k(k,\tau) = f_k(\tau)e^{\pm ik\tau}, \tag{1.63}$$

with $f_k(\tau)$ being constant for subhorizon scales. Solving for f_k gives $f_k(\tau) = A + \frac{B}{\tau}$ with $B = \pm\frac{i}{k}A$. After absorbing A into the definition of χ_k, we can write

$$\chi_k^{\pm}(\tau) = \left(1 \mp \frac{i}{k\tau}\right)e^{\mp ik\tau}. \tag{1.64}$$

At this point, we notice that the implications of this equation are twofold. First, the superhorizon modes $k\tau \ll 1$ will freeze with different modes causally disconnected. This is seen by the corresponding solution $|\chi_k| = (k\tau)^{-1} \Leftrightarrow \phi_k = \frac{H}{k}$ where $H \approx const$ during

inflation. Second, the amplitude of subhorizon modes $k\tau \gg 1$ will be suppressed $|\chi_k| = 1 \Leftrightarrow \phi_k = \frac{1}{a}$ due to spacetime expansion.

Inflaton fluctuations will be written as

$$\delta\hat{\phi}(\mathbf{x},\tau) = \int \frac{d^3k}{(2\pi)^3}\frac{1}{\sqrt{2ka}}\left[\hat{a}_{\mathbf{k}}\chi^{+}_{\mathbf{k}}(\tau)e^{i\mathbf{k}\cdot\mathbf{x}} + \hat{a}^{\dagger}_{\mathbf{k}}\chi^{+*}_{\mathbf{k}}(\tau)e^{-i\mathbf{k}\cdot\mathbf{x}}\right]. \tag{1.65}$$

where $\hat{a}_{\mathbf{k}}$ and $\hat{a}^{\dagger}_{\mathbf{k}}$ are the creation and annihilation operators, respectively. This indicates that in quantum mechanics the field perturbations become operators. We will be interested in the ground state of inflaton since it corresponds to its initial state where the small fluctuations disturb the field to start rolling down its potential producing inflation. Due to the homogeneity of the universe, we can pick one position x and investigate it expecting that every other position will result in the same outcome. We consider the location $x = 0$ for simplicity. We know the average fluctuation is $\langle 0|\delta\hat{\phi}(0,\tau)|0\rangle = 0$ which reflects the random nature of quantum fluctuations. On the contrary, the variance, corresponding to the non-zero quantum uncertainty in the field, is not zero. It shows the spread or the energy stored in the fluctuations. One observes that the only non-zero combination of annihilation and creation operators is $\hat{a}_{\mathbf{k}}\hat{a}^{\dagger}_{\mathbf{k}'}$, then the variance becomes

$$\begin{aligned}\langle 0|\delta\hat{\phi}^2(0,\tau)|0\rangle &= \int \frac{d^3k}{(2\pi)^3}\int \frac{d^3k'}{(2\pi)^3}\frac{1}{\sqrt{2k}}\frac{1}{\sqrt{2k'}}H^2\tau^2\chi^{+}_{k}\chi^{+*}_{k'}\langle 0|\hat{a}_{\mathbf{k}}\hat{a}^{\dagger}_{\mathbf{k}'}|0\rangle \\ &= \int \frac{d^3k}{(2\pi)^3}\int \frac{d^3k'}{(2\pi)^3}\frac{H^2\tau^2}{2k}|\chi^{+}_{k}|^2(2\pi)^3\delta^3(\mathbf{k}-\mathbf{k}') = \int \frac{d^3k}{(2\pi)^3}\frac{H^2\tau^2}{2k}|\chi^{+}_{k}|^2.\end{aligned} \tag{1.66}$$

Focusing only on the superhorizon modes $|\chi_k| = 1/k\tau$, we write

$$\langle 0|\delta\hat{\phi}^2(0,\tau)|0\rangle = \int \frac{d^3k}{(2\pi)^3}\frac{H^2}{2k^3} = \int \frac{dk}{k}\left(\frac{H}{2\pi}\right)^2 = \left(\frac{H}{2\pi}\right)^2 \ln\left(\frac{k_{\max}}{k_{\min}}\right), \tag{1.67}$$

since the largest scales (k_{min}) leave the horizon first, $k_{min} \sim (\tau_i)^{-1} = a_i H$ and smallest scales leave the horizon at the end of inflation, $k_{max} \sim (\tau_e)^{-1} = a_e H$, the variance can be related to the number of e-folds as

$$\langle 0|\delta\hat{\phi}^2(0,\tau)|0\rangle = \left(\frac{H}{2\pi}\right)^2 \ln\left(\frac{a_e}{a_i}\right) = \left(\frac{H}{2\pi}\right)^2 N_e. \tag{1.68}$$

This means that the amplitude of variance grows linearly with N_e implying that as inflation lasts longer, more and more scales have the chance to leave the horizon and be frozen. Defining the power spectrum $\mathcal{P}_\phi(k)$ of the inflaton perturbation as

$$\langle 0|\delta\hat{\phi}^2(0,\tau)|0\rangle = \int \frac{d^3k}{(2\pi)^3}\mathcal{P}_\phi(k), \tag{1.69}$$

we see that

$$\mathcal{P}_\phi(k) = \frac{H^2}{2k^3} \propto k^{-3}. \tag{1.70}$$

Perturbation analysis of general relativity shows that a small fluctuation in inflaton, which is the dominant source during inflation, leads to a perturbation in the energy-momentum tensor and subsequently in the metric tensor of the spacetime. Without going too much into detail at this point, we can simply state that the curvature perturbation, coming from the tensor part of metric perturbation, has a direct relation with the inflaton perturbation [37],

$$\mathcal{P}_\mathcal{R}(k) = \left(\frac{H}{\dot{\phi}}\right)^2 \mathcal{P}_\phi(k), \tag{1.71}$$

If we define a dimensionless power spectrum as

$$\Delta^2_\mathcal{R} \equiv \frac{k^3}{2\pi^2}\mathcal{P}_\mathcal{R}(k) = \left(\frac{H}{\dot{\phi}}\right)^2 \left(\frac{H}{2\pi}\right)^2 = \frac{1}{8\pi^2 M_P^2}\frac{H^2}{\epsilon_H}, \tag{1.72}$$

we will see the consequence of the following argument: inflation ends at slightly different times, with $\delta t = \delta\phi/\dot{\bar{\phi}}$, meaning the different patches of the universe are expanded by slightly different amounts accompanying the spread in the energy density proportional to the fluctuation in the scale factor at the end of inflation,

$$\frac{\delta\rho}{\rho} \sim \frac{\delta a}{a} = H\delta t = \frac{H^2}{2\pi\dot{\bar{\phi}}}. \tag{1.73}$$

Therefore, one can roughly say the curvature perturbation, or its dimensionless version, quantifies how much of the original quantum field fluctuations per number of e-folds ($\delta\phi \sim H/2\pi$) can be effectively converted into the curvature perturbations which lead to the density perturbation.

In the dimensionless power spectrum $\Delta^2_\mathcal{R}$ we have an implicit scale dependence hidden in H and $\dot{\phi}$. To see this, notice that during horizon crossing $k = aH$, different scales leave at slightly different times. Within that time period both H and $\dot{\phi}$ change slightly due to the slow-roll conditions. Conventionally, this scale dependence is given by the relation,

$$n_s - 1 = \frac{d\ln\Delta^2_\mathcal{R}}{d\ln k}, \tag{1.74}$$

where the dimensionless power spectrum is found as

$$\Delta^2_\mathcal{R} = A_s\left(\frac{k}{k_\star}\right)^{n_s-1}, \tag{1.75}$$

We can connect the spectral index with the slow-roll parameters using Eq. 1.74. First, notice

$$\frac{d}{d\ln k} = k\frac{d}{dk} = aH\frac{d}{d(aH)} \simeq a\frac{d}{da} = \frac{1}{H}\frac{d}{dt} = \frac{\dot{\phi}}{H}\frac{d}{d\phi}, \tag{1.76}$$

where we used $H \approx const$ and dropped the overbar on ϕ for simplicity. Combining the slow-roll and Friedmann equations (see Eq. 1.39) gives

$$\frac{\dot{\phi}}{H} \simeq \frac{-V'(\phi)}{3H^2} \simeq -M_P^2\frac{V'(\phi)}{V(\phi)}. \tag{1.77}$$

Given the above relations, we can easily track the following derivation

$$\begin{aligned} n_s - 1 &\approx -M_P^2\frac{V'(\phi)}{V(\phi)}\frac{1}{\Delta_{\mathcal{R}}^2}\frac{d\Delta_{\mathcal{R}}^2}{d\phi} \\ &\approx -M_P^2\frac{V'(\phi)}{V(\phi)}\left[-\frac{V'(\phi)}{V(\phi)} - \frac{V''(\phi)}{V'(\phi)}\right] \\ &= 2\eta_\phi - 6\epsilon_\phi. \end{aligned} \tag{1.78}$$

Until this point, we have been deriving the direct consequences of quantum fluctuations in inflaton. Small fluctuations in the huge energy deposit of the scalar field in the early universe lead to a substantial back reaction from spacetime in the form of metric fluctuations. This leads to the curvature perturbation because the variation in the field's energy density curves the spacetime in various amplitudes. It is a scalar perturbation with dynamical evolution and its characterized mainly by spacetime expansion, horizon crossing, etc. Another form of metric perturbation is the tensor perturbation which originates from the quantum fluctuation in the gravitational field. In other words, it is synonymous to the intrinsic fluctuation of the spacetime curvature. This should not lead to confusion with the earlier concept of curvature perturbations which represent the modifications of the shape of spacetime by creating potential wells and hills. Thus, the fluctuations in the gravitational field produces ripples in the spacetime geometry that propagate as the transverse and traceless gravitational waves. All inflation does to them is to stretch them beyond the Hubble horizon during inflation. Since they don't originate from inflaton field fluctuation, we will not bother ourselves deriving an expression for the tensor power spectrum. The result can be found in many cosmology books [37]

$$\Delta_t^2(k) = \frac{8}{M_P^2}\left(\frac{H}{2\pi}\right)^2, \tag{1.79}$$

where we can see an explicit dependence on the energy scale of inflation. Eq. **??** with the

slow-roll Friedmann equation reveals

$$\left(\frac{H}{\dot{\phi}}\right)^2 \approx \frac{1}{2\epsilon_\phi}\frac{1}{M_P^2}, \tag{1.80}$$

showcasing weaker amplitude for tensor power spectrum compared to the scalar power spectrum in Eq. 1.72, making it an observational challenge to detect. Conventionally, one considers a quantity that can make comparison easy between tensor and scalar perturbation by introducing the scalar-to-tensor ratio as

$$r \equiv \frac{\Delta_t^2}{\Delta_{\mathcal{R}}^2} = 16\epsilon_\phi. \tag{1.81}$$

This parameter gives additional information about the energy scale of the inflation since it is related to the potential of the inflaton as

$$V^{1/4} \sim \left(\frac{r}{0.01}\right)^{1/4} 10^{16}\,\text{GeV}, \tag{1.82}$$

so that if it is $r \approx 0.01$, we may expect an energy scale of inflation to be on the order of the GUT scale. The term r can also serve to distinguish between inflationary models through the Lyth bound. The latter is derived by observing $r = \frac{8}{M_P^2}\left(\frac{\dot{\phi}}{H}\right)^2$ and recalling that H doesn't vary much during inflation,

$$\frac{\triangle\phi}{M_P} \approx 2\left(\frac{r}{0.01}\right)^{1/2}. \tag{1.83}$$

This demonstrates that large r is produced by superplanckian variations in the field. It further demonstrates the power of measuring r to constrain inflationary models. As mentioned earlier, we have good observational bounds for the parameters n_s and r while precisions are only improving with time. For example, large field models corresponding to chaotic inflation have been ruled out since they produce way more primordial gravitational waves in contradiction with the latest findings about the tensor-to-scalar ratio [34, 35, 38].

1.2.3 Observational Evidence for Dark Energy

In this subsection, we shift our attention to the late universe. Observation of the accelerated cosmic expansion had a lasting effect on the development of the standard model in cosmology [21, 22]. We go through these observational evidence for dark energy.

1.2.3.1 Supernovae Ia

The Type Ia supernovae (SN Ia) are created by the explosion of the white dwarf stars when their mass exceeds the Chandrasekhar mass limit. In standard theory, they are believed to pop up everywhere in the universe regardless of their location meaning they have a common absolute magnitude (denoted as M) independent of the redshift z. In other words, they are so bright that we can observe them to large distances. Hence, their spectral evolution (lightcurve) is well studied by atomic physics both in emission and absorption. By observing them at different wavelengths and times, one can standardize them to connect their apparent brightness to the their intrinsic brightness and hence measure their distance. Therefore, we consider them ideal standard candles to measure the distance or the redshift z and the apparent magnitude m of any astronomical object. Speaking of the distance, the concept that is frequently used in this type of measurement is the luminosity distance d_L defined as

$$d_L^2 \equiv \frac{L_s}{4\pi\mathcal{F}}, \tag{1.84}$$

where L_s is the absolute luminosity of the source and $\mathcal{F}$ is the energy flux. Theoretically, one can find d_L in terms of the properties of the universe's geometry (determined by FRW metric),

$$d_L = \frac{(1+z)}{H_0}\int_0^z \frac{dz'}{\sqrt{\sum_i \Omega_i^{(0)}(1+z')^{3(1+w_i)}}}. \tag{1.85}$$

The crucial property of this integral is its dependence on the matter content of the universe characterized by the density parameter Ω_i. The presence of dark energy can significantly increase the luminosity distance of an object. One can show it by by taking, for example, $\Omega_m + \Omega_d = 1$ where Ω_m refers to non-relativistic matter, Ω_d refers to the dark energy density, and its equation of state is $w = -1$. This means evaluating the integral for z' involves smaller Ω_m for much of the integral.

The apparent and absolute magnitude are related to the luminosity distance by

$$m - M = 5\log_{10}\left(\frac{d_L}{\text{Mpc}}\right) + 25. \tag{1.86}$$

Thus, if we can measure the apparent magnitude m and know the absolute magnitude M, we can obtain the luminosity distance. Then using Eq. 1.85 yields the matter content of the universe. To illustrate this, let us consider two supernovae: 1992P at low ($z = 0.026$)

and 1997ap at high redshift ($z = 0.83$) with known apparent magnitudes $m = 16.08$ and $m = 24.32$, respectively. First, we have to find the absolute magnitude of the standard candles and it can be done by observing the approximation $d_L \approx z/H_0$ for $z \ll 1$. For 1992P supernovae and using Eq. 1.86 results in $M = -19.09$. Using the same Eq. 1.86 with the absolute magnitude for 1997ap supernovae results in $d_L \approx 4800$Mpc or

$$H_0 d_L \simeq 1.16, \quad \text{for } z = 0.83,$$

where we used $H_0^{-1} = 2998h^{-1}$ Mpc with $h = 0.72$. However Eq. 1.85 suggests other values,

$$\begin{aligned} H_0 d_L &\simeq 0.95, \quad \Omega_m^{(0)} \simeq 1, \\ H_0 d_L &\simeq 1.23, \quad \Omega_m^{(0)} \simeq 0.3, \quad \Omega_\Lambda^{(0)} \simeq 0.7. \end{aligned}$$

Thus, the two approaches give almost the same answer for $H_0 d_L$ when the existence of the dark energy accounting for 70% universe's matter content is assumed. Statistically speaking, one cannot claim that the universe's expansion is accelerating based on a single data. Perlmutter *et al.* [22] studied 42 SN Ia supernovas at $z = 0.18 - 0.83$ redshift range and found $\Omega_m = 0.28^{+0.09}_{-0.08}$ meaning most of the matter in the universe is the dark energy $\Omega_\Lambda = 0.72$.

According to these investigations, the cosmic expansion started to accelerate very recently. We can see this from

$$z < z_c \equiv \left(\frac{2\Omega_\Lambda^{(0)}}{\Omega_m^{(0)}} \right)^{1/3} - 1, \tag{1.87}$$

obtained from the acceleration condition Eq. 1.2. For $\Omega_m^{(0)} = 0.3$, $\Omega_\Lambda^{(0)} = 0.7$ we get $z_c = 0.67$ which is close to today $z_{\text{today}} = 0$.

Other candles can also probe the acceleration phase of the universe. The FRIIb radio galaxies studied in [39, 40] yield similar results. However, their constraints are weaker compared to the Type SN Ia measurements. Another promising candle to probe the acceleration for high redshifts ($z > 5$) is the Gamma Ray Bursts (GRB) [41]. So if there is appreciable dark energy at early times, we can learn about it through the information provided by GRB measurements. However, at present, cosmologists see systematics dominating radio galaxies and GRB.

Another method that gives a standard ruler to determine dark energy is the Baryon Acoustic Oscillation (BAO) [42]. We can see BAO in the non-integrated Sachs-Wolfe effect, the first dominant term:

$$\frac{\triangle T}{T} \sim (\frac{1}{4}\delta_k + \Phi) + \text{Doppler shift} + \text{ISW} + \dots \tag{1.88}$$

where δ_k is the density perturbation, Φ is the decaying gravitational potential due to spacetime expansion. Once the scale k enters the horizon, it oscillates under the effect of two competing forces – gravitational force and pressure force (resulting from the photon-baryon coupling). Sound horizon has a scale just enough for the pressure waves to make one oscillation; smaller scales make many more while larger scales don't have enough time to make a single oscillation. When we add up all the contribution from different parts of the universe, we will have constructive interference for the sound horizon scale. The total effect is the first peak in the CMB power spectrum. It is the dominant linear order term where non-linear effects are negligible and thus most precisely determined. We can use the sound horizon as the standard ruler. Using the comoving sound horizon ($r_{\text{s.h}} = 150\text{Mpc}$) and measuring the angular size (θ) of two points in the sky, we can determine the angular diameter distance

$$D_A = \frac{r_{\text{s.h}}}{\theta}.$$

Likewise, we can calculate D_A theoretically for a flat universe,

$$D_A = \frac{1}{1+z}\int_0^z \frac{dz}{H(z)},$$

this means the presence of dark energy (inside H) changes the geometry of the universe. By comparing the values of angular diameter distance from two approaches, we can find out the composition of the matter content.

1.2.3.2 Age of the Universe

We know the age of the oldest stellar populations (t_s) and they can provide a lower bound for the universe's age (t_0) since we expect $t_0 > t_s$. However, with the flat CDM model without dark energy, it is impossible to satisfy this consistency check, as we show below.

Jimenez *et al.* found $t = 13.5 \pm 2$ Gyr as the age for the Globular clusters in our galaxy by using a method-independent approach [43]. While Richer *et al.* [44] and Hansen *et al.* [45] showed the globular cluster M4 to have an age $t = 12.7 \pm 0.7$ Gyr by implementing

the white dwarfs cooling sequence method. These discoveries require the universe's age to be $t > 11 - 12$ Gyr. At the same time, assuming ΛCDM model, Planck18 data produces the age of the universe $t_0 = 13.799 \pm 0.021$Gyr [46].

We demonstrate what is the problem with a flat universe consisting of only dust. The universe's age can be calculated as

$$t_0 = \int_{t_i}^{t_f} dt = \int_{t_i}^{t_f} \frac{da}{aH} = \int_0^\infty \frac{dz}{(1+z)H_0\sqrt{\Omega_r^{(0)}(1+z)^4 + \Omega_m^{(0)}(1+z)^3 + \Omega_K^{(0)}(1+z)^2 + \Omega_\Lambda^{(0)}}}. \tag{1.89}$$

where one can ignore the radiation $\Omega_r^{(0)}$ since the effect coming from $z > 1000$ is negligible (the radiation dominated period is short). With $\Omega_K^{(0)} = 1 - \Omega_m^{(0)}$ (no dark energy $\Omega_\Lambda^{(0)} = 0$), we have

$$t_0 = \frac{1}{H_0}\int_0^\infty \frac{dz}{(1+z)^2\sqrt{1+\Omega_m^{(0)}z}}. \tag{1.90}$$

Integrating this for $\Omega_m^{(0)} = 1$ gives

$$t_0 = \frac{2}{3H_0}, \tag{1.91}$$

and we know the most accurate value for the Hubble parameter is $H_0^{-1} = 9.776h^{-1}$ Gyr with $0.64 < h < 0.8$ [47]. Substitution yields $t_0 = 8 - 10$ Gyr, giving much younger universe than the oldest globular cluster.

However, a flat universe with $\Omega_m^{(0)} + \Omega_\Lambda^{(0)} = 1$ can easily fix this contradiction

$$H_0 t_0 = \int_0^\infty \frac{dz}{(1+z)\sqrt{\Omega_m^{(0)}(1+z)^3 + \Omega_\Lambda^{(0)}}} = \frac{2}{3\sqrt{\Omega_\Lambda^{(0)}}} \ln\left(1 + \sqrt{\frac{\Omega_\Lambda^{(0)}}{\Omega_m^{(0)}}}\right). \tag{1.92}$$

Substituting $\Omega_m^{(0)} = 0.3$ and $\Omega_\Lambda^{(0)} = 0.7$, we get

$$t_0 = \frac{0.964}{H_0} \tag{1.93}$$

which gives the universe's age $t_0 = 13.1$ Gyr for $h = 0.72$. Thus, ΛCDM model can elegantly solve the age crisis. This is another hint that we are missing an extra matter component of the universe – dark energy.

1.2.3.3 CMB and LSS Measurements

Observations concerning the early and late time processes such as CMB [48] and Large Scale Structure (LSS) [49, 50] provide independent information about dark energy. In

the case of CMB, dark energy's implication on the power spectrum is indirect since it was subdominant at early times and came to dominate the universe's energy density only recently ($z \approx 0.7$). In the LSS measurements, the impact of dark energy plays a crucial role since they focus on the late-time evolution of the universe (from $z \approx 3$ to today).

The existence of dark energy has a twofold significance on CMB. First, its presence modifies the geometry of the universe which has direct manifestation in the location of the first peak in the CMB power spectrum. The peak corresponds to the sound horizon during recombination. The calculation of its location involves the angular diameter distance D_A between the CMB and the present time. To determine D_A, we have to know about the properties of spacetime geometry which is affected by the late time dark energy domination. Second, dark energy has an imprint on the Integrated Sach-Wolfe (ISW) effect. It enhances the large-scale anisotropies (low multiples, $l \lesssim 10$) since CMB photons, during their journey, enter potential wells and their energy increases. However, the gravitational potentials decay due to the accelerated expansion and photons spend less energy to climb out of the well, in total, gaining net energy.

In LSS measurements, dark energy's imprint is directly observed since it suppresses the structure growth by expanding the space, reducing the gravity effect. The growth rate f is commonly used to describe the structure growth

$$f \propto \frac{d \ln \delta}{d \ln a}, \tag{1.94}$$

where the density perturbation δ slows down due to Hubble expansion. Observations such as weak lensing, galaxy clustering, and redshift space distortion (RSD) directly involve the suppressed growth rate.

Combining SN Ia, CMB, and LSS measurements provide tight constraints, ruling out the flat universe that consists of only dust [51]. Compiling these independent observations strongly suggests the existence of cosmological constant with density parameter $\Omega_\Lambda^{(0)} = 0.7$ and the equation of state $w = -1$. Apart from the fine-tuning and naturalness problems inherent in the cosmological constant, observations have long been consistent with its predictions.

1.2.4 Dark Energy as Quintessence

A flurry of activities in the 1970s in high-energy physics and cosmology resulted in ready-to-explain theories about the mechanisms of inflation. It took some time for the above-mentioned observational breakthroughs to make these speculations a central topic for research. Thus, a dynamical scalar field producing the recent accelerated expansion originated from those investigations of inflation. This dynamical field with its Lagrangian given in Eq. 1.24 was studied as a substitute for the cosmological constant. Historically, a tilted, linear potential was first proposed by Linde to replace the flat potential to consider the dynamic nature of cosmological constant [52].

We have derived macroscopic and microscopic properties of the scalar field, or simply quintessence onward, in Subsections 1.2.2.1 and 1.2.2.2. Without further going into the technical details, we notice that everything remains the same with the inflationary scenario except for the two facts. First, inflation lasted only about $\triangle t \approx 10^{-35}$s while the recent accelerated expansion has been going on for billions of years. In addition, we are not here interested in how long it will continue since our observation is only concerned with the past events. Second, the energy scales of these two processes are vastly different: the inflationary energy scale is commonly estimated to be around the GUT scale $\sim 10^{16}$GeV, while the late time acceleration energy scale is very low $\sim 10^{-12}$GeV while the current Hubble rate is $H_0 \sim 10^{-42}$GeV. It suggests that quintessence dynamics are naturally much slower and we do not need to put certain conditions like slow-roll. The other reason being that the universe is not as close to a de Sitter state as during inflation since there is non-negligible ordinary matter. Also, dark energy does not obey the slow approximation used for inflation (all terms in Eq. 1.35 are of comparable magnitude).

1.2.4.1 Quintessential Inflation

After studying inflation and dark energy, a question arises: why don't we use a single scalar field to act both as inflaton and quintessence field? Peebles and Vilenkin considered that question by proposing a potential for the scalar field ϕ to act as inflaton in the early universe and quintessence field in late universe [53]. In this regard, it was important that the potential doesn't possess true minimum since it would force the field to oscillate and

decay into other fields. The proposed potential has the following form

$$V(\phi) = \begin{cases} \lambda(\phi^4 + M^4), & \text{for } \phi < 0, \\ \\ \frac{\lambda M^4}{1+(\phi/M)^\alpha}, & \text{for } \phi \geq 0. \end{cases} \tag{1.95}$$

At first, with $\phi < 0$ the field produces chaotic inflation. Long after that, the sign of the field flips $\phi > 0$ and we will have a flat potential with a low energy scale corresponding to quintessence, eventually, driving the universe's expansion into its accelerated phase. The difficulty with this model is that it has no tracking solutions to avoid sensitivity to the initial conditions. Also, reheating after inflation is absent since the potential has no minimum. People speculated about the gravitational particle production to account for reheating but this mechanism proved to be inefficient [54]. Another peculiar property of this model is its kinetic energy dominated phase before radiation starts. This has a huge effect on the density of the primordial gravitational waves [53, 55]. Despite these apparent drawbacks, people developed mechanisms to constrain undesirable consequences of this model.

1.3 Dark Matter and Structure Growth

1.3.1 Observational Evidence For Dark Matter

The confirmation of the existence of dark matter came from different corners of the universe by various observations. In 1933, Fritz Zwicky observed faster galaxy rotations in the Coma Clusters [56, 57]. Using the virial theorem for self-gravitating systems, $2E_k = E_p$, he determined the galaxy velocity through the relation $v^2 = GM_{obs}/R$. Taking the values $M_{\rm obs} = 800 \times 10^9 M_\odot$ and $R \sim 10^6$ lyrs, he calculated $v \sim 10^2$ km s^{-1} but the observed value was $v \sim 10^3$ km s^{-1}. To match the observation with the theoretical prediction, one requires $M_{\rm tot} \sim 10^2 M_{\rm obs}$ meaning there is an extra mass. However, since that time the precision observations lowered the extra contribution to $\sim 10 M_{\rm obs}$.

Another observation pointing to extra mass came 40 years later in the 1970s by Ford and Rubin [58] showcasing strong evidence for the flat rotation curves corresponding to the outer regions of spiral galaxies. From the virial theorem, $v^2(r) = GM(r)/r$, we recognize that the velocity curve should steadily go to zero outside the galaxy disk. This is because the mass M approaches a constant value as less and less mass is present outwards so that

M/r approaches zero. Only when we imply $M(r) \sim r$ outside the disk $r > r_{\text{disk}}$, can we infer a flat rotation curve. This suggests an invisible matter outside the disk where its mass is distributed.

There was another breakthrough in CMB measurements in determining the temperature fluctuations at the time of recombination [30]. Temperature anisotropy was on the order of $\frac{\triangle T}{T} \sim 10^{-5}$ and it is related to the matter density perturbation at recombination $\frac{\triangle T}{T} \propto \delta \sim 10^{-5}$. Since that time, the universe expanded for about $a = 10^3$ hinting that we should expect $\delta \sim 10^{-2}$ now. However, we already have stars and galaxies, in other words, we are in the nonlinear regime for structure growth $\delta \gtrsim 1$. This gave way to speculations that there was a form of matter that could interact with photons only gravitationally so that matter density perturbations could cluster more efficiently during the radiation era. As soon as matter domination starts, we have gravitational potential well deep enough for the baryons to fall and cluster more quickly than expected. Statistically speaking, to fit CMB data more accurately, we are required to include a small amount of baryons ($\sim 4\%$) and a large amount of invisible dark matter ($\sim 26\%$).

1.3.2 Dark Matter Properties

We mentioned earlier that the only known property of dark matter is its gravitational interaction. Below, we consider the main properties that dark matter may possess and give bounds coming from theoretical considerations.

We know more of the mass density of dark matter and less of its number density. Its particle nature is quite elusive with its highly unconstrained particle mass. For any fundamental particle, its mass can range between $m_{\text{dm}} = 10^{-23}$ eV (so that its Compton wavelength is within galaxy scales, and hence it can explain rotation curves) and $m_{\text{dm}} = 10^{18}$ GeV. The lower bound comes from the velocity dispersion of stars in ultrafaint dwarf galaxies [59] while the upper bound is also found using velocity dispersion [60].

Dark matter doesn't have a charge and cannot interact with photons, otherwise, we could see it. However, during the pre-recombination era, it could possess a charge to decrease the clustering effect of dark matter. Estimation shows its value on the order of $\lesssim 10^{-6}$e to avoid inconsistencies with the data. The value is minuscule rendering any possibility of interaction with electron unfeasible [61].

When it comes to the spin property, this invisible matter is either fermion or bo-

son and depending on the choice, its mass can have different constraints. For example, fermionic dark matter cannot have a mass that is too light due to the Pauli exclusion principle and estimation gives $m_{\text{dm}} \gtrsim 10\text{eV}$. However, if it is boson then there is no lower bound since we wouldn't have any constraining principle as we had with fermions.

It is essential to point out that the growth of large-scale structures carries rich cosmological insight into the universe's different matter contents, their evolution, and so on. We can deduce constraints on the dark matter clustering through exploring deviations in gravitational attraction from Newton's value caused by its self-interaction or its different composition [62]. To study this effect, different approaches were taken both model-based and phenomenological.

In the following, we will study the growth of structure from density perturbations. We will see how curvature perturbation during inflation seeds the density perturbation in the radiation era linking up nicely with our previous discussion of inflation.

1.3.3 Density Perturbation

As we showed in the field perturbation analysis, any fluctuation in the inflaton sources metric perturbation. However, tensor perturbations in the metric are weakly coupled with ordinary matter except for neutrinos that have anisotropic stress (introduces off-diagonal terms in the stress-energy tensor). Thus, for structure growth analysis, we are content with the scalar perturbations. The perturbed metric becomes

$$ds^2 = -[1 + 2\Phi(t, \mathbf{x})]dt^2 + a^2(t)[1 - 2\Phi(t, \mathbf{x})]d\mathbf{x} \cdot d\mathbf{x}, \tag{1.96}$$

where ds^2 is the line element and $\Phi(t, \mathbf{x})$ corresponds to Newtonian potential. Due to the curvature perturbation $\mathcal{P}_\mathcal{R}$, inflation ends at slightly different times $\delta t \sim \delta\phi/\dot{\phi}$ causing fluctuation in the scale factor a which accompanies fluctuations in the energy density. In other words, $\mathcal{P}_\mathcal{R}$ directly sources matter density perturbation δ defined as

$$\delta(\mathbf{x}) = \frac{\rho(\mathbf{x}) - \bar{\rho}}{\bar{\rho}}, \tag{1.97}$$

where $\bar{\rho}$ is the mean background density and $\rho(\mathbf{x})$ corresponds to the density at position $\mathbf{x}$ such that $\delta(\mathbf{x}) \ll 1$. On the other hand, we saw that the CMB power spectrum is homogeneous and isotropic. These symmetries are well captured in the Fourier transform as each mode would evolve independently. Therefore, it is much more convenient to work

in Fourier space

$$\delta_k = \int \delta(\mathbf{x}) e^{-i\mathbf{k}\cdot\mathbf{x}} d^3x, \tag{1.98}$$

Without getting into details, we briefly summarize the implications of the density perturbation equation derived in many cosmology books such as [37]. Considering only the subhorizon scales and working in Fourier space, we have

$$\ddot{\delta}_k + 2\frac{\dot{a}}{a}\dot{\delta}_k + \left(\frac{c_s^2 k^2}{a^2} - 4\pi G\rho_{\text{tot}}\right)\delta_k = 0, \tag{1.99}$$

where c_s is the sound speed of the medium and ρ_{tot} is the sum of the energy density of each component. This is the evolution equation and we immediately notice that depending on the sign of the bracket, we will have two different solutions. If $\frac{c_s^2 k^2}{a^2} > 4\pi G\rho_{\text{tot}}$, the solution is damped meaning there will be no growth since the pressure forces neutralizes the gravitational pull. However, the case $\frac{c_s^2 k^2}{a^2} < 4\pi G\rho_{\text{tot}}$ corresponds to the solution we are looking for - gravitational collapse or growth of structure. Therefore the borderline has a special name - *Jean's wavelength*,

$$\lambda_J \equiv c_s\sqrt{\frac{\pi}{G\rho_{\text{tot}}}}. \tag{1.100}$$

In the following, we will consider the nature of structure growth in different cosmological epochs. In our calculations, the term $\frac{c_s^2 k^2}{a^2}$ will be neglected due to several factors: study of non-relativistic matter and large scales structure formations captured by $\lambda > \lambda_J$..

1.3.3.1 Structure Growth over Cosmic Epochs

We would like to see the growth of non-relativistic matter in various stages of the universe's history.

Radiation domination (RD). In this period, baryon and relativistic particles, such as photons, were coupled to each other acting as a single medium. Since pressure forces are strong enough to compete with the gravitational forces leading to subhorizon fluctuations, we will have oscillations with constant amplitude around $\delta_{r+b} = 0$. Thus, we don't expect growth during radiation since we are below the Jeans' length. However, if we assume the existence of cold dark matter (denoted with subscript c) which doesn't couple to photons, we can write

$$\ddot{\delta}_c + 2\frac{\dot{a}}{a}\dot{\delta}_c - 4\pi G\rho_{\text{tot}}\delta_c = 0. \tag{1.101}$$

During RD, we have $\rho_c \ll \rho_r$ and the time average of radiation density fluctuation is $< \delta_r > \approx 0$, so we expect $\ddot{\delta}_c + 2\frac{\dot{a}}{a}\dot{\delta}_c \gg 4\pi G\rho_{\rm tot}\delta_c$. Also, we note that during radiation the Hubble parameter evolves as $H = 1/2t$. All these arguments combined leads to

$$\ddot{\delta}_c + \frac{1}{t}\dot{\delta}_c = 0, \tag{1.102}$$

which has two solutions $\delta_c = \text{const}$ and $\delta \propto \ln t$. Thus, even though baryon density couldn't grow in this hostile environment, dark matter could cluster. Later, it would make up for that deficit in the observed CMB power spectrum. This happens because baryons will undergo a boost of clustering by falling into the non-zero CDM potential that experienced logarithmic growth during RD.

Matter domination (MD). Once the universe becomes cool enough, due to expansion, it transitions to its matter-dominated phase characterized by $a \propto t^{2/3}$, $H = \frac{2}{3t}$ and $4\pi G\rho = \frac{2}{3t^2}$. In this case, baryons decouple from photons and fall into CDM's potential well and they quickly catch up with the dark matter evolution. Afterwards, baryons and dark matter will act as a single medium throughout the cosmic evolution. We can write

$$\ddot{\delta}_m + \frac{4}{3t}\dot{\delta}_m - \frac{2}{3t^2}\delta_m = 0, \tag{1.103}$$

which has two solutions, one decaying $\delta_m \propto t^{-1}$ and one growing mode $\delta_m \propto t^{2/3}$. In terms of the scale factor, the growing mode is $\delta_m \propto a$. Thus, the structure grows proportional to a until dark energy takes over the matter content as the dominant one.

Dark energy domination. Dark energy domination is a recent event occurring at around $z \approx 0.7$. However, it has an important role in the universe's evolutionary dynamics. It changes the underlying geometry and suppresses the structure growth. In this era, we have $\rho_\Lambda \gg \rho_m$ conversely $H^2 \gg 4\pi G\rho_{\rm tot}\delta_m$ where $\rho_{\rm tot} = \rho_m + \rho_r$. Therefore, we solve the equation,

$$\ddot{\delta}_m + 2H\dot{\delta}_m = 0, \tag{1.104}$$

to find two solutions $\delta_m \propto \text{const}$ and $\delta_m \propto e^{-2t\cdot\text{const}} \propto a^{-2}$. The rate of growth de-accelerates eventually leading to a halt of growth altogether. It means the Newtonian potential decays $\Phi \propto a^2\rho_m \propto a^{-1}$ unlike its constant value during matter domination. This has an imprint on the observed CMB power spectrum through the Integrated Sachs-Wolfe effect as CMB photons experience decaying gravitational effect while moving towards us.

This analysis only applies to large scales frozen outside the horizon which have entered it only recently. For smaller scales, the evolution has been occurring for a longer time

resulting in their transition into the non-linear regime. To study small-scale evolution, we must abandon the linear perturbation theory in favor of non-linear theories. However, even within the linear regime, there are several persistent tensions with the standard model such as σ_8 tension. There are multiple fronts opened in theoretical cosmology to resolve this problem.

1.4 Aims and Structure of the Thesis

In the preceding sections, we presented the detailed history of our universe starting from the initial quantum fluctuations in the inflaton field leading up to the large-scale structure formation. In this thesis, we aim to investigate the models beyond ΛCDM and their detectable signatures on the growth of structure. In the rest of the thesis, I will present the following results in detail:

In Chapter 2, we study the α attractor model that explains inflation and dark energy with a single scalar field. We found a relationship between the prediction of inflation and the dynamic nature of dark energy. Our finding suggests there is an optimal medium to detect experimental signals for the equation of state $w \neq -1$ of dark energy and scalar-to-tensor ratio r predicted by inflation [28].

Chapter 3 presents the investigation of dark matter properties. We examined the implications of deviations in its clustering strength and equation of state on the structure growth. Employing a model-independent approach by binning the deviations in redshift, we conducted an information matrix analysis. Given a tomographic survey covering a wide range of redshifts, we can have a glimpse into how much dark matter can deviate from its standard description [63].

In Chapter 4, we study structure growth in the context of the modified gravity model. The modified part includes a coupling between gravity and matter which leaves a unique imprint on the matter clustering. Using redshift space distortion measurements, we conducted MCMC analysis showcasing a decrease in σ_8 tension [64].

We conclude in Chapter 5.

Chapter 2

Connecting Inflation and Dark Energy

2.1 Introduction

Due to their simplistic nature, scalar fields are the avenues to tackle various problems. For instance, we are familiar with the Higgs field in fundamental physics, inflaton field as the cause of rapid cosmic acceleration in the early universe, and possibly dynamic dark energy responsible for the late time cosmic acceleration. One of the first attempts to bring two different scalar fields together was the quintessential inflation framework which aimed to explain inflation and dark energy with a single potential [53]. However, the main goal being to choose the right form for the potential, it lacked a solid foundation in high-energy physics leaving an impression of an ad hoc model. A more robust concept must be built upon high-energy physics such as supergravity or string theory since inflation takes place at high energies where, as is usually believed, the strong symmetry constraints are restored. These additional symmetries can highly constrain the possible forms for the field's potential and kinetic energies, as is the case in α-attractors [65–67]. These models provide a unique, non-trivial geometry for the field space. The boundaries of this field space can accommodate high energy scales associated with inflation and low energy scales attributed to dark energy, e.g. [68, 69]. Finally, unifying these two phenomena as quintessential inflation has been a hot topic lately [70–77].

We will focus on α-attractors, a scalar field with a generic potential that includes Starobinsky cosmology. We further show that the field must be thawing recently to have certain desirable effects on cosmic evolution. This is an ideal scenario to explain the large gap in time between two inflationary epochs. Initially, the field was rolling down

the plateau during inflation terminating at a certain point when the potential steepens and decreases to its lowest value. From this moment onward, Hubble friction dominates the field dynamics, effectively, stopping the field, or "freezing" it, and releasing it only recently to thaw to behave differently than its counterpart – cosmological constant. It was shown in [78] that thawing fields have certain properties that can be analytically derived and numerically verified by solving the equations of motion for the field.

One of the main advantages of combining quintessential inflation with the α-attractor framework is to link the observables from the two eras. Observationally, the situation is similar to a "win-win" scenario. Failing to detect the primordial gravitational waves, characterized by r, can be understood as the field's premature cessation caused by its low kinetic energy and the Hubble friction once it reaches the second plateau and freezes higher up its potential. However, when it thaws, it will exhibit more dynamic behavior since the field acquired higher potential energy at the time of freezing. Therefore, a low r scenario will produce more deviations in the equation of state parameter w from that of the cosmological constant, a more favorable condition to be detected by future observations. On the other hand, if r is large due to a steeper potential, the field thaws at later times giving rise to less dark energy dynamics. Therefore, it will be hard to detect deviations from cosmological constant. We study conditions that favor observations of each parameter or a happy condition where the experimental signals from both can be detected. The potential energy we adopt avoids zero minimum corresponding to the cosmological constant and the evolution comes mainly from the α-attractor dynamics.

Section 2.2 provides symmetric considerations that lead to the α-attractor Lagrangian. While in Section 2.3, we discuss the interpretation of the α parameter and show how it emerges in the expressions for tensor-to-scalar ratio r and dark energy equation of state w linking two cosmic accelerations. In section 2.4, we briefly summarize the main characteristics of α-attractors and introduce the coupled system for the equations of motion. Section 2.4.1 solves the system numerically showcasing the influence of the model parameters α and initial field values ϕ_i on the solution. We present the main findings of this work in Section 2.4.2 where the relation between r and the dark energy equation of state parameters w_0 and w_a is studied both analytically and numerically. In Section 2.4.3, we discuss the constraints on the observable parameter from future experiments. Finally, a discussion and summary of our results are given in Section 3.5.

2.2 Canonical Action under Conformal Symmetry

The specific form of the α-attractor Lagrangian arises naturally when we impose additional symmetries. This approach provides constraints on the kinetic and potential terms and links the inflationary framework to high-energy physics. In most cases, conformal symmetry is the guiding principle for fundamental frameworks such as string theory and supergravity which have more built-in symmetries to extend the current physical theories. We can put it this way, the Poincare group states that regardless of where an observer is (translation), where he looks (rotation), and how fast he is moving (boost), all physical laws are the same; if we add additional transformations such as inversion, followed by translation, and followed by another inversion, then we get the full conformal group. Thus, a theory invariant under this full symmetry transformation will have a rich structure to accommodate the explanation of unique physical events such as inflation. In this symmetry, it is the angle θ that is preserved (through $\cos\theta = [\vec{A}\cdot\vec{B}]/[|\vec{A}|\cdot|\vec{B}|]$), and the scale invariance is automatically included if we consider constant scaling across spacetime which amounts to dilation. If we add to this argument the observational evidence for an almost scale-invariant CMB power spectrum, they all seem to hint towards conformal symmetry for early universe physics. However, it introduces its difficulty in explaining a mysterious mechanism that broke the conformal symmetry during inflation [79].

This section investigates conformal symmetry constraints on the scalar field canonical action. The constraints primarily focus on the metric (spacetime geometry) and the kinetic term (field dynamics). Since potential energy does not interact with the metric directly, the priority will be to ensure the conformal invariance of the kinetic term and the metric. Prior to that, we check whether the canonical form of the kinetic term in the action, which is Lorentz invariant, also respects conformal symmetry,

$$L = \frac{\sqrt{-g}}{2} g^{\mu\nu}\partial_\mu\phi\partial_\nu\phi. \tag{2.1}$$

We apply to this action the following general conformal transformation,

$$\tilde{g}_{\mu\nu} = e^{-2\sigma(x)} g_{\mu\nu}. \tag{2.2}$$

However, the Lagrangian 2.1 is indeed not invariant. To see this, we follow the effects of metric transformation on the action,

$$L = \frac{\sqrt{-\tilde{g}}}{2}\tilde{g}^{\mu\nu}\partial_\mu\phi\partial_\nu\phi = e^{-2\sigma}\frac{\sqrt{-g}}{2} g^{\mu\nu}\partial_\mu\phi\partial_\nu\phi, \tag{2.3}$$

here we used $\det(cA) = c^n \det(A)$ (for $n \times n$ matrix A) and $\tilde{g}^{\mu\nu} = e^{2\sigma(x)} g^{\mu\nu}$. Since the field is coordinate-dependent, it also transforms as

$$\tilde{\phi} = e^{\sigma(x)} \phi. \tag{2.4}$$

Then, substituting the transformed field and taking partial derivative give

$$L = \frac{\sqrt{-\tilde{g}}}{2} \tilde{g}^{\mu\nu} \partial_\mu \tilde{\phi} \partial_\nu \tilde{\phi} = \frac{\sqrt{-g}}{2} g^{\mu\nu} \partial_\mu \phi \partial_\nu \phi + \frac{\sqrt{-g}}{2} g^{\mu\nu} \left(\phi^2 \partial_\mu \sigma \partial_\nu \sigma + \partial_\mu \phi^2 \partial_\nu \sigma \right). \tag{2.5}$$

This shows that the original action is not invariant under conformal transformation. There must be an additional variable in the Lagrangian 2.1 to cancel the term in the bracket during the transformation. Turns out the non-minimal coupling term $\frac{1}{12}\phi^2 R(g)$ is what we seek. As a next step, we will show its conformal transformation. First, note the conformal transformation of Ricci scalar is [80]

$$\tilde{R} = e^{2\sigma} \left(R - 6 e^{\sigma} g^{\mu\nu} \partial_\mu \partial_\nu e^{-\sigma} \right), \tag{2.6}$$

combining this with the field transformation, we get,

$$\frac{\sqrt{-\tilde{g}}}{12} \tilde{\phi}^2 \tilde{R} = \frac{\sqrt{-g}}{12} \phi^2 R - \frac{\sqrt{-g}}{2} \phi^2 e^{\sigma} g^{\mu\nu} \partial_\mu \partial_\nu e^{-\sigma}. \tag{2.7}$$

Integrating the last term by parts and discarding the surface integral gives

$$\int d^4x \frac{\sqrt{-g}}{2} \phi^2 e^{\sigma} g^{\mu\nu} \partial_\mu \partial_\nu e^{-\sigma} = \int d^4x \frac{\sqrt{-g}}{2} \left[g^{\mu\nu} (\partial_\mu \phi^2 \partial_\nu \sigma + \phi^2 \partial_\mu \sigma \partial_\nu \sigma) + \phi^2 e^{\sigma} \partial_\mu g^{\mu\nu} \partial_\nu \sigma \right]. \tag{2.8}$$

The last term also cancels due to the metric being Riemannian manifold $\nabla_\mu g^{\mu\nu} = 0$. Finally, we obtain

$$L = \frac{\sqrt{-\tilde{g}}}{2} \left(\tilde{g}^{\mu\nu} \partial_\mu \tilde{\phi} \partial_\nu \tilde{\phi} + \frac{\tilde{\phi}^2 \tilde{R}}{6} \right) \overset{\text{C. S}}{=} \frac{\sqrt{-g}}{2} \left(g^{\mu\nu} \partial_\mu \phi \partial_\nu \phi + \frac{\phi^2 R(g)}{6} \right), \tag{2.9}$$

as the conformally invariant action. We recognize that the following gauge $\phi = \sqrt{6}$ reduces to the Einstein-Hilbert action without matter term. The next steps in the ensuing subsections are followed as in [81].

2.2.1 Enriching Field Structure with SO(1.1) Symmetry

To ensure non-trivial field geometry, we introduce a symmetry into our Lagrangian – SO(1, 1) - to make our field structure Lorentz invariant. Therefore, it is the Lorentz

subgroup – any matrix transformation that preserves the inner product $[x, y] = x^2 - y^2$ with a unit determinant. This symmetry allows the field to transform in a fashion that respects the conformal symmetry while being the simplest extension from the flat to the curved geometry for the field structure. As we will show later, this curved geometry is hyperbolic with negative curvature, meaning that away from the origin the field value will be stretched. In a flat geometry setup, a small change in the field corresponds to a small change in the potential. However, in negatively curved geometries, as we go farther away from the origin, the field increases quickly. Then assuming a smooth potential, a small change in its value is produced by a large difference in the field value. This effectively introduces a third-party involvement in the field evolution: it is not only the potential that dictates the field how to move but the evolution away from the origin will dictate the potential how to behave. In other words, we expect a small change in the potential gradient away from the origin, effectively, driving it to plateau.

Since SO(1, 1) is Lorentz 1+1 dimension, to have the inner product, we introduce a second field χ accordingly. Note, χ is a conformal compensator and has no associated physical degree. Then our conformally symmetric action transforms into

$$L = \frac{\sqrt{-g}}{2}\left[g^{\mu\nu}\partial_\mu\chi\partial_\nu\chi + \frac{1}{6}\chi^2 R(g) - g^{\mu\nu}\partial_\mu\phi\partial_\nu\phi - \frac{1}{6}\phi^2 R(g) - \frac{\lambda}{18}(\phi^2 - \chi^2)^2\right]. \quad (2.10)$$

One can observe that χ has a wrong sign which makes it look an ad hoc construction but it is a common practice in supergravity models to make the structure more elegant. In the meantime, we notice this theory becomes antigravity for $\chi^2 - \phi^2 > 0$. Then the role of χ is to represent the cutoff limit for ϕ to remain within the standard gravity. Again, we recover the Einstein-Hilbert action with $\chi^2 - \phi^2 = 6$ gauge. Here, the fields are defined as $\chi = \sqrt{6}\cosh(\varphi/6)$ and $\phi = \sqrt{6}\sinh(\varphi/6)$ in terms of a new field φ which is massless canonically normalized field. The term λ corresponds to the cosmological constant.

We can consider a more general case by replacing λ with a function $f(\chi, \phi)$ by breaking the introduced symmetries. However, we can do it gently in such a fashion to keep at least one of the symmetries. The natural choice is to preserve conformal symmetry and to deform SO(1, 1) so that we have $\lambda = f(\phi/\chi)$.

2.2.2 α attractor from $\chi = \sqrt{6\alpha}$ gauge

We choose a gauge for one of our fields to obtain the desired form of the action. With the choice $\chi = \sqrt{6\alpha}$, the Lagrangian in 2.10 modifies to

$$L = \frac{\sqrt{-g}}{2}\left[R\left(\alpha - \frac{\phi^2}{6}\right) - g^{\mu\nu}\partial_\mu\phi\partial_\nu\phi - 2f\left(\frac{\phi}{\sqrt{6\alpha}}\right)\left(\frac{\phi^2}{6} - \alpha\right)^2\right]. \tag{2.11}$$

This action is written in the Jordan frame which is favored to investigate the curvature modifications. However, an analogous way to study the modification is to use the usual Einstein frame which is well adapted to handle the modification in the matter part of the action. It is still not clear which frame is the actual physical frame. One subtle issue shown in the work [82] is that without including the "gravitational contact term" in the Jordan frame, the results will not be generically compatible in the two systems. Apart from that consideration, it is easy to switch to the Einstein frame by the following transformation,

$$g^J_{\mu\nu} = (\alpha - \frac{\phi^2}{6})^{-1} g^E_{\mu\nu}. \tag{2.12}$$

From the conformal transformation, we have $\tilde{g}_{\mu\nu} = e^{2\sigma(x)} g_{\mu\nu}$, then it is easy to recognize $\sigma = \ln\left((\alpha - \frac{\phi^2}{6})^{-1/2}\right)$. Using the results in [80], we get

$$R_J = \left(\alpha - \frac{\phi^2}{6}\right)\left[R_E + 3g_E^{\mu\nu}\partial_\mu\partial_\nu \ln\left(\alpha - \frac{\phi^2}{6}\right) - \frac{3}{2}g_E^{\mu\nu}\partial_\mu \ln\left(\alpha - \frac{\phi^2}{6}\right)\partial_\nu \ln\left(\alpha - \frac{\phi^2}{6}\right)\right]. \tag{2.13}$$

computing the derivatives of logarithms as

$$\begin{aligned}
\partial_\nu \ln\left(\alpha - \frac{\phi^2}{6}\right) &= -\frac{\phi}{3(\alpha - \frac{\phi^2}{6})}\partial_\nu\phi, \\
\partial_\mu\partial_\nu \ln\left(\alpha - \frac{\phi^2}{6}\right) &= -\frac{6\alpha + \phi^2}{18(\alpha - \frac{\phi^2}{6})^2}\partial_\mu\phi\partial_\nu\phi - \frac{\phi}{3(\alpha - \frac{\phi^2}{6})}\partial_\mu\partial_\nu\phi.
\end{aligned} \tag{2.14}$$

and substituting them yields

$$(\alpha - \frac{\phi^2}{6})R_J = (\alpha - \frac{\phi^2}{6})^2 R_E - (\alpha + \frac{\phi^2}{3})g_E^{\mu\nu}\partial_\mu\phi\partial_\nu\phi - (\alpha - \frac{\phi^2}{6})\phi g_E^{\mu\nu}\partial_\mu\partial_\nu\phi. \tag{2.15}$$

The next step is to convert the Jordan frame metric determinant into Einstein frame by $\sqrt{-g_J} = (\alpha - \frac{\phi^2}{6})^{-2}\sqrt{-g_E}$. Then we obtain

$$L = \frac{\sqrt{-g_E}}{2}\left[R_E - \frac{\alpha + \frac{\phi^2}{3}}{(\alpha - \frac{\phi^2}{6})^2}g_E^{\mu\nu}\partial_\mu\phi\partial_\nu\phi - \frac{\phi}{\alpha - \frac{\phi^2}{6}}g_E^{\mu\nu}\partial_\mu\partial_\nu\phi - \frac{1}{\alpha - \frac{\phi^2}{6}}g_E^{\mu\nu}\partial_\mu\phi\partial_\nu\phi - 2f\left(\frac{\phi}{\sqrt{6\alpha}}\right)\right]. \tag{2.16}$$

If we integrate the third term discarding the surface integral along with $\partial_\mu g_E^{\mu\nu}$, it cancels out the fourth term and the remaining part is added to the second term to give

$$L = \frac{\sqrt{-g_E}}{2}\left[R_E - \frac{\alpha}{\left(\alpha - \frac{\phi^2}{6}\right)^2} g_E^{\mu\nu}\partial_\mu\phi\partial_\nu\phi - 2f\left(\frac{\phi}{\sqrt{6\alpha}}\right)\right]. \tag{2.17}$$

We rescale the coordinate axis as $x_\mu \to \frac{x_\mu}{\sqrt{\alpha}}$ and recognize the last term as the field potential energy to obtain

$$L = \frac{\sqrt{-g}}{2}\left[R - \frac{g^{\mu\nu}\partial_\mu\phi\partial_\nu\phi}{\left(1 - \frac{\phi^2}{6\alpha}\right)^2} - V\left(\frac{\phi}{\sqrt{6\alpha}}\right)\right], \tag{2.18}$$

where we dropped the subscript E since we will primarily work in the Einstein frame. This long-sought action has poles in the kinetic term introducing non-trivial geometry into the field space. As it turns out the Poincare disk best describes this unique geometry.

From a practical side, it is better to bring the action to its canonical form which is well-studied in cosmology. To do that, we introduce a new canonically normalized field by solving, $\frac{\partial\phi}{\left(1-\frac{\phi^2}{6\alpha}\right)^2} = \partial\varphi$, to obtain

$$\phi = \sqrt{6\alpha}\,\tanh\frac{\varphi}{\sqrt{6\alpha}}\,. \tag{2.19}$$

This transformation will move the poles from $\phi = \pm\sqrt{6\alpha}$ to $\varphi = \pm\infty$ explicitly showing the plateau where inflation occurs with the field rolling slowly.

2.3 Key features of α

2.3.1 Interpretation

As we know from special relativity, the underlying geometry to study physical processes is flat Minkowski space and different frames are related to each other by Lorentz transformation to preserve the proper distance. However, this distance preservation - Lorentz transformation - has a hyperbolic structure. In other words, we can study a physical event in both flat and hyperbolic geometries with only different concepts, such as, velocity and rapidity. In the latter case, the preserved quantity under Lorentz boost is the hyperbolic angle due to its additive nature. This is an important feature of conformal

symmetry as mentioned earlier. The mapping between two spaces is the hyperbolic tangent, $v = c \tanh \eta$, where v is the object's velocity and η corresponds to the rapidity which is a velocity representation in hyperbolic geometry. So if we were to study relativistic motion, we can equivalently switch to hyperbolic structure by adopting rapidity instead of velocity which is more convenient since it has additive properties. In this regard, it is crucial to have a convenient representation of hyperbolic geometry. Poincare disk is the most well-known technique for this purpose. We start with a hyperboloid defined in flat space as

$$X^2 + Y^2 - T^2 = -1, \tag{2.20}$$

and it can be mapped onto a disk using the stereographic projection $x = \frac{X}{1+T}$ and $y = \frac{Y}{1+T}$ (this procedure is similar to how we obtain 2D map of the Earth). Then the corresponding metric will have the form

$$dz^2 = 4\frac{dx^2 + dy^2}{(1 - (x^2 + y^2))^2}. \tag{2.21}$$

This reminds us of the kinetic term in 2.18. Turns out, the Poincare disk best describes the field ϕ's underlying geometry. As we move towards the disk's boundary, the field value becomes infinite although the circle has a finite radius. Information gets distorted since we are mapping an infinite hyperboloid onto a unit disk but the angle between intersecting curves is preserved. Thus, one is free to speculate that the inflationary scenarios can happen at the boundaries of the disk where the field's potential approaches its plateau.

From a dynamical perspective, we note that depending on the two limiting values of α, it has two distinct physical interpretations [81],

$$\begin{cases} \alpha \to 0, & \tanh \frac{\varphi}{\sqrt{6\alpha}} << \frac{\varphi}{\sqrt{6\alpha}}, \quad \text{"ultra-relativistic" limit} \\ \alpha \to \infty, & \tanh \frac{\varphi}{\sqrt{6\alpha}} \approx \frac{\varphi}{\sqrt{6\alpha}}, \quad \text{"non relativistic" limit.} \end{cases} \tag{2.22}$$

It is evident that the ultra-relativistic limit can likewise be achieved when the field value approaches a very large number with fixed α. In this sense, the situation is similar to an object accelerated close to the speed of light, "things" become different, in other words, time stops. In the case of the field space, approaching the boundary of the Poincare disk creates a unique condition for high-energy state of the universe - inflation.

From a geometrical perspective, the Poincare disk can locally represent Kahler moduli space used in supergravity and string theory where the main idea of α-attractor stems from [65–67]. Although the Poincare disk has a constant curvature $R_P = -1$, the α

parameter is related to the Kahler curvature as

$$R_K = -\frac{2}{3\alpha} \tag{2.23}$$

Then depending on the two limiting cases, we have

$$\begin{cases} \alpha \to 0, & \text{high curvature limit} \\ \alpha \to \infty, & \text{low curvature limit.} \end{cases} \tag{2.24}$$

Another interpretation for α is its role in controlling the position of the singular term in 2.18 which corresponds to the Ultraviolet cutoff [83]. In other words, we can control the threshold between low and high-energy quantum field theory. From symmetry considerations, it is speculated that α takes discrete values [84, 85]. In the discussed Poincare disk scenario, this parameter takes $3\alpha = 1, 2, \ldots 7$ with $\alpha = 1$ corresponding to Starobinsky and Higgs inflation models.

2.3.2 Connecting n_s, r, and w_∞ with α

Any specific details of a general potential are washed away when we consider the limit $\varphi \to \pm\infty$. The positive infinite corresponds to high energy scale of inflation while the negative infinity leads to the low energy scale of dark energy . In both cases, the Taylor expansion of the potential around these limiting cases will have similar expressions with only a sign difference. In the vicinity of the boundary $\phi = \pm\sqrt{6\alpha}$, the $\phi(\varphi)$ relation becomes

$$\phi = \pm\sqrt{6\alpha}\left(1 - 2e^{\mp\sqrt{\frac{2}{3\alpha}}\varphi}\right), \tag{2.25}$$

up to a higher order terms $\mathcal{O}\left(e^{-2\sqrt{\frac{2}{3\alpha}}\varphi}\right)$. Then Taylor expanding the potential $V(\phi)$ around these boundaries gives

$$V = V_\pm \mp 2\sqrt{6\alpha}V'_\pm e^{\mp\sqrt{\frac{2}{3\alpha}}\varphi}, \tag{2.26}$$

where $V'_\pm \equiv \partial_\phi V\big|_{\phi=\pm\sqrt{6\alpha}}$ and $V_\pm = V(\pm\sqrt{6\alpha})$.

Now, we can find the imprints of α-attractor on the inflationary observables – spectral index n_s and tensor-to-scalar ratio r. Focusing on the inflationary part of the potential, we compute

$$\frac{d\varphi}{dN} = \frac{V'}{V} = \frac{4V'_+ e^{-\sqrt{\frac{2}{3\alpha}}\varphi}}{V_+ - 2\sqrt{6\alpha}V'_+ e^{-\sqrt{\frac{2}{3\alpha}}\varphi}}, \tag{2.27}$$

where N is the remaining number of e-folds till the end of inflation such that $dN < 0$, generally of order N = 50–60. In the limit $\varphi \to \infty$, we can neglect the second term in the denominator leaving us with,

$$\frac{d\varphi}{dN} = \frac{V'}{V} = 4\frac{V'_+}{V_+}e^{-\sqrt{\frac{2}{3\alpha}}\varphi}, \tag{2.28}$$

solving for $e^{-\sqrt{\frac{2}{3\alpha}}}$ in terms of N gives

$$e^{-\sqrt{\frac{2}{3\alpha}}\varphi} = \frac{V_+}{V'_+}\sqrt{\frac{3\alpha}{2}}\frac{1}{4N}, \tag{2.29}$$

substituting it into the slow-roll parameter yields

$$\varepsilon_H = \frac{1}{2}(\frac{d\varphi}{dN})^2 = \frac{3\alpha}{4}\frac{1}{N^2}. \tag{2.30}$$

Likewise, we can find the second slow-roll parameter as

$$\eta_H = \frac{V''}{V} - \frac{1}{2}\left(\frac{V'}{V}\right)^2 = -\frac{1}{N} - \varepsilon_H. \tag{2.31}$$

We recall that $r = 16\varepsilon_H$ and $n_s = 1 - 4\varepsilon_H + 2\eta_H$. Computing n_s to first order in N, finally gives

$$n_s = 1 - \frac{2}{N}\ , \quad r = \frac{12\alpha}{N^2}\ , \tag{2.32}$$

To derive the asymptotic value of the dark energy equation of state far into the future w_∞, we set $V_- = 0$ corresponding to the zero cosmological constant $\Lambda = 0$ to avoid $w_\infty = -1$ [86]. At late time, we have an exponential potential $V \sim e^{\lambda\varphi}$ that flattens as $\varphi \to -\infty$ to give an asymptotic power-law inflation [87]. It is well known, in that regime, the equation of state approaches its asymptotic value,

$$w_\infty = -1 + \frac{\lambda^2}{3} = -1 + \frac{2}{9\alpha}. \tag{2.33}$$

Therefore, another observable quantity is determined through α, making this framework even more attractive.

2.4 α-Attractors as Quintessential Inflation

Our focus is particularly on the quintessential inflation based on the α-attractor framework, where the field rolls from the high-energy inflationary plateau to its $\sim 10^{110}$ times smaller potential energy corresponding to the late-time dark energy. One way to achieve

this is to include the Λ term by hand to account for the second plateau. We avoid that route by taking only dynamical energy with zero cosmological constant. We achieve it by choosing an exponential potential to have an attractor behavior at late times to avoid fine-tuning. Regarding the observables n_s and r, we already have an attractor to wash away any initial misbehavior, imposed by the symmetry of our framework. These two considerations are embedded in the potential,

$$\begin{aligned} V(\phi) &= M^2 e^{-2g} \left[e^{g\left(\frac{\phi}{\sqrt{6\alpha}}+1\right)} - 1 \right] \\ V(\varphi) &= M^2 e^{-2g} \left[e^{g\left(\tanh\left(\frac{\varphi}{\sqrt{6\alpha}}\right)+1\right)} - 1 \right], \end{aligned} \tag{2.34}$$

first studied in [72] as Exp-model II. We name it ExpLin due to its unique shape at two extremes – at early times it approaches its plateau as an exponential while at late times it becomes a linear function in $\phi + \sqrt{6\alpha}$. The advantage of the linear potential is its "resilience" to quantum bumps or corrections in the field due to its approximate shift symmetry near the pole [88]. The inflationary energy scale is given by M^2, while $M^2 e^{-2g}$ corresponds to the current energy scale of the dark energy such that the parameter g is on the order of ~ 125.

Given the observables of two inflationary epochs in terms of α in Eqs. 2.32–2.33, we can connect the tensor-to-scalar ratio with the asymptotic value of the dark energy equation of state as

$$1 + w_\infty = \frac{8}{3N^2 r} = 0.22 \left(\frac{51}{N}\right)^2 \left(\frac{4.6 \times 10^{-3}}{r}\right) . \tag{2.35}$$

The parameter values used in this calculation were borrowed from the Starobinsky model predictions [89]. We see a simple relation between the two observables, that is, if we stand a chance to observe CMB polarization B-modes (larger r), then it is hard to distinguish dynamic dark energy from the cosmological constant ($w = -1$) and vice versa.

To analyze the model, we solve the equation of motion, Klein-Gordon equation, corresponding to the quintessence scalar field. We bring this second-order differential equation into its coupled autonomous system of first-order differential equations for the kinetic and potential energies as in [90]. Introducing $x = \varphi'/\sqrt{6H^2}$, $y = \sqrt{V(\varphi)/(3H^2)}$ as our new variables, we can write

$$x' = -3x + \sqrt{\frac{3}{2}}\lambda y^2 + \frac{3}{2}x\left[2x^2 + \gamma(1 - x^2 - y^2)\right] \tag{2.36}$$

$$y' = -\sqrt{\frac{3}{2}}\lambda y x + \frac{3}{2}y\left[2x^2 + \gamma\left(1 - x^2 - y^2\right)\right] . \tag{2.37}$$

Where a prime denotes a derivative taken with respect to $\ln a$, e-fold time. In this autonomous system, the dark energy equation of state has a simple form,

$$w = \frac{x^2 - y^2}{x^2 + y^2}. \tag{2.38}$$

We denote the present fractions of matter and radiation energy density relative to the critical density of the universe as Ω_m and Ω_r, respectively. Then, the background fluid's equation of state γ (without the field) and the fractional potential slope λ can be written as

$$\gamma = 1 + \frac{1}{3}\frac{1}{1 + \frac{\Omega_m}{\Omega_r} e^{\ln a}} \tag{2.39}$$

$$\lambda = -\frac{V_{,\varphi}}{V} . \tag{2.40}$$

One may prefer an analogue system with three equations that can be solved numerically [90]. We have also implemented this system to test for accuracy by defining $\Gamma = VV_{,\varphi\varphi}/V_{,\varphi}^2$. Then the slope parameter λ evolves according to

$$\lambda' = -\sqrt{6}\,\lambda^2(\Gamma - 1)x . \tag{2.41}$$

Numerical solutions obtained by both systems show identical results to the desired precision. All the results in this work are obtained by solving the two-equation system.

2.4.1 Viable α Values and Feasible Initial Conditions

To find the field evolution, we have to supply the system of differential equations with initial conditions φ_i', φ_i, and with the model parameter α. The following argument determines initial conditions. After the end of inflation, the inflaton transitions into its kination phase where its kinetic energy dominates due to the steepness of the potential, then the potential flattens again making the Hubble friction the dominant term in the equation. The field freezes at a certain time in its evolution making the results independent of the choice for φ_i', and we set it to zero. We also expect the evolution independent of $\varphi_i = \varphi_f$ over a certain range due to the attractor behavior of the potential at late times. The initial conditions are set at $\ln a_i = -15$ corresponding to $z \approx 3 \times 10^6$, well inside the radiation epoch. We focus on the specific values of $\alpha = [1/3, 7/3]$ to match with the symmetric considerations coming from the Poincaré disk. Lastly, we fix the fiducial value

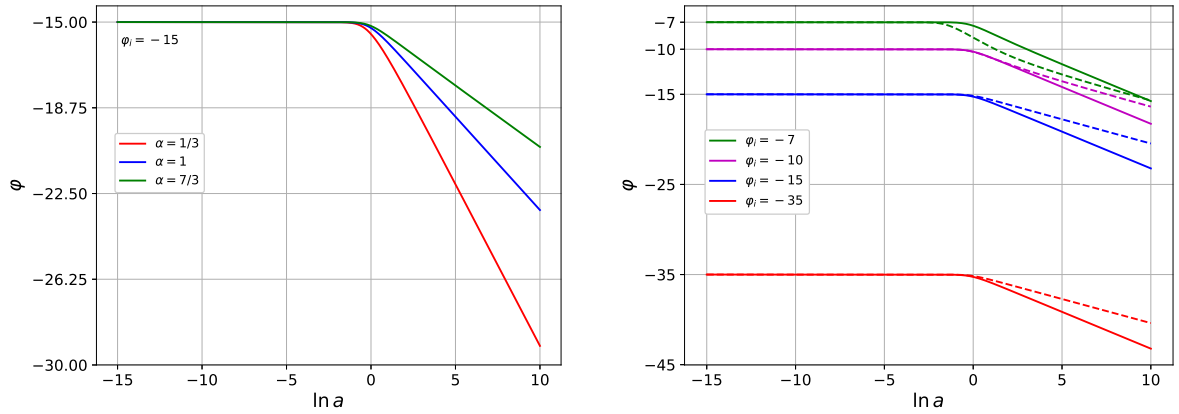

Figure 2.1: The field evolution influenced by Hubble friction and the slope of potential energy. Left panel illustrates the dependence on α with fixed $\varphi_i = \varphi_f = -15$. While the right panel shows the dependence on ϕ_f with fixed $\alpha = 1$ (solid) and $\alpha = 7/3$ (dashed).

of the fractional matter energy density to $\Omega_m = 0.3$ while adopting $H_0 = 68$ km/s/Mpc where necessary.

In Fig. 2.1, we show the field evolution $\varphi(\ln a)$ corresponding to different values of α and φ_f. As we can see the field is frozen for most of the time, thawing only recently. We will further discuss such behavior in Sec. 2.4.2 known as the thawing field in literature [68, 91, 92]. The left panel displays strong thawing behavior of the field for large α values. However, the right panel displays a similar behavior: bigger φ_f causes the field to thaw sooner and more strongly (better seen with higher α value). In both cases, the similar behavior is attributed to the potential's sensitivity to steepness caused by these parameters.

The dynamics of the dark energy is best distinguished by its equation of state parameter $w(\ln a)$. In Fig. 2.2, we display this parameter depending on α values and initial condition φ_f. Since the field is frozen initially, we observe $w = -1$, as expected. Far into the future, it will approach its asymptotic value $w_\infty = -1 + 2/(9\alpha)$. However, as we saw in the previous figure, the steepness of the potential plays a crucial role: the field may overshoot first and then relax to its attractor value. For $\varphi_f \lesssim -15$, one can notice that the equation of state shows a similar shape, while for $\varphi_f \gtrsim -10$ the overshooting is so extreme near the present that it becomes irrelevant to consider this range from an observational point of view.

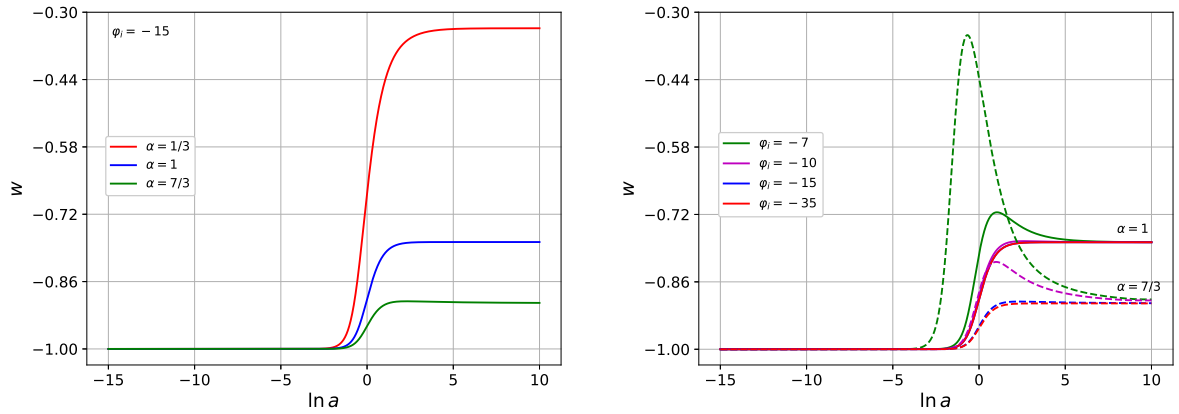

Figure 2.2: The equation of state of dark energy shows cosmological constant-like behavior in the past, only to relax to less negative values later, to approach its asymptotic value in the future. The left panel shows the effect of α, with smaller values $\alpha < 1$ showing huge deviations from $w = -1$, rendering them difficult to reconcile with observations. The right panel presents φ_f dependence of the w evolution. The less negative φ_f produces potentials with the steeper slopes causing w to overshoot its attractor value, with $\varphi_f > -10$ being unviable observationally while $\varphi_f < -15$ producing near identical outcomes.

2.4.2 Connection Between Inflation and Dark Energy

We saw how the ExpLin α-attractor model connects two parameters, tensor-to-scalar ratio r and asymptotic value of dark energy equation of state w_∞, both belonging to events separated by billions of years. Although, r is an observable, w_∞ is not, in the sense that observations do not constrain it directly but they only constrain $w(a)$ through cosmic distances and growth factors. Therefore, it is best to study $w(a)$ and ways to connect it to its asymptotic value.

The Refs. [78, 93] demonstrated that the form $w(a) = w_0 + w_a(1-a)$, called the CPL parametrization, is a good approximation for the observational probes such as distances and growth factors relative to the exact equation of state parameter with $\sim 0.1\%$ accuracy for thawing fields. Accordingly, we start by investigating the relationship of the fitting parameters w_0 and w_a to the model parameters.

As a first step, we look for patterns that can help connect $w_\infty(\alpha)$ to w_0. Looking at Fig 2.2, we can already find a hint that for viable α and φ_f, where overshooting the attractor value is suppressed, the relation between the two values of w is expected to be simple. To see this, we compute $P \equiv (1+w_0)/(1+w_\infty)$ and plot it in Fig. 2.3. As can be seen, we find that for a viable range of α and φ_f ranges, we indeed have a simple relation,

$$1 + w_0 \approx 0.5(1 + w_\infty) \ , \tag{2.42}$$

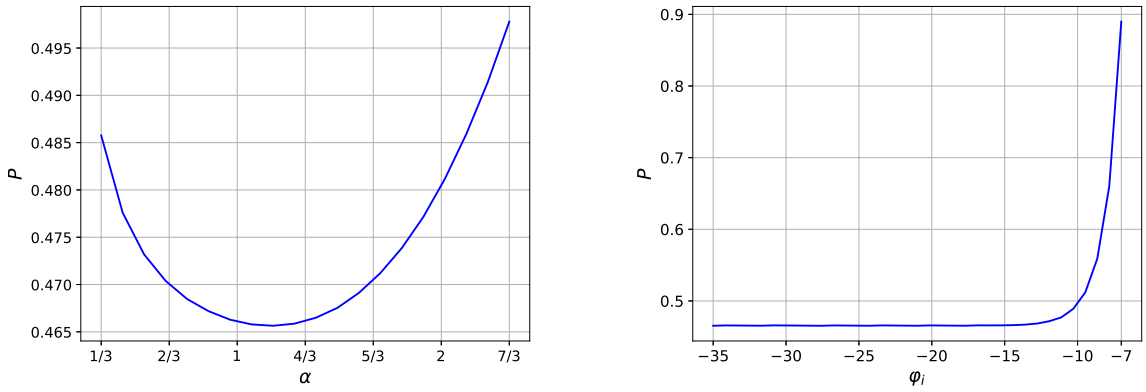

Figure 2.3: Connecting the present value of the dark energy equation of state to its asymptotic value through the ratio $P \equiv (1+w_0)/(1+w_\infty)$. The ratio is almost constant for the chosen α's with fixed $\varphi_f = -15$ (left panel) and viable φ_f with fixed $\alpha = 1$ corresponding to Starobinsky model(right panel).

to a desired accuracy. Now, we can relate two different, seemingly unrelated, observables, i.e. r to w via Eq. 2.35 to obtain

$$1 + w_0 \approx \frac{4}{3N^2 r} = 0.10 \left(\frac{51}{N}\right)^2 \left(\frac{4.6 \times 10^{-3}}{r}\right) \ . \tag{2.43}$$

When it comes to the parametrized time-varying dark energy equation of state, Ref. [78] demonstrated a narrow relation $w_a \approx -(1+w_0) \times (1.5 - 1.6)$ for thawing fields. We find $w(a)$ by solving the coupled equations of motion and check if this relation also holds for our ExpLin model which corresponds to a thawing field. Concerning the CPL parameters, w_0 is just the present value of the dark energy equation of state $w(a=1)$. While w_a is determined in such a way to capture a universal pattern all model parameters share as shown by Ref. [78]. It is often wrongly interpreted as the first derivative in the Taylor expansion around today $w_a = w'(a=1)$. However, following Ref. [78], we define it from the phase space quantity w' as $w_a = -w'(a)/a$ evaluated at some $a = a_\star$ where the model parameter values show universal behavior. This doesn't affect the observables where w_0 and w_a are treated as the fitting parameters in $w(a) = w_0 + w_a(1-a)$, rather it is used as a theory interpretation tool, a calibration, to bring unique behaviors corresponding to different model parameters close together.

In Fig. 2.4, we plot the calibration ratio $Q \equiv w_a/(1+w_0)$ against $a_\star$ to identify a range of parameter values where we might observe the relation established in Ref. [78] for thawing fields. As can be seen, most of the model parameters produce the calibration ratios that lie close to each other for a range of $a_\star$. Slight deviations from the general trend

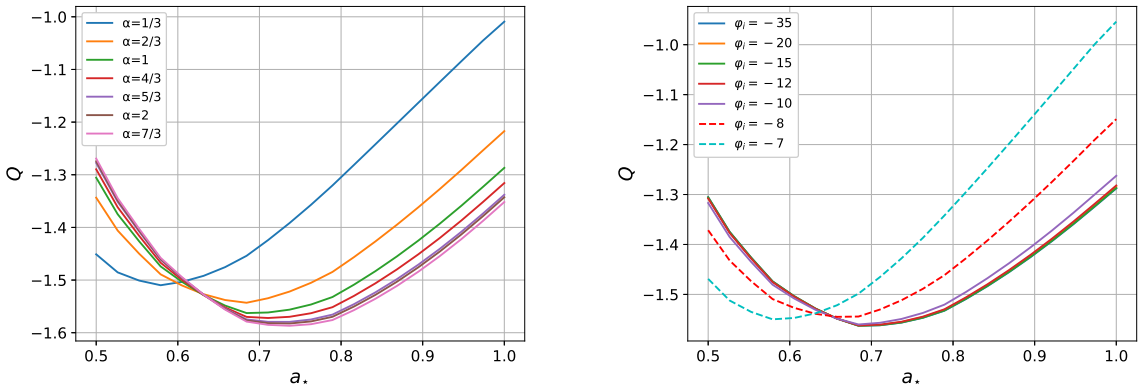

Figure 2.4: Demonstration of ExpLin model acting as the standard thawing field. The calibration given by the ratio $Q \equiv w_a/(1+w_0)$ is plotted as a function of $a_\star$, where we use $w_a = -w'(a_\star)/a_\star$. Plots for different α with $\varphi_f = -15$ [left panel] and for different φ_f with $\alpha = 1$ [right panel] both show nearly universal phase space feature at around $a_\star \approx 0.65$ over viable parameter ranges.

appear in the case of $\alpha = 1/3$ (fixed $\phi_f = -15$) and $\varphi_f = -7$ (fixed $\alpha = 1$). However, as shown in Fig. 2.2, these models have a strong deviation from $w = -1$ rendering them irrelevant for discussion. For viable ranges of α and ϕ_f, we can see an especially tight calibration at around $a_\star = 0.65$. Therefore, we can write the following approximation

$$w_a \approx -1.53(1+w_0) \ , \tag{2.44}$$

establishing the validity of the thawing field parametrization demonstrated in Ref. [78]. Now, we can rewrite Eq. 2.43 as

$$w_a \approx \frac{-6}{3N^2 r} = -0.16 \left(\frac{51}{N}\right)^2 \left(\frac{4.6\times10^{-3}}{r}\right) \ . \tag{2.45}$$

Thus, with the dark energy equation of state characterized by CPL parameters, we have an interconnected relation among w_0, w_a, and r. We check this relation by solving the coupled system for a range of α and ϕ_i values. In Fig. 2.5, the model predictions are given in the w_0–w_a plane, with colors and symbols corresponding to different α and ϕ_i values, respectively. As can be seen, these predictions lie close to each other highlighting the potency of calibration parameter w_a demonstrated in Eq. 2.44. The deviations $w_0 > -0.8$ seen in the phase space, again, correspond to models with unviable parameter ranges like $\alpha = 1/3$ and $\varphi_f > -8$. Otherwise, all models follow the w_0–w_a relation independent of φ_f for $\varphi_f \lesssim -10$.

Fig. 2.6 demonstrates the correspondence between the primordial gravitational wave and the CPL parameters. We used $\varphi_f = -15$ (however the results are independent of

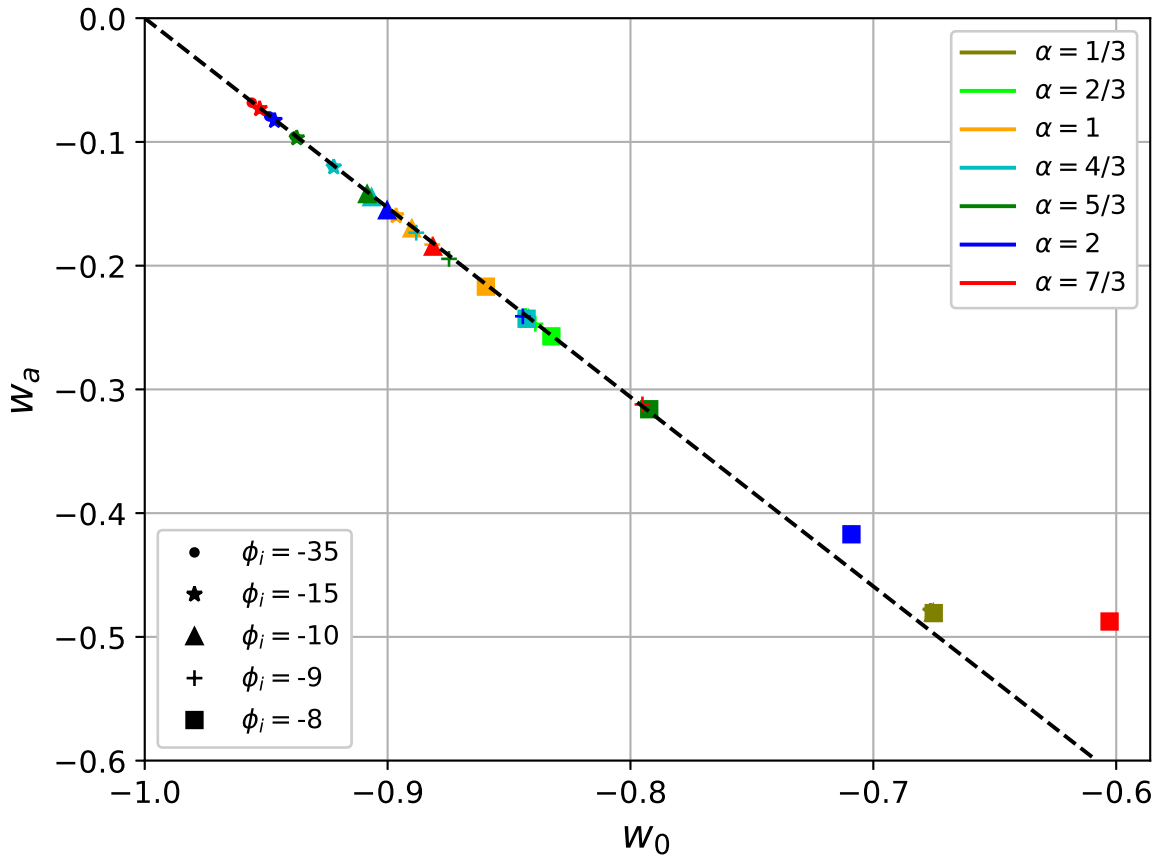

Figure 2.5: Demonstrating the validity of the relation in Eq. 2.44 by numerically solving the system of equation for $w(a)$. Colors and symbols correspond to α and ϕ_f, respectively. Deviations from Eq. 2.44 (outside the dashed line) occur in the unviable range of the parameters (in the case of $\alpha = 1/3$, all symbols are stacked on top of each other).

φ_f over its viable range) and plotted the derived r, w_0, w_a values for a given α. If we fix α in Eq. 2.32, the tensor-to-scalar ratio r becomes a function of only N while there is no such dependence in the CPL parameters. The result is clearly shown in the plot where the band covers $N = [50, 60]$ (a reasonable range for inflation) and where the solid curve connects the different α's for $N = 51$. In both panels, we can clearly see the inverse relation between dark energy dynamics and the primordial gravitational wave strength. This relation suggests if we stand a good chance to observe the primordial gravitational waves in the next generation experiments, then the odds are against dynamical dark energy, while if we fail to find gravitational waves created during inflation, then the odds are against cosmological constant. Since the expectation for the next generation experiments, such as the CMB and cosmic distance/structure surveys, are very high with uncertainties lowering to $\sigma(r) \approx 5 \times 10^{-4}$, $\sigma(w_0) \approx 0.08$, $\sigma(w_a) \approx 0.2$ (e.g. [94–97]), there is hope to detect both.

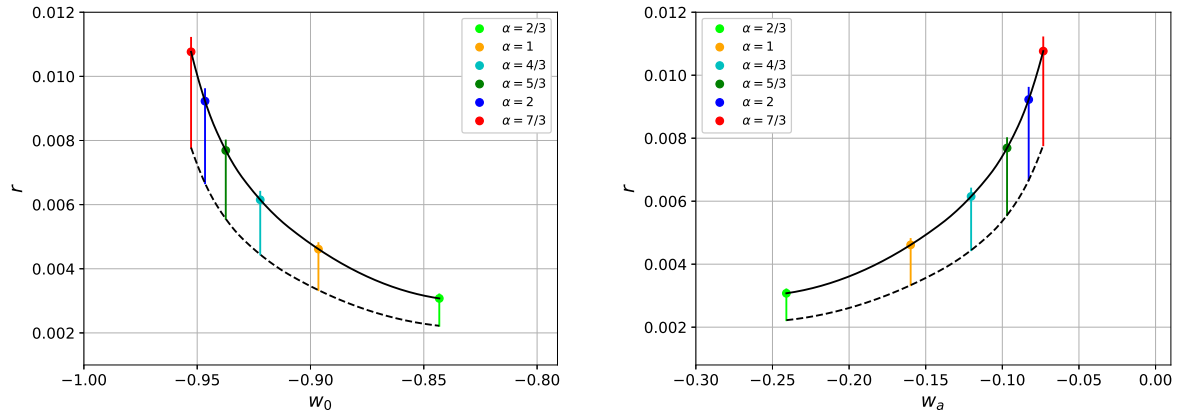

Figure 2.6: The connection, between the strength of inflationary gravitational waves r and the dark energy equation of state parameters w_0 (left panel) and w_a (right panel), is tight as shown by the curves. In both panels, φ_f is fixed to $\varphi_f = -15$, however, we expect the same result over its viable range. Solid (dashed) black curves link the different α values for $N = 51$ (60), with vertical colored lines running over $N = [50, 60]$ for constant α.

2.4.3 Constraints from Observations

This subsection aims to constrain the ExpLin model parameters from observations, particularly, through the CMB observables n_s and r. We find the model parameter α and the number of e-folds N as a function of CMB observables. From Eq. 2.32, we can establish

$$N = \frac{2}{1-n_s} = 57\,\frac{1-0.965}{1-n_s} \tag{2.46}$$

$$\alpha = \frac{r}{3(1-n_s)^2} = 1.24\,\frac{r}{4.6\times 10^{-3}}\left(\frac{1-0.965}{1-n_s}\right)^2 . \tag{2.47}$$

Furthermore, the relation between the inflation mass scale M and observed CMB temperature perturbation amplitude A_s is given by [72]

$$M^2 = \frac{144\pi^2\alpha N}{(2N-3\alpha)^3}\,A_s \approx 10^{-10}\,\alpha. \tag{2.48}$$

The value M is also constrained by the measurements since we already connected α with observation through Eq. 2.47,. Lastly, the parameter g in the exponential potential plays the role to fine-tune the present energy scale of dark energy once we transition to the late-time acceleration. Because CMB measurements require the fractional dark energy density to be around $\Omega_{d,0} = 0.7$, we can estimate g using the bisection method. In the top right panel of Fig. 15 in Ref. [72], the parameter g is shown as a function of the inflation energy scale M and initial field value (when the field thaws) φ_f (with the difference that they use γ instead of g and notate φ_f as φ_F).

Previously, we established a tight relation between the parametrization of dark energy equation of state w_0, w_a and its future asymptotic value w_∞ thus connecting w_0, w_a with r. Experimentally, w_0 and w_a will be determined by the growth of structure and observations concerning the cosmic distances. While the nature of primordial gravitational waves r will be tightly constrained by the next generation CMB B-mode polarization experiment. Although these observations are expected to give a strong consistency test, the current state of affairs in cosmological surveys already puts tight bounds on the dynamical dark energy suggesting it shouldn't deviate too much from the cosmological constant. For instance, for thawing fields with $w_0 = -0.8$ and hence $w_a \approx -0.3$ obtained by the reduced distance to CMB recombination shows a deviation of 1.1% from the cosmological constant predictions which are well above the constraints of Planck measurements [98]. Meanwhile, by changing Ω_m just a small amount 0.02 between the ($w_0 = -0.8$, $w_a = -0.3$) model and ΛCDM, one is expected to move within 0.4% distance constraint. In this case, the distance, calculated using the first model, is equivalent to the constant $w_0 = -0.9$ model. It suggests the models that produce deviations from the cosmological constant by more than $w_0 > -0.8$ is expected to be disfavored.

Thus, α attractor model with ExpLin-like potential indicates a strong connection between the primordial gravitational wave and the dark energy. Observationally, it says if an experiment is able to find an imprint of one then a "parameter map" tells another experiment where to search for the signature of the other. All these are possible thanks to the model behaving like a thawing field which gives the experimenter more leverage on the dynamics in terms of both the calibration parameter w_a and the present value w_0 of dark energy.

2.5 Conclusions

Introducing additional symmetry, in the form of conformal invariance, to the action significantly enhances its predictive ability due to the constraints put by the high energy physics. We heuristically derived the α attractor action, first, by making the canonical kinetic term invariant under conformal transformation, second, by enhancing the field space structure by introducing $SO(1,1)$ symmetry through a new field. Then fixing this new field to a parameter α, we transformed the action into Einstein's frame, overall ef-

fect being an action with a pole in the kinetic term. In all steps in the derivation, we followed the arguments of Ref. [83]. It turns out the parameter α has a deep physical interpretation coming from different considerations: curvature of field space, hyperbolic angle or rapidity, pole shifting, all involving α in one way or another. Next, by solving the equation of motion numerically, we established connection between the observables of inflation and late time dark energy.

Considering we are on the cusp of precision experiments, detection of primordial gravitational waves or dynamic feature of cosmological constant would significantly boost our understanding of these two important cosmic events. Quintessential inflation unifies these two epochs while α attractor provides physical framework with definitive predictions. In our investigation, we incorporated both by choosing the ExpLin potential. With this potential, we have two distinct regions: exponential part at early times explains inflation and the linear part at late time explains dark energy. According to this model, late time dark energy emerges as the thawing field with a calibrated relation $w_a = -1.53(1 + w_0)$ and asymptotic attractor in the future with $1 + w_0 \approx 0.5(1 + w_\infty)$. Since w_∞ and r both have α dependence, this model provides a tight relation between the observables of two epochs. We have confirmed these relations through numerical analysis and showed the system to be insensitive to initial conditions. As a matter of fact, those α values that lie in the higher end of the Poincaré disk range will forecast stronger primordial gravitational waves while values at the lower end predict dynamical nature for dark energy. Values that lie in the middle range, including Starobinsky inflation ($\alpha = 1$), will provide accessible signals for both events.

Chapter 3

Model Independent Dark Matter Properties from Cosmic Growth

3.1 Introduction

With the emergence of precision-guided observational cosmology, new phenomena are being persistently detected with possible explanations beyond common understanding of the universe. Dark matter is one of the examples which, over time, became an inseparable ingredient of the standard cosmological model [99–101]. Current understanding of galaxy properties along with large structure formation cannot avoid the possible presence of dark matter in the universe [102]. The potential existence of dark matter is so appealing that the standard model ΛCDM requires ~ 6 times more of its contribution to the universe's energy budget than the baryonic matter. However, the only hint we receive from cosmic surveys come from dark matter's gravitational interaction with its surroundings. Other basic properties such as spin, charge, and number density of dark matter are poorly constrained.

There are a plethora of dark matter models in literature aiming to address apparent tensions between the parameter estimations of small and large-scale surveys. These models ascribe various cosmic properties to dark matter, such as, nonstandard interactions, cannibalism, unusual decaying characteristics, evolving equation of state, etc [103–107]. They all should "walk on eggshells" to keep the well-established data about dark matter intact while at the same time to explain apparent observational or theoretical difficulties. Another way to maneuver among these issues is to take a phenomenological point

of view which is more observation-oriented by retaining the general notion but slightly modifying the part that can be data-constrained. The so-called "generalized dark matter" approach proposed in Ref. [108] deals with an evolving equation of state which includes a sound speed in the fluid perturbations and viscous sound speed. This approach is widely explored in [109–111].

This work aims to explore the constraining capabilities of cosmic growth observations on two properties dark matter possesses. These include the equation of state (w_{dm}) and clustering strength (F_{cl}). Standard theory assumes pressureless dark matter with its energy density evolving like baryons ($w_{\rm dm} = 0$) and clustering with Newtonian gravitational strength ($F_{\rm cl} = 1$). We modify both assumptions slightly while keeping the analysis as model-independent as possible. Without presuming any functional forms for these concepts, we will allow deviations in certain redshift bins. Afterward, we show how measurements like DESI, Euclid, and peculiar velocity can constrain binned clustering strength.

Section 3.2 provides a brief review of the density perturbation equation and where we can find spots to introduce modifications grounded on physical principles. The following two sections are devoted to studying the modified gravitational clustering strength (Section 3.3) and modified dark matter equation of state (Section 3.4). Our analysis is summarized in Section 3.5.

3.2 Dark Matter and Cosmic Growth

Structure growth surveys carry rich cosmological insight. Not only do they probe the cosmic expansion rate through the universe's matter content and its density evolution, but these surveys also provide additional information about their clustering properties. The latter can identify crucial points about the role of gravitation, interaction, and self-interaction in structure growth. This study considers a flat universe filled with dark matter, baryons, and cosmological constant. We will avoid a scenario where each matter component may have interaction terms including self-interaction.

In linear density perturbation analysis, structure growth is formulated by the sub-horizon perturbation equation. Introducing $\delta = \delta\rho_m/\rho_m$ as the matter overdensity, t as the cosmic time and identifying the Hubble parameter as $H = \dot{a}/a$, gravitational constant

as G_N we can write the perturbation equation as

$$\frac{d^2\delta(t)}{dt^2} + 2H(t)\,\frac{d\delta(t)}{dt} - 4\pi G_N \rho_m(t)\,\delta(t) = 0\ , \tag{3.1}$$

where $\rho_m = \rho_b + \rho_{\rm dm}$ is given as a sum of baryons and dark matter.

As our previous study suggests (Chapter 2), considering a dynamical scalar field can have rich possibilities to unite different sectors of cosmology. This will, however, significantly modify the above equation since, unlike the cosmological constant case, there is a contribution from dark energy perturbation. In those scenarios, the behavior of H will also be different from its standard form as it contains the dark energy. Nevertheless, as long as one is focused on matter growth, dark energy perturbation can have a negligible impact. Motivated by this consideration, we keep the dark energy sector "quiet" by assuming that dark energy is well described by the cosmological constant. We will solely focus on the dark matter sector by allowing its clustering strength deviate from the usual gravitational clustering as

$$G_N \rho_m \delta \to G_N\left(\rho_b\delta_b + F_{\rm cl}\,\rho_{\rm dm}\delta_{\rm dm}\right)\ . \tag{3.2}$$

To give a more general and model-independent investigation than Ref. [112] did, we will allow $F_{\rm cl}$ to be time-dependent and at the same time assume no specific model and study it purely phenomenologically. The consequences of this approach will be presented in Section 3.3.

The second option we have is to fix the gravitational sector as Newtonian and allow deviations in the dark matter equation of state which will modify its energy density evolution as

$$\rho_{\rm dm}(a) \;\; = \;\; \rho_{\rm dm}(a=1)\,a^{-3} \;\; = \rho_{\rm dm}(a=1)\,a^{-3}\,F_{\rm eos}(a)\ . \tag{3.3}$$

Upholding the principle, we again study modification part $F_{\rm eos}$ phenomenologically. Since the dark matter density appears both in $H(t)$ and in the source term in the evolution equation, the situation may not be as straightforward: we may not be able to attribute the changes to a single term like in the previous case. However, if we choose a path where we can keep $H(t)$ intact by altering the dark energy sector accordingly, this path will lead us back to our first approach where $F_{\rm cl}$ enters just the source term. Again, we consider the dark energy to be cosmological constant. We present the results of this extension in Section 3.4.

In both approaches, we adopt the standard evolution for baryon energy density $\rho_b \sim a^{-3}$ where its present value $\Omega_{b,0}h^2 = 0.02233$ is taken from the Big Bang Nucleosynthesis (BBN) and CMB measurements. We adopt $h = 0.7$ (therefore $\Omega_b = 0.0456$) and fix the total matter fractional density to $\Omega_{m,0}^{\rm LCDM} = 0.3$.

3.3 Dark Matter Clustering

We aim to constrain the clustering and equation of state deviations by galaxy redshift surveys. Those measurements map the large-scale structure over cosmic time, often characterized by the scale factor a or redshift range $z = a^{-1} - 1$. These data offer valuable insight into the clustering evolution determined by the growth rate $f = d\ln\delta/Hdt = d\ln\delta/d\ln a$. This quantity is commonly used in redshift space distortion (RSD) measurements. We assume that most of the structure growth happened during matter domination while dark energy domination acts to suppress this process. In this respect, it is more convenient to adopt the scale factor as a time variable, and normalize the matter overdensity over its matter-dominated value $\delta^{\rm md} \sim a$ by using the growth factor $g(a) = [\delta(a)/\delta(a_i)]/(a/a_i)$. When solving the growth equation, the initial time a_i is chosen deep inside the matter domination where $g = 1$ and $f = 1$. In terms of these new concepts, we can write the growth equation in the following form:

$$\begin{aligned} 0 &= a^2\frac{d^2g}{da^2} + \left(5 + \frac{1}{2}\frac{d\ln H^2}{d\ln a}\right) a\frac{dg}{da} \\ &\quad + \left(3 + \frac{1}{2}\frac{d\ln H^2}{d\ln a} - \frac{3}{2}\left[\Omega_b(a) + F_{cl}(a)\,\Omega_{dm}(a)\right]\right) g \ . \end{aligned} \tag{3.4}$$

The solution of this equation can be used to construct the growth rate as $f = 1 + d\ln g/d\ln a$. However, RSD measurements involve $f\sigma_8$ with an additional parameter $\sigma_8(a)$ defined as the mass fluctuation amplitude,

$$\sigma_8^2(a) = \int \frac{d^3k}{(2\pi)^3} P(k,a) W^2(kR_8), \tag{3.5}$$

where $W(kR_8)$ is the window function to filter out all the modes outside $R_8 = 8h^{-1}$ Mpc, while $P(k,a) = A_s T^2(k)\delta^2(a)$ is the power spectrum with the transfer function $T(a)$ and the CMB fluctuation amplitude A_s. Since $\sigma_8 \sim \delta$, we will have $f\sigma_8 \sim d\delta/d\ln a$ leaving us with an undetermined initial value $\sigma_{8,0}$. We can fix this constant, either, to its present value as measured by mass clustering, or, normalize it in terms of the

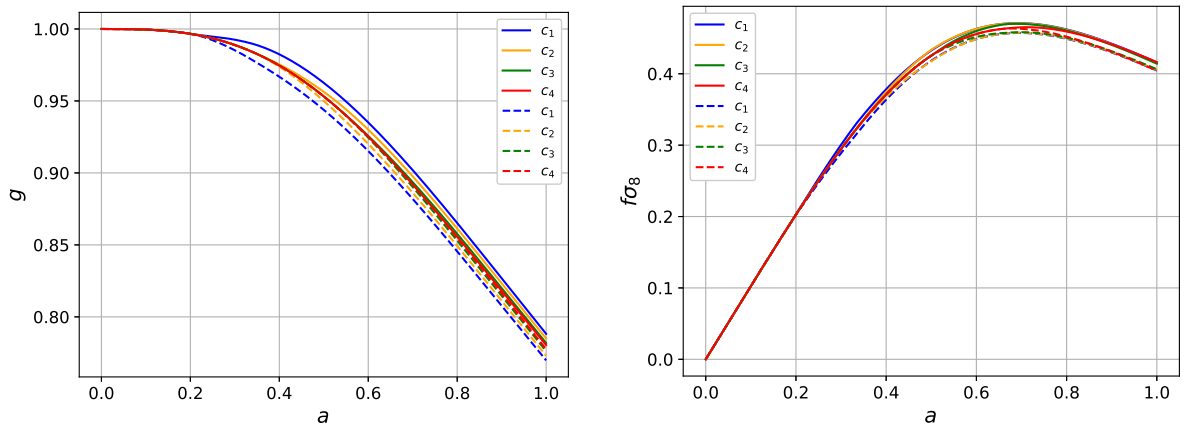

Figure 3.1: Dark matter clustering strength, $c_i = \pm 0.05$ (solid/dashed curves), shows a distinct influence on the growth factor $g(a)$ [left panel] and RSD factor $f\sigma_8(a)$ [right panel].

CMB fluctuation amplitude A_s to preserve the high redshift universe consistent with the standard cosmological model. We choose the second option which enables us to disentangle the effects of the late time processes from the initial conditions set by the CMB. So that any deviation in $\sigma_{8,0}$ is attributed only to the deviations in clustering strength. Taking all these into account, we can write

$$f\sigma_8(a) = \frac{\sigma_{8,0}^{\rm LCDM}}{g_0^{\rm LCDM}}\, ag\left(1 + \frac{d\ln g}{d\ln a}\right) , \tag{3.6}$$

where $g_0^{\rm LCDM} = 0.779$ and $\sigma_{8,0}^{\rm LCDM} = 0.8$ computed from the CMB physics.

3.3.1 Sensitivity to Deviations

Quantities $g(a)$ and $f\sigma_8(a)$ will be affected by the clustering strength in the source term. To study the deviations in dark matter clustering phenomenologically, we consider

$$F_{\rm cl}(a) = 1 + c(a) , \tag{3.7}$$

with $c(a)$ given by multiple intervals, each with constant amplitude c_i and time interval a (referred to as bins). We are interested in the epoch $a = [0.2, 1]$ and we divide it into four bins as $a = [0.2, 0.333], [0.333, 0.5], [0.5, 0.667], [0.667, 1]$. To keep CMB and BBN intact, we set the clustering deviation to zero for $a < 0.2$. Thus, we have the earliest bin deviation represented by c_1 and the latest bin by c_4. Here, the role of $F_{\rm cl}$ can be interpreted in two different ways: the entire dark matter participates in the growth of structures with different gravitational strength from G_N, or only a fraction of dark matter is suited for gravitational clustering, e.g. if there are distinct species of dark matter.

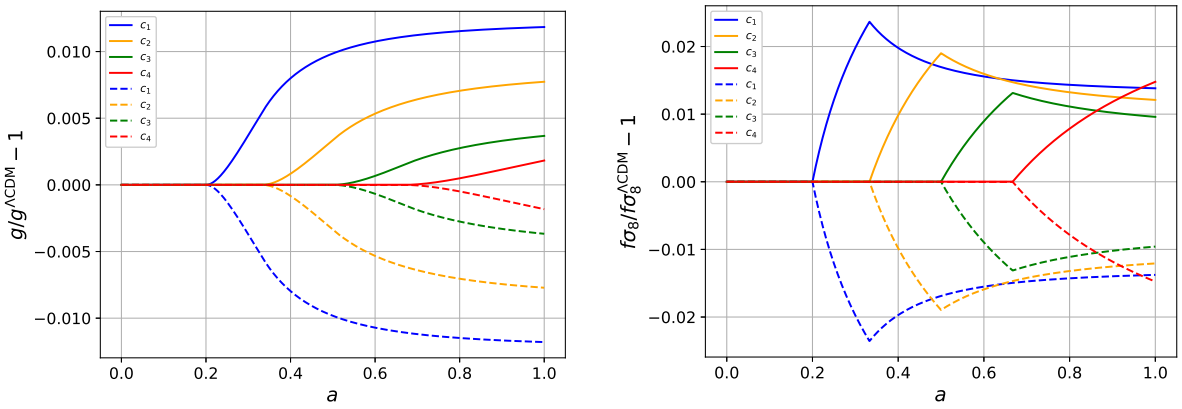

Figure 3.2: The same as in Fig. 3.1, but shown as fractional deviations from ΛCDM values.

At this point, it is important to note that the value of growth at a specific time is influenced by all the events that occurred at an earlier time since it is a dynamic process. In this regard, to determine the effect of a certain bin deviation on the growth, a tomographic survey spanning a wide range of redshift will be of particular importance.

The response of the growth factor g and RSD factor $f\sigma_8$ to the clustering deviation with amplitude $c_i = \pm 0.05$ is presented in Fig. 3.1. As said earlier, growth is a dynamic process therefore no wonder the earliest bin has the longest and most sustained impact. To see it more clearly, we plot the fractional deviation from ΛCDM in Fig 3.2. Since F_{cl} enters only the source term there is a simple relation between the growth and the bin amplitude: we can suppress or enhance the growth by changing the clustering strength. Note, we turn on the deviation for only the bin duration and then turn it off. The response of two quantities to the binned deviation is different as seen in Fig. 3.1. The effect on the growth rate starts to wind down at the end of a bin while the deviation in growth factor is sustained, or it acts as "inertia", since the latter is an integral of $f\sigma_8$.

To constrain the deviation $c(a)$, we will use information matrix formalism (sometimes called Fisher matrix analysis refer to Appendix A). This formalism consists of multiple steps: first, we assume a certain level of error in the observable $\mathcal{O}$ (e.g., g or $f\sigma_8$) based on the experimental design, instrument sensitivity, and noise level; then we compute the theoretical sensitivity $\partial\mathcal{O}/\partial c_i$ of the observable to the deviation c_i; as a last step, we feed these two into the Fisher matrix to find out how the assumed errors propagate to the uncertainties $\sigma(c_i)$ in the deviations. In Fig. 3.3, we show the information sensitivity $\partial\mathcal{O}/\partial c_i$ for g and $f\sigma_8$. Typical galaxy surveys measure $b(a)g(a)$ instead of just the growth

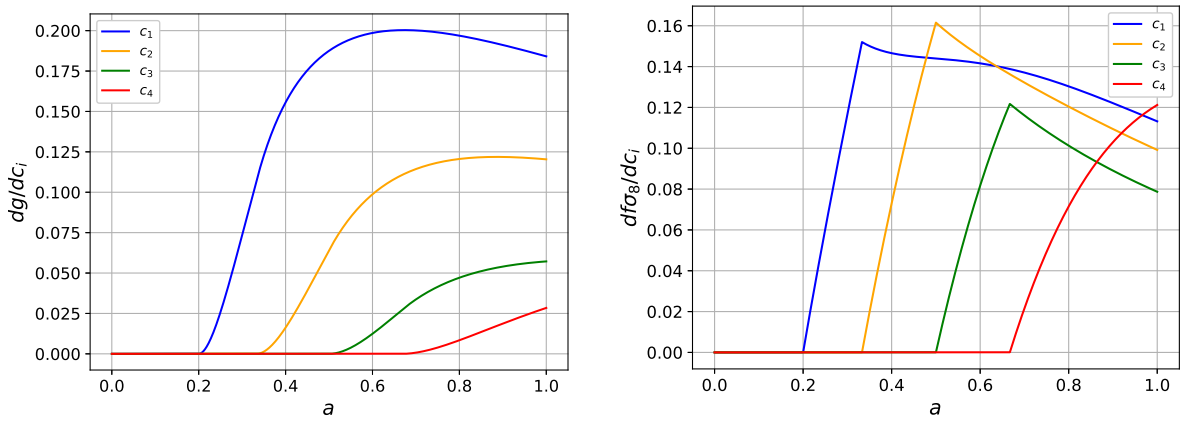

Figure 3.3: Sensitivity $\partial\mathcal{O}/\partial c_i$ curves for g and $f\sigma_8$. Curves corresponding to each clustering strength c_i show distinct shapes suggesting any covariance between them can be broken by data over a broad range of scale factor.

factor, where $b(a)$ is the scale/redshift dependent bias term. This bias arises because galaxies are overrepresented in the high density dark matter regions and underrepresented in the low density regions (making $b > 1$). However, what matters most is that there will be always degeneracy in $g(a)$ since the bias $b(a)$ is also scale dependent making it hard to disentangle the contributions of the two to the total outcome. Thus, using g in our constraints requires higher order correlation functions or data other than growth. With this in mind, we will focus on RSD factor $f\sigma_8$ alone due to its lack of bias.

Should the sensitivity curves have similar shapes, their effects on the observables would be the same making it difficult to break the covariance between them by any data. However, the situation is the opposite in our case (see Fig. 3.3) and data over a wide range of redshift can break any covariance between these parameters. Interestingly, $f\sigma_8$ sensitivity curves show linear behavior within higher redshift bins as explained in Ref. [113] (see Fig. 6). At late times, this behavior is modified and the sensitivity grows more slowly.

3.3.2 Estimated Constraints on Deviations

So far, we have computed the theoretical sensitivities of the observables to the deviations. The next step is to provide the uncertainties in the observables (in the context of information matrix analysis, they represent the uncertainties in the collected data). Prior to taking that step, we observe that the binned clustering covers a wide range of scale factor and no single cosmic survey can cover so vast a redshift range. Therefore, we consider a

combination of three different surveys. The mock data will have 2% uncertainty in the $f\sigma_8$ data from DESI[94] covering $z = 0.35, 0.45, \ldots 1.55$ denoted as "desi", plus Euclid measurements [114] at $z = 1.65, 1.75, 1.85, 1.95$ denoted by "euclid", plus peculiar velocity measurements [115–117] at $z = 0.1$ denoted by "pv". In all these cases, the lowercase names are used to highlight that we are not using the mentioned experimental results, we are simply referring to the redshift range these measurements usually focus. We have five fitting parameters: the present matter fractional density $\Omega_{m,0}$ and four binned deviations c_i with fiducial values $\Omega_{m,0} = 0.3$ and $c_i = 0$, respectively. To represent information from an additional survey, we add a Gaussian prior $\sigma_{\Omega_{m,0}} = 0.02$.

We present the results of combined effect of three data on parameter constraints in Fig. 3.4. As one can see, deviation in the highest redshift c_1 is strongly constrained by adding euclid data while the constraints of the lowest redshift bin c_4 benefits if we further add pv data. The combined measurements produce the uncertainties in the deviations as $\sigma(c_i) = (0.0282, 0.0524, 0.0888, 0.1367)$, respectively. The binned values reveal the strongest correlation to be between the second and fourth bin $r(c_2, c_4) = 0.49$.

3.4 Dark Matter Equation of State

In this section, we study the consequences of the evolving dark matter equation of state $w_{\rm dm}$. This modification will emerge in two places in the growth equation - the source term and the friction term (through Hubble parameter). We keep the clustering strength at the Newtonian gravitational coupling G_N to focus solely on the impact of $w_{\rm dm}$ modification. For consistency, we allow $w_{\rm dm}$ to change in the same four bins and set $w_{\rm dm} = 0$ only for $a < 0.2$.

Ref. [108] explored the non-standard dark matter in the context of the generalized dark matter paradigm. In this scenario, dark matter is assumed to have an evolving $w_{\rm dm}(a)$, a general sound speed $c_s(a)$, and a viscous sound speed $c_{\rm vis}$. However, Refs. [118–122] demonstrated that these sound speeds have minimal effect. Thus, we neglect $c_s(a)$ and $c_{\rm vis}$ in our analysis to focus only on the dark matter density evolution.

The relation between the energy density and the equation of state is

$$\rho_{\rm dm} = \rho_{\rm dm}(a = 1)\ e^{3\int_a^1 (da'/a')\,[1+w(a')]}\ , \tag{3.8}$$

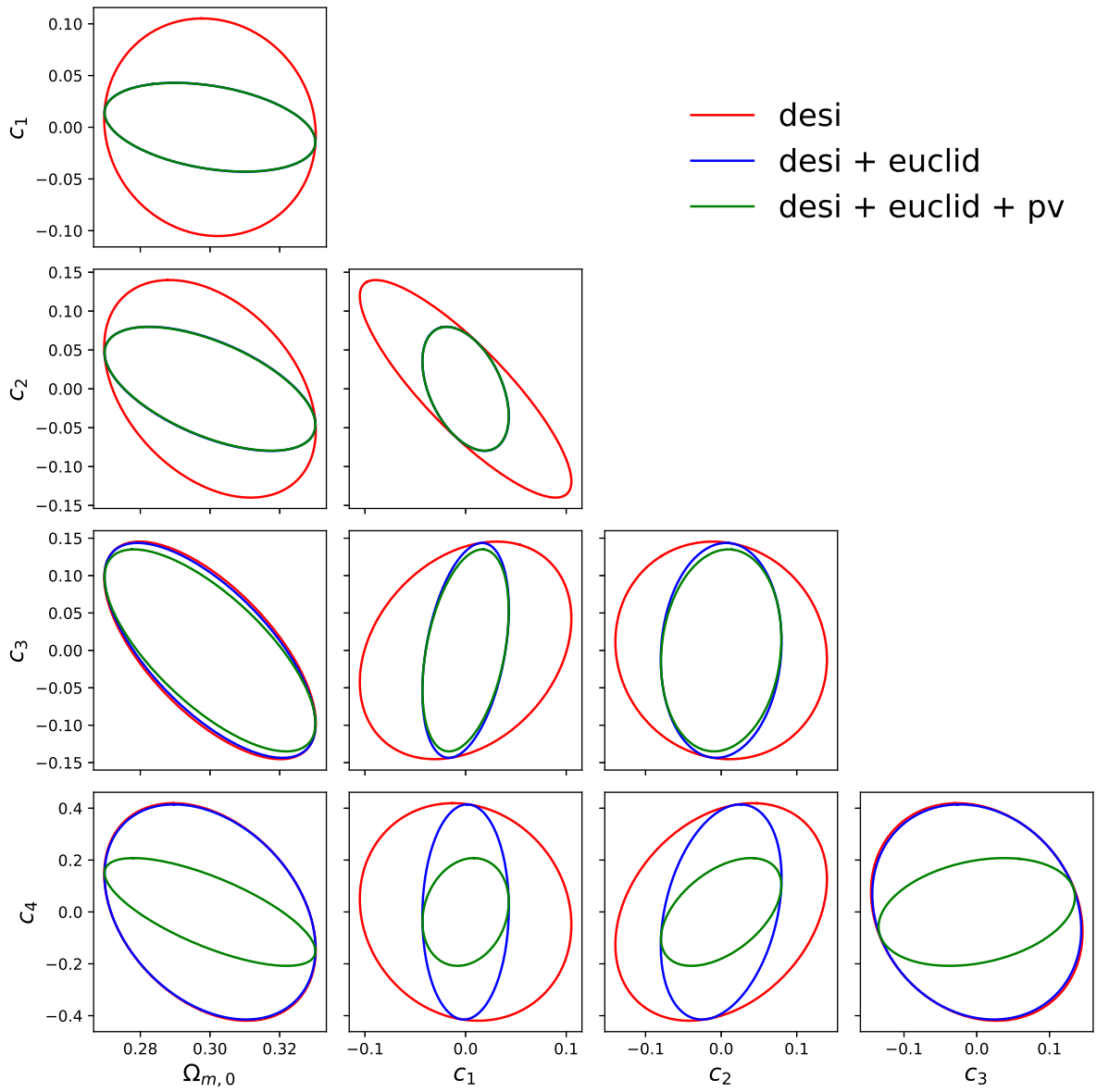

Figure 3.4: The combined effect of three measurements on the 68% joint confidence level contours for c_i and $\Omega_{m,0}$. We add a prior $\sigma_{\Omega_{m,0}} = 0.02$ in all cases.

recognizing similar pattern in Eq. 3.3, we write

$$\rho_{\rm dm}(a) = \rho_{\rm dm}^{\rm LCDM}(a=1)\, a^{-3}\, \Pi_{i=1}^{j} \left(\frac{\min[a, a_{i+1}]}{a_i} \right)^{-3w_i} \quad , \tag{3.9}$$

where we used j to indicate the four different bins in which a might be evaluated. For example, if a is evaluated within the first bin $a_1 < a < a_2$ then $j = 1$, while within the fourth bin $a_4 < a \leq 1$ then $j = 4$, with $a_5 > 1$. Preserving the high redshift universe translates to having a unit product in Eq. 3.9 for $a < a_1$, so that $\rho_{\rm dm}(a < a_1) = \rho_{\rm dm}^{\rm LCDM}(a < a_1)$. Keeping the Hubble constant H_0 fixed, we can write

$$\Omega_{\rm dm,0} = \Omega_{dm,0}^{\rm LCDM}\, a_1^{3w_1} a_2^{3(w_2-w_1)} a_3^{3(w_3-w_2)} a_4^{3(w_4-w_3)} \quad . \tag{3.10}$$

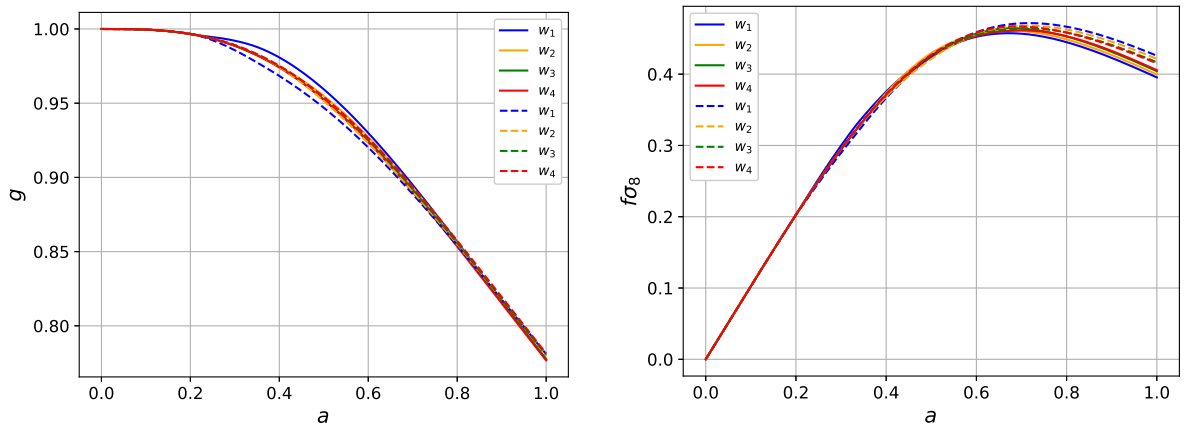

Figure 3.5: The impact of equation of state deviation on the growth factor $g(a)$ [left panel] and RSD factor $f\sigma_8(a)$ [right panel]. The amplitude of each deviation is $w_i = \pm 0.05$ corresponding to the solid and dashed curves, respectively.

The total matter consists of $\Omega_{m,0} = \Omega_{b,0} + \Omega_{\rm dm,0}$ as usual. However, $\Omega_{m,0} \neq \Omega_{m,0}^{\rm LCDM}$ since $w_i \neq 0$ and only when $w_i = 0$ we should expect standard cosmology.

The responses of g and $f\sigma_8$ to the deviations $w_i = \pm 0.05$ are plotted in Fig. 3.5. If we compute the residuals with respect to ΛCDM (see Fig. 3.6), we notice a striking difference from our first approach: all curves cross the ΛCDM curve. One important thing to notice is that we have different ΛCDM even before we turn on the first redshift bin due to $\Omega_{\rm dm,0} \neq \Omega_{dm,0}^{\Lambda\rm CDM}$ from Eq. 3.10. Additionally, dimensionless Hubble parameter is also modified since Eqs. 3.9 and 3.10 give

$$H^2(a < a_1)/H_0^2 = \Omega_{m,0}^{\rm LCDM} a^{-3} + 1 - \Omega_{b,0} - \Omega_{\rm dm,0} \ , \tag{3.11}$$

before the first bin turns on. Only when we have all the deviations set to zero $w_i = 0$, then we expect $\Omega_{\rm dm,0}$ and $H^2(a < a_1)$ restore to their ΛCDM values.

We notice the three-stage impact of deviations in the structure growth to understand the crossing behavior in Fig. 3.5. The Hubble parameter acts as a friction in the evolution equation, therefore, growth is affected by a small amount even before the first bin since $H^2(a < a_1)$ is offset from the fiducial ΛCDM by a^3 (refer to Eq. 3.11). This is similar to Eq. (7) in Ref. [123] where it was shown that both the growth rate f and the growth factor g deviate from their fiducial values by an amount of a^3. The suppression of growth is due to $\Omega_{\rm dm,0}$ as it decreases with increasing w_i (for positive w_i). This corresponds to the first pre-bin stage as it is shown more clearly in the fractional deviations in Fig. 3.6. The second stage occurs within bin as w_i deviates from zero. Any deviation directly affects the friction term in the evolution equation through $d\ln H^2/d\ln a = -3(1 + w_{\rm tot})$ with non-

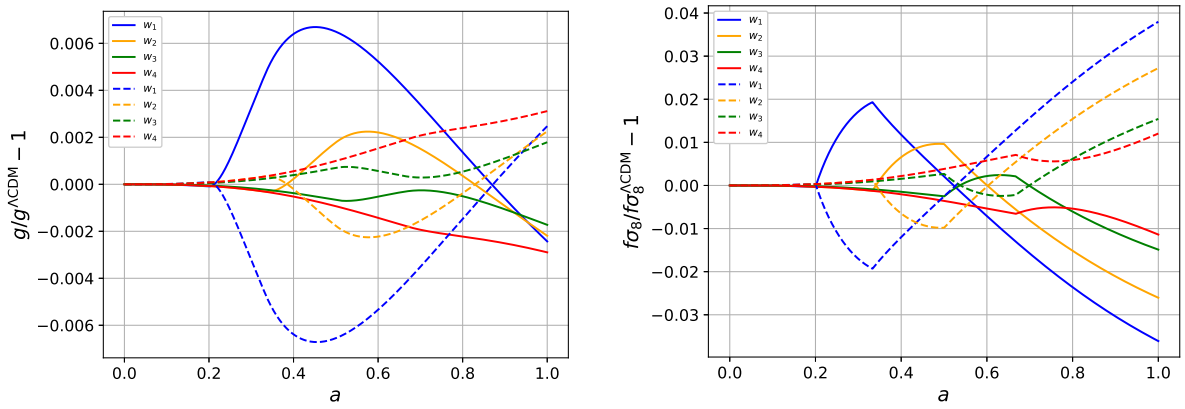

Figure 3.6: The same as in Fig. 3.5, but shown as fractional deviation form ΛCDM values.

zero w_i. The suppression/enhancement of this friction term leads to enhanced/suppressed growth for positive/negative w_i. The final stage takes place after a bin is turned off. Here, again the reduced $\Omega_{\mathrm{dm},0}$ suppresses growth but this time less effectively than it did before the first bin.

We can see the imprints of these three physical behaviors in the sensitivity plots in Fig. 3.7. Similar to the clustering deviation case, we see an inertial effect in the growth factor where it continues an upward trend even though the bin is turned off. Eventually, the reduced $\Omega_{\mathrm{dm},0}$ takes over to suppress the growth for the rest of its history. The fitting parameters are the present ΛCDM fractional matter density $\Omega_{m,0}^{\mathrm{LCDM}}$ and the four equation of state deviations w_i with fiducial values $\Omega_{m,0}^{\mathrm{LCDM}} = 0.3$ and $w_i = 0$, respectively. This time we expect more covariance since all these parameters appear in $\Omega_{\mathrm{dm},0}$ given by Eq. 3.10.

Implementing the same data combination, we obtained the 68% joint confidence contours for the parameter constraints in Fig. 3.8. Finally, when using the prior in $\Omega_{m,0}^{\mathrm{LCDM}}$,

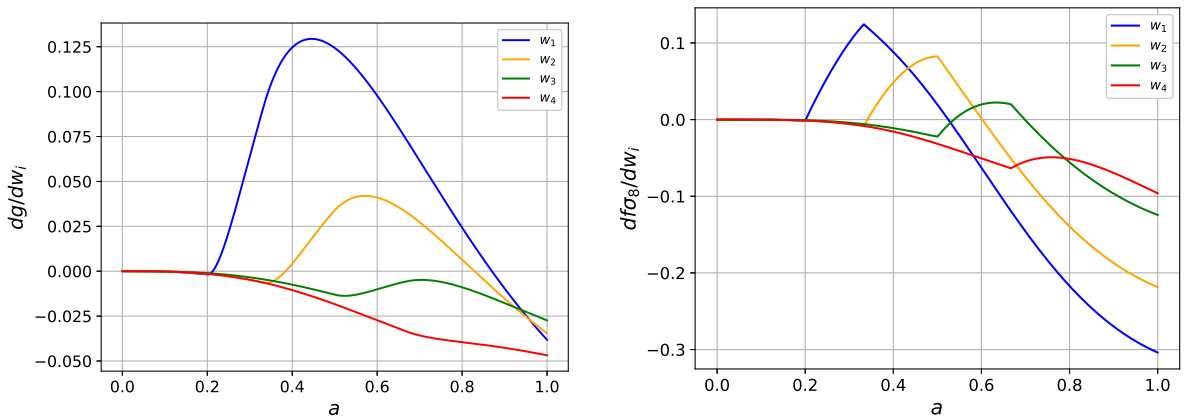

Figure 3.7: Sensitivity $\partial\mathcal{O}/\partial w_i$ curves for g and $f\sigma_8$. Right panel shows less sensitivity in $f\sigma_8$ to the low-redshift bin deviations.

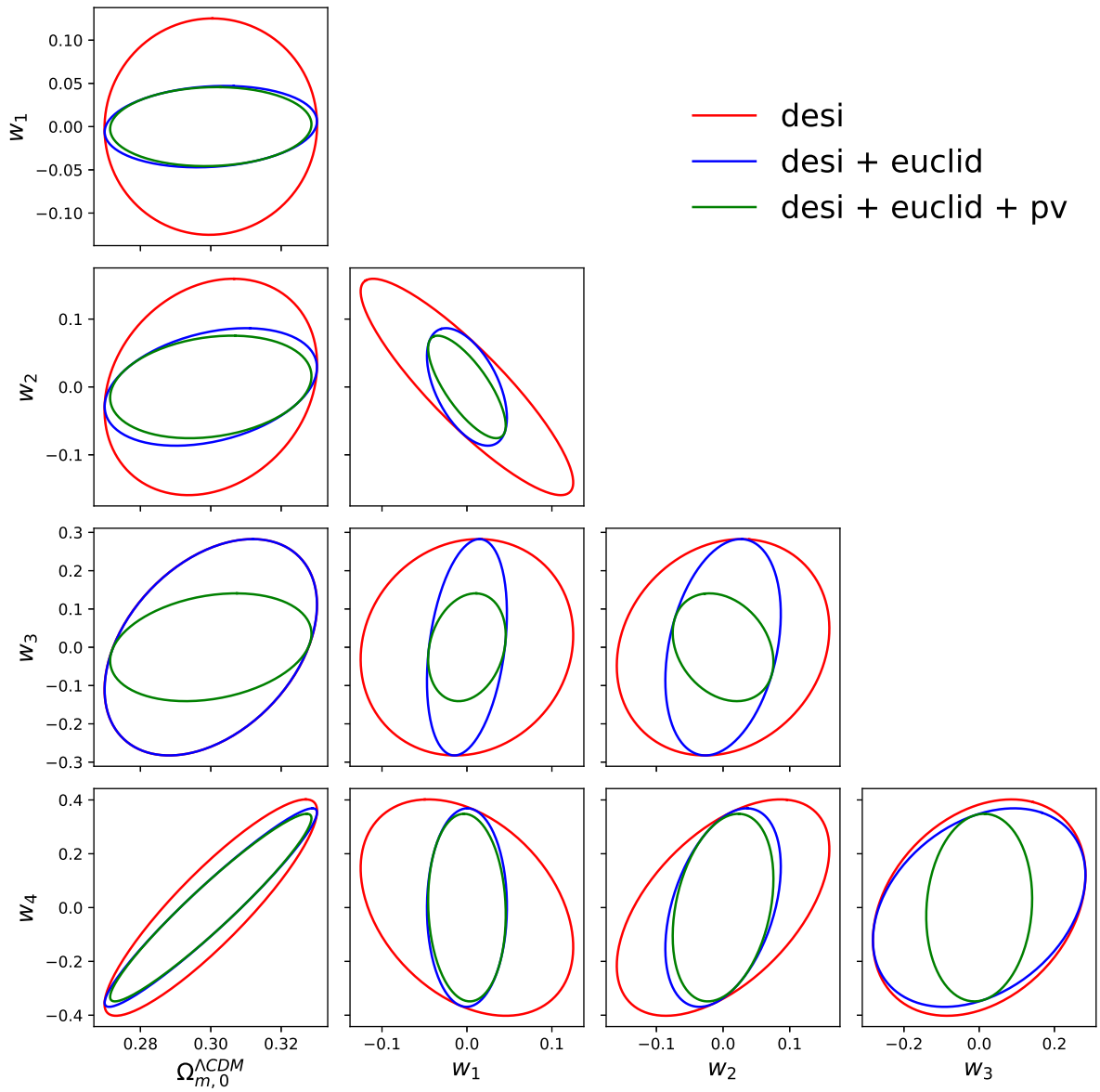

Figure 3.8: 68% joint confidence level contours on the dark matter equation of state parameters and matter fractional density for various data combinations. All cases have a prior $\sigma_{\Omega_{m,0}} = 0.02$.

the deviations in the parameters are $\sigma(w_i) = (0.0300, 0.0497, 0.0926, 0.2293)$, respectively. Although the bins are mostly independent, this time the strongest correlation $r(w_1, w_2) = -0.75$ shows slightly higher value compared to our first approach with $r(c_2, c_4) = 0.49$.

Under normal circumstances, adding pv data, corresponding to low-redshift, should not add a constraint on the first w_1 and second w_2 bins since they are turned on at high redshift. However, the outlined three physical phases, with the help of $\Omega_{\rm dm,0}$, enable the propagation of late-time data constraints to the early time. This back-and-forth propagation of data constraints is further seen through the effect of euclid data (high

redshift) on the w_3 and w_4 constraints (low redshift), albeit modestly. The situation was completely different if we look at Fig. 3.4. Also, the impact of pv on w_4 is especially weak due to several factors: the covariance between w_4 and $\Omega_{\rm dm,0}$ is high, with correlation $r(w_4, \Omega_{\rm dm,0}) = 0.95$, and the $f\sigma_8$ sensitivity to w_4 is small at low redshift (see Figure 3.7), making it difficult to break the degeneracy and constrain the deviation with low redshift data. While adding high redshift measurements predictably improves the constraints on high redshift bins w_1 and w_2, pv data seems to help with the w_3 bin.

3.5 Conclusions

With the advancement of precision guided cosmology, the evidence for dark matter's existence became ever more convincing. However, we have little knowledge about its fundamental properties expect for its energy density. Exploring the dark matter nature became the most exciting research field in cosmology with a plethora of proposed models. In this study, we investigated its two characteristics – clustering strength and equation of state both necessary for structure growth. We employed a model-independent approach by binning deviations in redshift within the two properties.

Cosmic structure growth has been an excellent probe to constrain dark matter properties. We first study if dark matter clusters with the standard gravitational strength. RSD measurements with 2% accuracy similar to DESI, Euclid, and low redshift peculiar velocity experiments put $\sigma(c_i) \approx 0.03 - 0.14$ level constraints on the clustering deviation.

Our second investigation concerns how much dark matter deviates from the pressureless baryons, i.e. $\rho_{\rm dm} \propto a^{-3}$. It is essentially an investigation of the equating of state of dark matter. Employing the same four bins and data combinations, we found the constraints to be at the $\sigma(w_i) = 0.03 - 0.23$ level. We showed that the modification in w carries rich possibilities to a modification in the background cosmological model.

Unlike other works, we didn't adopt any functional forms for the deviation behavior which would have resulted in even tighter constraints. We prefer model-independent approach given the uncertainties in the dark matter properties. We expect to obtain improvements in the constraints with future surveys that will span even higher redshifts, such as MegaMapper [124] or Spec-S5 [125]. The consequences of general sound speed and viscous sound speed associated with non-zero equation of state are left for future work.

Chapter 4

Running gravitational constant induced dark energy as a solution to σ_8 tension

4.1 Introduction

Over the last three decades, cosmology became quantatitive with increasing measurement accuracy. The cosmic acceleration, discovered in the final years of last century pointed towards the existence of dark energy Λ in addition to cold dark matter (CDM)[21]. Thus, ΛCDM became a standard model with an excellent description of structure evolution starting from the initial density seeds observed in the CMB to the present large scale structure (LSS) [46, 126–128]. The parameters of this model have been measured with remarkable accuracy by various cosmic surveys. The Planck's results released in 2018 provided precise estimates of the standard model parameter values which were used to define Planck18/ΛCDM model[46]. Despite its success, significant challenges remain mostly with the unknown constituents such as the cosmological constant Λ and CDM. There is also an ad-hoc period of rapid expansion in the early universe to explain the almost scale-invariant initial conditions [25, 26, 129].

Aggravating the issue further, recent cosmic surveys brought to light inconsistencies with the estimates of Planck18/ΛCDM. These include tensions between the predicted and observed values of the present Hubble parameter and σ_8 parameter corresponding to the amplitude of mass fluctuations on scale of $8h^{-1}$ Mpc. Both tensions occur at late times $z \lesssim 0.6$ with a third discrepancy following suit – increased value of Ω_m favored by low redshift measurements. These findings exert considerable pressure on the Planck18/ΛCDM model.

Even though tensions might occur due to a systematic bias in the data analysis, their persistence after almost a decade of data processing hints toward new physics [130].

The parameter σ_8 is estimated by several cosmic observations such as, weak lensing by the CFHTLenS collaboration [131], and the Redshift Space Distortion (RSD) measurements [132–134]. As shown in Ref. [135, 136], these measurements are in tension with the values of $\Omega_{m,0}$ and σ_8 from the Planck mission. There are many attempts to reconcile this tension through dark energy-dark matter interaction [137–142], a hot dark matter [143], and modified gravity models [144–146]. However, one should expect that a proposal for resolving one tension would not aggravate the other. This brings the central focus on less intrusive and more simple modifications to the standard model.

The present work aims to address the σ_8 tension through investigating the structure growth implications of simple modification to GR whose effects can be captured by a single scalar function of the energy density $\xi(\rho)$. This modification was first introduced to resolve the singularity issue of GR [147] and we will call it the Markov-Mukhanov model or simply the MM model. We consider a physically motivated parametrization for running gravitational constant G and obtain all the other quantities through MM prescription. From a numerical perspective, we fit the model parameters to the RSD datasets and show that MM model can alleviate σ_8 tension thereby providing insight into Newton's constant.

This work contains two major sections – theoretical and numerical. Section 4.2 outlines the MM action with the background equations and the perturbation equation, followed by the introduction of the $G(a)$ parametrization. Section 4.3 presents the numerical results. We conclude in Section 4.4. Throughout, we follow the units $c = \hbar = 1$.

4.2 Theory

4.2.1 Markov-Mukhanov Action

We study the simplest modification to GR – non-minimal coupling between matter and gravity defined by a function $\xi(\rho)$ where $\rho = T^{\mu\nu}u_\mu u_\nu$ is the proper density of the background fluid. This modification, while equivalent to ΛCDM in a specific limit, has a predictive power that goes beyond the standard model without assuming the existence of

any hypothetical field. As proposed in [147], the total action is

$$\mathcal{S} = \int \left(\frac{R}{8\pi G_0} + 2\xi(\rho)\mathcal{L}_m \right) \sqrt{-g} d^4x \ , \tag{4.1}$$

where G_0 is the usual Newton's constant and $\mathcal{L}_m = \rho$ corresponds to matter Lagrangian. Assuming a homogeneous and isotropic universe, we use the flat Robertson-Walker (RW) metric with the space-like signature $(+---)$ throughout this chapter. In the limit $\xi \to 1$, the theory reduces to GR without dark energy while retaining $\xi = 1 + \frac{\text{const}}{\rho}$ fully restores ΛCDM.

We vary the action $\mathcal{S}$ with respect to the metric $g_{\mu\nu}$ to obtain the equation of motion that links the geometric structure with the matter content,

$$G^\nu_\mu \equiv R^\nu_\mu - \frac{1}{2}\delta^\nu_\mu R = 8\pi G(\rho) T^\nu_\mu + \Lambda(\rho)\delta^\nu_\mu \ . \tag{4.2}$$

The equation contains a time-varying gravitational constant G and a Λ-like term on the right-hand side of the modified Einstein's equation. The energy-momentum tensor T^ν_μ for the perfect fluid is

$$T^\nu_\mu = (\rho + P) u_\mu u^\nu - P\delta^\nu_\mu, \tag{4.3}$$

here we denote P as the fluid pressure and u_μ as its four-velocity.

It could be misinterpreted that $G(\rho)$ and $\Lambda(\rho)$ are independent quantities, however, they are connected through the gravity-matter coupling $\xi(\rho)$ as

$$G(\rho) = G_0 \left(\rho \frac{d\xi}{d\rho} + \xi \right), \quad \Lambda(\rho) = -8\pi G_0 \rho^2 \frac{d\xi}{d\rho} \ . \tag{4.4}$$

If we consider the Newtonian limit $G \to G_0$, the general solution of Eq. 4.4 for $\xi(\rho)$ reproduces ΛCDM cosmology with

$$\xi_{\Lambda CDM} = \left(1 + \frac{\lambda_0}{\rho} \right) \ , \tag{4.5}$$

where λ_0 is a constant and with the combination $\Lambda = 8\pi G_0 \lambda_0 = \Lambda_0$, we recognize the cosmological constant.

Employing RW metric, we can find the MM version of the Friedmann equations as

$$\begin{aligned} H^2 &= \frac{8\pi G(\rho)}{3}\rho + \frac{1}{3}\Lambda(\rho) = \frac{8\pi G_0}{3}\xi\rho \ , \\ \frac{\ddot{a}}{a} &= -\frac{4\pi G_0}{3}\left[(\rho + 3P)\xi + 3\rho\frac{d\xi}{d\rho}(\rho + P) \right] \ . \end{aligned} \tag{4.6}$$

The time span of our analysis starts from the matter-dominated epoch, then keeping only the pressureless dust is a good approximation. However, regardless of the background

fluid, there is an underlying symmetry of MM model which keeps the conservation of energy-momentum tensor for the matter component intact (see the r.h.s. of Eq. 4.2)

$$\nabla_\nu \left(8\pi G(\rho) T^\nu_\mu + \Lambda(\rho)\delta^\nu_\mu \right) = 0. \tag{4.7}$$

In other words, the combination of $G(\rho)$ and $\Lambda(\rho)$ under covariant derivative cancels the mutual effects as

$$8\pi T^\nu_\mu \nabla_\nu G(\rho) + \delta^\nu_\mu \nabla_\nu \Lambda(\rho) = 0, \tag{4.8}$$

to give

$$G(\rho)\nabla_\nu T^\nu_\mu = 0. \tag{4.9}$$

For $\mu = 0$, we recognize it as the continuity equation for the background fluid [148]. Solving $\nabla_\nu T^\nu_0 = 0$ for $\rho(a)$ gives

$$\rho = \rho_{\rm m} = \Omega_m \rho_0 a^{-3}, \tag{4.10}$$

with $\rho_{\rm m}$, Ω_m, and ρ_0 as the matter-energy density, present matter fractional density, and present total density of the universe, respectively.

All the necessary background quantities are well-defined once we determine the functional form for any one of ξ, G, and Λ terms. We favor G out of the three choices, because we have more knowledge about the gravitational constant making it easier to parameterize, a fit we take advantage of in the ensuing sections. Hence, we will refer to (4.1) as GCDM hereafter given that it can effectively replace the cosmological constant.

As detailed in Appendix B, one could map the effects of varying $G(\rho)$ into a perfect fluid form. It provides easier incorporation of GCDM parameters into the CAMB or CLASS codes for early universe investigations. However, at this stage we want to keep the physical meanings of time varying G intact to better understand its unique imprint in the structure growth.

4.2.2 Density Perturbations

Growth of structure characterized by δ is a powerful probe to distinguish GR from modified gravity models [149]. We now employ density perturbation analysis to derive an evolution equation for $\delta \equiv \delta\rho/\rho$ in the MM prescription. To estimate the density perturbations within flat RW spacetime, we implement the conformal Newtonian gauge with two scalar metric perturbations Ψ and Φ. In linear order, we expect $\delta \ll 1$ and it is practical to

discriminate background (denoted with overbar) quantities from perturbations by writing $X = \bar{X} + \delta X$. Then, the perturbed metric becomes

$$g^{\nu\mu} = \bar{g}^{\nu\mu} + \delta g^{\nu\mu} = \frac{1}{a^2} \begin{pmatrix} 1 - 2\Psi & 0 \\ 0 & -(1 + 2\Phi)\delta^{ij} \end{pmatrix} , \tag{4.11}$$

while Eq. 4.2 can be written as

$$G^{\nu}_{\mu} = \bar{G}^{\nu}_{\mu} + \delta G^{\nu}_{\mu} , \quad T^{\nu}_{\mu} = \bar{T}^{\nu}_{\mu} + \delta T^{\nu}_{\mu} , \quad G = \bar{G} + \delta G , \quad \Lambda = \bar{\Lambda} + \delta\Lambda . \tag{4.12}$$

Substituting these quantities into the field equation while keeping only the zeroth and first-order terms gives

$$\bar{G}^{\nu}_{\mu} + \delta G^{\nu}_{\mu} = 8\pi\bar{G}\bar{T}^{\nu}_{\mu} + \bar{\Lambda}\delta^{\nu}_{\mu} + 8\pi\bar{G}\delta T^{\nu}_{\mu} + 8\pi\delta G\bar{T}^{\nu}_{\mu} + \delta\Lambda\delta^{\nu}_{\mu} . \tag{4.13}$$

Since the field equation links two separate concepts, geometry and matter content, it is wise to consider LHS and RHS of Eq. 4.13 separately. Starting in the matter domination era (negligible radiation), we still expect the energy-momentum tensor to be isotropic. We further note that the perturbed G and Λ do not trigger additional anisotropic stresses as seen in Eq. 4.13. Thus, neglecting this effect, we set $\Phi = \Psi$.

The LHS of Eq. 4.13 can be written as [37]

$$G_{00} = 3\mathcal{H}^2 + 2\nabla^2\Phi - 6\mathcal{H}\Phi' , \tag{4.14}$$

$$G_{0i} = 2\partial_i \left(\Phi' + \mathcal{H}\Phi\right) , \tag{4.15}$$

$$G_{ij} = -\left(2\mathcal{H}' + \mathcal{H}^2\right)\delta_{ij} + \left[2\Phi'' + 4\left(2\mathcal{H}' + \mathcal{H}^2\right)\Phi + 6\mathcal{H}\Phi'\right]\delta_{ij} , \tag{4.16}$$

where the prime denotes conformal time derivative while the calligraphic characters such as, $\mathcal{H} = a'/a$, refer to their values in conformal coordinate system. In subhorizon scales $k \gg \mathcal{H}$, velocity perturbation is subdominant leading to $\Phi' + \mathcal{H}\Phi \approx 0$ in Eq. 4.15. Thus, focusing only on Eqs. 4.14 and 4.16, we raise the indices and keep the first-order terms to obtain

$$G^0_0 = a^{-2}\Big(3\mathcal{H}^2 + 2\nabla^2\Phi - 6\mathcal{H}(\Phi' + \mathcal{H}\Phi)\Big) = a^{-2}\Big(3\mathcal{H}^2 + 2\nabla^2\Phi\Big) , \tag{4.17}$$

$$G^i_i = -3a^{-2}\left[-\left(2\mathcal{H}' + \mathcal{H}^2\right) + 2\left(\Phi'' + 3\mathcal{H}\Phi' + \left(2\mathcal{H}' + \mathcal{H}^2\right)\Phi\right)\right] . \tag{4.18}$$

Next, we move to the RHS of Eq. 4.13 and write the first-order terms of the matter perturbation as

$$\delta T^0_0 = \delta\rho_{\rm m} \ , \tag{4.19}$$

$$\delta T^i_i = -3\delta P_{\rm m} \approx 0 \ , \tag{4.20}$$

while perturbations in G and Λ are

$$\bar{T}^0_0\delta G + \delta\Lambda\delta^0_0 = 0 \ , \tag{4.21}$$

$$\bar{T}^i_j\delta G + \delta\Lambda\delta^i_j = \delta\Lambda\delta^i_j \ . \tag{4.22}$$

where $\delta\Lambda = (d\Lambda/d\bar{\rho}_{\rm m})\delta\rho_{\rm m}$ and $\delta G = (dG/d\bar{\rho}_{\rm m})\delta\rho_{\rm m}$. Eq. 4.21 follows as a special case of Eq. 4.8.

After finding the perturbed quantities in the Einstein and total energy-momentum tensors, we can equate both sides to obtain

$$\nabla^2\Phi = 4\pi\bar{G}a^2\bar{\rho}_{\rm m}\delta \ , \tag{4.23}$$

$$\Phi'' + 3\mathcal{H}\Phi' + \left(2\mathcal{H}' + \mathcal{H}^2\right)\Phi = \Phi'' + 2(\mathcal{H}\Phi)' = -\frac{1}{2}a^2\delta\Lambda \ , \tag{4.24}$$

up to a first order. Zeroth order terms are just Friedmann's first and second equations given in Eq. B.7.

In the rest of this work, we omit the overbar representing the background quantities. Since different modes decouple and evolve independently in Fourier space, we find the Fourier transforms of the above perturbed equations together with the Laplacian operator $\nabla^2 \to -k^2$ where k is the comoving wavenumber. We take conformal time derivative of Eq. 4.23 and substitute into Eq. 4.24 to find

$$\delta_k'' + \mathcal{H}\delta_k' + \left(\mathcal{H}' - \mathcal{H}^2\right)\delta_k = -2\frac{G'}{G}\delta_k' - \left[\left(1 - \frac{k^2}{3\mathcal{H}^2}\right)\mathcal{H}\frac{G'}{G} + \frac{G''}{G}\right]\delta_k \ . \tag{4.25}$$

On the LHS, we recognize the perturbation equation within the Friedmann-Robertson-Walker model while on the RHS, we see the correction terms resulting from GCDM (4.1) that features a scale-dependent term. We consider scales inside the Hubble radius $k >> \mathcal{H}$, expect minimal deviation from Newtonian gravitational constant $|G'/G_0| \ll 1$ (see Eq. 4.4). While the stability of the gravitational field requires $|G''/G_0| \ll 1$ ensuring minimal perturbative G effect on the structure growth. Thus, on the RHS, all the terms

are subdominant compared to the term involving scale-dependence. Then, the equation simplifies to

$$\delta_k'' + \mathcal{H}\delta_k' + \left[\mathcal{H}' - \mathcal{H}^2 - \frac{k^2}{3\mathcal{H}}\frac{G'}{G}\right]\delta_k = 0\ . \tag{4.26}$$

Next, we convert the derivatives from conformal time into scale factor a and use the second Friedmann equation to arrive at the final form for the main equation of our analysis,

$$a^2\frac{d^2\delta_k}{da^2} + \left(3 + \frac{d\ln H}{d\ln a}\right)a\frac{d\delta_k}{da} - \left(\frac{3}{2}\frac{G}{G_0}\frac{H_0^2\Omega_{\rm m}}{a^3H^2} + \frac{1}{3}\frac{k^2}{a^2H^2}\frac{d\ln G}{d\ln a}\right)\delta_k = 0\ . \tag{4.27}$$

Hence, the modifications from GCDM influence the cosmic structure growth in two different ways: directly impacting the source term by suppressing/enhancing the growth depending on the negative/positive slope $\frac{dG}{da}$, and indirectly affecting the growth through H in the modified Friedmann equations (see Eq. B.7).

4.2.3 Parameterizing $G(\rho)$

We shall now proceed to propose a parametrization for G to trace the deviation from GR at low redshift universe. We assume there was a matter-dominated epoch during the cosmic evolution which is a safe practice since there is no deviation in the dust evolution $\rho_{\rm m} \sim a^{-3}$ from the standard model. Under this assumption Eq. 4.4 becomes

$$G = G_0\left(-\frac{a}{3}\frac{d\xi}{da} + \xi\right). \tag{4.28}$$

From Eq. B.5, we observe $\xi \approx 1$ during matter domination. Likewise, we can establish a parallel line of thought by observing that there is little room for deviation from ΛCDM at early times and Eq. 4.5 suggests $\xi \to 1$ for $a \to 0$. Then we have $G \simeq G_0$ and $dG/da \simeq 0$ at $a \ll 1$ while we should recover $G \simeq G_0$ at present, i.e. at $a = 1$. These considerations substantially restrict the possible parametrization for $G(a)$. Additionally, we have $dG/da|_{(a=1)} \approx 0.001$ from the lunar laser experiments [150]. Meanwhile, the range of $G = 1.09 \pm 0.2$ is required by Big Bang Nucleosynthesis (BBN) [151]. Taking all these key elements into account, we propose the following parametrization

$$G/G_0 = 1 + ga^n(1-a)^{2m}, \tag{4.29}$$

where g is the only free parameter, n and m are natural numbers. Integrating Eq. 4.28 with $g = 0$ restores ΛCDM limit of Eq. 4.5. In the $g \neq 0$ case, we choose certain values for m and n then try to search g by fitting the parametrization to the data. We reiterate

the process until finding the solution to the σ_8 tension. Regarding the exponents, n and m control the early and late time behavior of G, respectively. However, the overall effect should be very small otherwise the last term in Eq. 4.27 will overwhelm the source. Supposing $\frac{k}{aH}|_{a=1} = \frac{H_0^{-1}}{\lambda} \approx \frac{4000}{10} = 400$, we see the scale dependent part involves a large number $\sim 10^5$. To have a meaningful contribution in the source term, we have to counterbalance it by expecting $\frac{d\ln G}{d\ln a} \sim 10^{-5}$ which translates to having large numbers for either n or m. We will take this point into account when choosing specific values of n and m.

In the ensuing section, we implement the Redshift Space Distortion (RSD) factor $f\sigma_8$ to explore the model implications on the σ_8 tension.

4.3 Numerical Analysis

4.3.1 Method

The galaxy redshift surveys provide insight into the clustering evolution, characterized not only by δ but by the growth rate f, over a redshift range $z \in (0.02, 1.4)$. The growth rate is related to the density perturbation as

$$f(a) = \frac{d\ln\delta_k(a)}{d\ln a}. \tag{4.30}$$

However, RSD measurements commonly use the combination $f\sigma_8$ for its lack of bias [152]. Here, σ_8 stands to show the root mean square of matter power spectrum over the scale ~ 10 Mpc. By solving Eq. 4.27, we can construct,

$$f\sigma_8 = \sigma_8 \frac{d\ln\delta_k}{d\ln a}. \tag{4.31}$$

Carefully collected RSD measurement data for $f\sigma_8(z)$ is presented in Table 4.1. We aim to test our model's prediction against this data using Bayesian analysis and by minimizing

$$\chi^2 = VC^{-1}V^T\ , \tag{4.32}$$

for the fitting parameters g and σ_8. Here, C^{-1} stands for the inverse covariance matrix corresponding to the data in the Table and V is the raw vector, i-th column of which is given by

$$V_i = f\sigma_8(z_i) - \text{ratio}(z_i) f\sigma_8(z_i, g, \sigma_8)\ , \quad i = 1, \ldots, N. \tag{4.33}$$

Table 4.1: A summary of dataset containing independent $f\sigma_8(z)$ measurements from different surveys compiled by [144]

Index	Dataset	z	$f\sigma_8(z)$	Refs.	Fiducial $\Omega_{\rm m}$
1	6dFGS+SnIa	0.02	0.428 ± 0.0465	[153]	0.3
2	SnIa+IRAS	0.02	0.398 ± 0.065	[154, 155]	0.3
3	2MASS	0.02	0.314 ± 0.048	[155, 156]	0.266
4	SDSS-veloc	0.1	0.37 ± 0.130	[157]	0.3
5	SDSS-MGS	0.15	0.490 ± 0.145	[158]	0.31
6	2dFGRS	0.17	0.510 ± 0.060	[152]	0.3
7	GAMA	0.18	0.360 ± 0.090	[159]	0.27
8	GAMA	0.38	0.440 ± 0.060	[159]	0.27
9	SDSS-LRG-200	0.25	0.3512 ± 0.0583	[160]	0.25
10	SDSS-LRG-200	0.37	0.4602 ± 0.0378	[160]	0.25
11	BOSS-LOWZ	0.32	0.384 ± 0.095	[161]	0.274
12	SDSS-CMASS	0.59	0.488 ± 0.060	[162]	0.307115
13	WiggleZ	0.44	0.413 ± 0.080	[163]	0.27
14	WiggleZ	0.6	0.390 ± 0.063	[163]	0.27
15	WiggleZ	0.73	0.437 ± 0.072	[163]	0.27
16	Vipers PDR-2	0.6	0.550 ± 0.120	[164]	0.3
17	Vipers PDR-2	0.86	0.400 ± 0.110	[164]	0.3
18	FastSound	1.4	0.482 ± 0.116	[165]	0.27

The terms in the expression are: i-th value of the data $f\sigma_8(z_i)$ and the model prediction $f\sigma_8(z_i, g, \sigma_8)$ with N designating the total number of measurements. We specifically focus on ratio(z_i), given its importance to include the model dependence of the data. For example, we can see different fiducial cosmologies used when extracting the $f\sigma_8$ data in Table 4.1. To account for this model dependence, the following ratio is shown to be an excellent approximation [166]

$$\text{ratio}(z) = \frac{H(z)d_A(z)}{H^{fid}(z)d_A^{fid}(z)} \ . \tag{4.34}$$

We have the model-specific Hubble parameter $H(z)$ and the angular diameter distance $d_A(z)$ in the numerator while similar parameters of the fiducial cosmology were represented in the denominator.

In Ref. [163], no correlation is assumed for all data, except for WiggleZ for which

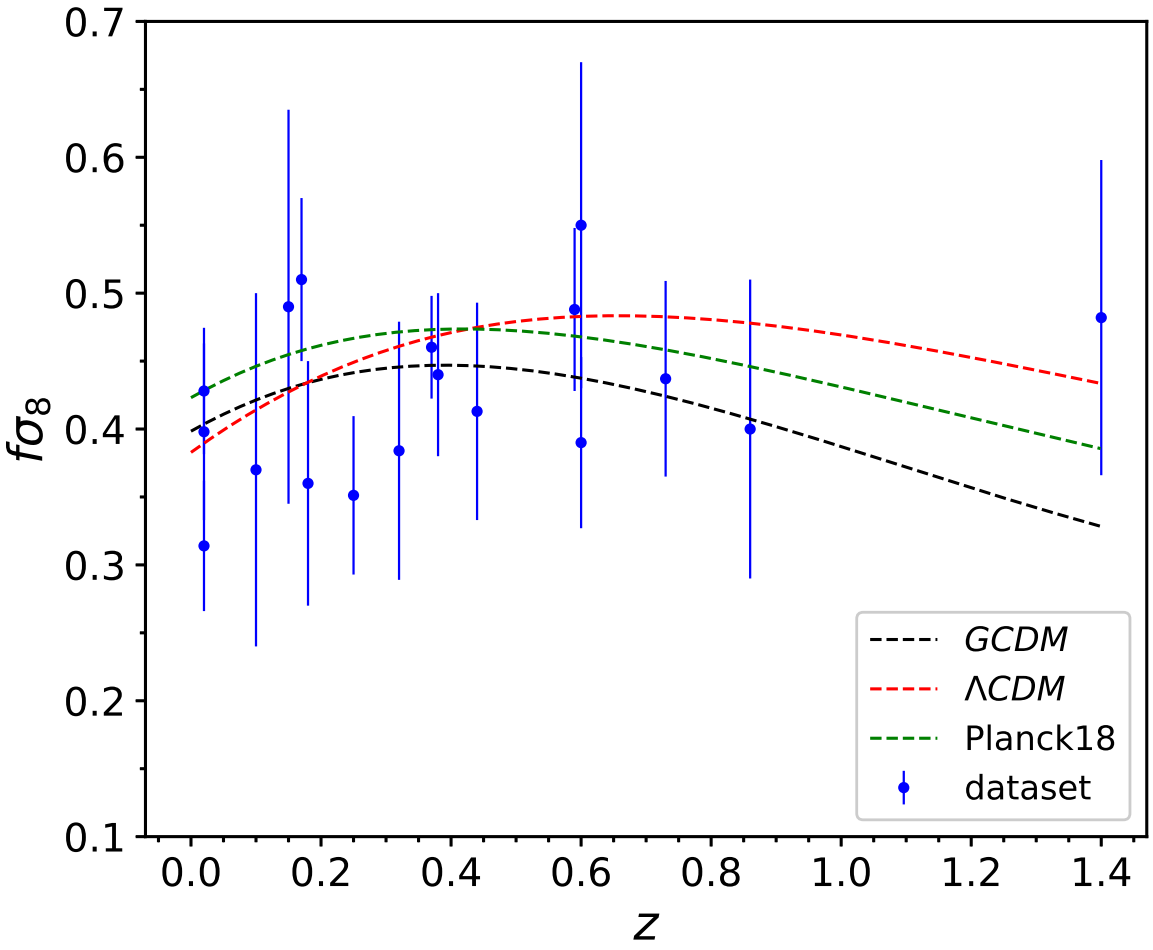

Figure 4.1: The error bars in the dataset of Table 4.1 are represented by vertical lines. The green and red dashed lines correspond to the best fits of Planck18 and ΛCDM models, respectively. While the black dashed line is the GCDM result obtained by $G(a)$ parameterization with the best fit $g = 0.24$ corresponding to $n = 3, m = 10$.

the covariance matrix is given by

$$C^{\text{WiggleZ}} = 10^{-3} \begin{pmatrix} 6.400 & 2.570 & 0.000 \\ 2.570 & 3.969 & 2.540 \\ 0.000 & 2.540 & 5.184 \end{pmatrix} . \tag{4.35}$$

Hence, at the position of the WiggleZ data, we will have 3×3 submatrix C^{WiggleZ} inside the $N \times N$ covariance matrix.

In evaluating the best fit values for σ_8 and g, we used open-source sampler `emcee` [167] and `GetDist` [168] libraries. GitHub[1] repository contains our Python implementation.

[1] https://github.com/Tilek-Zhumabek/GCDM

4.3.2 Results

This section provides the results of testing GCDM against RSD data. We fitted the model predictions $f\sigma_8$ to the observations to find the best fit values of g and σ_8. At first glance, it might look problematic to use the scale independent RSD data to justify a model which contains scale dependence in growth. To remind the reader, the cosmological measurements (including $f\sigma_8$) are effectively averaged over a range of scales and, in our case, using a certain value for k as a representative scale makes the model's predictions comparable to the observation. Thus, when solving Eq. 4.27 the scale is fixed to $k = 300H_0 \sim 0.1h$ Mpc^{-1} and this choice is motivated by several reasons. First, the tension between the ΛCDM predictions and the Planck18/ΛCDM best fit parameters occur during large scale structure formation which is a relatively late time phenomena (roughly between $0 < z < 1$). Therefore, we are interested in the large scales. However, our measurement accuracy is limited for $k < 0.01h$ Mpc^{-1} while scales smaller than $k > 0.2h$ Mpc^{-1} have already transitioned to their nonlinear regimes making $k = 0.1h$ Mpc^{-1} a reasonable choice [169, 170].

Fig. 4.1 displays the result of fitting the ΛCDM and GCDM models to the RSD factor measurements in Table 4.1. GCDM with G parameterization ($n = 3, m = 10$) yields the best fit values of $g = 0.24^{+0.089}_{-0.097}, \Omega_{\rm m} = 0.28^{+0.092}_{-0.073}, \sigma_8 = 0.87^{+0.20}_{-0.19}, \chi^2 = 14.2$ (dashed-black curve), while Planck18/ΛCDM model gives $\Omega_{\rm m} = 0.31^{+0.0074}_{-0.0074}, \sigma_8 = 0.81^{+0.0061}_{-0.0061}, \chi^2 = 17.6$ (dashed-green curve), lastly, ΛCDM model presents the best fit parameter values as $\Omega_{\rm m} = 0.22^{+0.12}_{-0.11}, \sigma_8 = 0.89^{+0.24}_{-0.20}, \chi^2 = 12.3$ (dashed-red curve).

We notice that the loss function χ^2 corresponding to GCDM stops between the Planck18 (highest) and ΛCDM (lowest) values. In this regard, one may argue based on Occam's razor that simpler models are more preferred if the complex model doesn't result in a better fit to the observation. This is basically the perspective of statistical preference. However, there is another perspective of dataset consistency whose goal is not merely to reduce the loss function but making the confidence regions of different probes overlap. ΛCDM can achieve lower χ^2 thanks to having less number of parameters and by "ignoring" the inconsistencies with other data (CMB in this case). Thus, while the standard model fits one piece of the puzzle very well, it may happen that it is missing another component which could become significant as the measurement precision increases. Here the extra parameter in GCDM may prove important to bridge the gap between early and

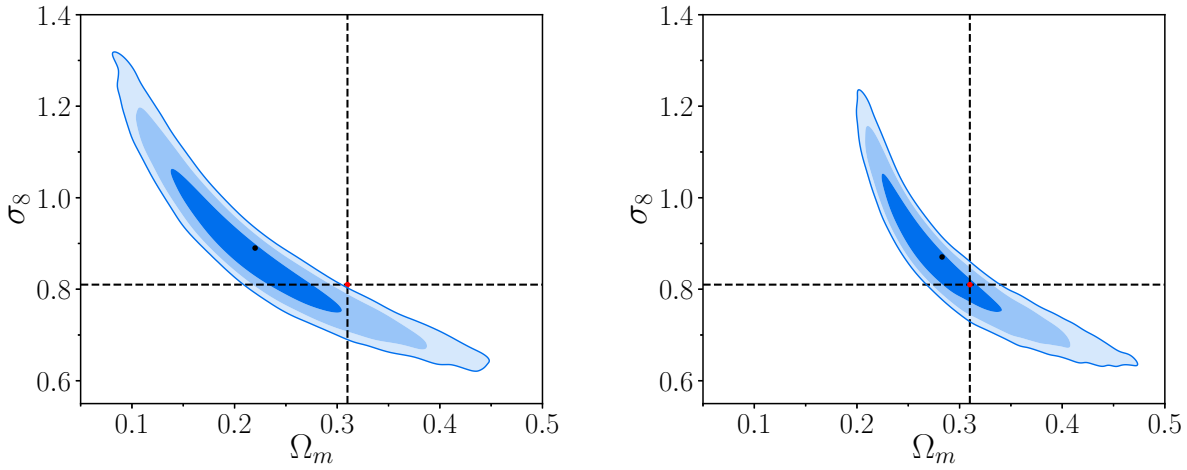

Figure 4.2: Posterior distribution for ΛCDM [left panel] and GCDM [right panel]. In both figures, the red point represents the concordance Planck18 /ΛCDM values while the black dot represents the mean value of the distribution.

late time measurements.

Another point to consider is that while GCDM includes ΛCDM as a special case ($g = 0$), we shouldn't expect that looking for the minimum χ^2 would always result in $g = 0$. The reason being that adding extra parameter makes your parameter space larger and thus "penalizes" the fit. Additionally, in higher dimensional space, the likelihood surface may contain subtle correlations between g and Ω_m, σ_8. Thus, the optimization process doesn't automatically "force" g to settle to zero unless the data strongly demands it.

We note that the scale-dependent term of Eq. 4.27, absent in ΛCDM, plays a crucial role in the structure growth, the overall effect being controlled by the slope of $G(a)$. If there is no change in the gravitational constant $\frac{dG}{da} = 0$, we don't observe any deviation in the growth from the ΛCDM predictions. However, a slight change $\frac{dG}{da} \approx 0$ can activate scale dependent growth by enhancing/suppressing it depending on the positive/negative sign of $\frac{dG}{da}$. As Fig. 4.3 shows, there is a slight change in $G(a)$ during matter domination just enough to have the right amount of structure today. Here, we should note that the term containing k^2 in Eq. 4.27 introduces a very large number and to compensate for that we require small G making it a correction term not a leading term. The choices of $n = 3$ and $m = 10$ makes G small and relieves the pressure on g to traverse bigger regions in the MCMC search for the optimal value. Initially, increasing G helps matter to clump together under gravitational pull while at around $z \approx 8$ it starts to suppresses growth by decreasing to its present value $G = G_0$. The overall effect reduces the tension level from

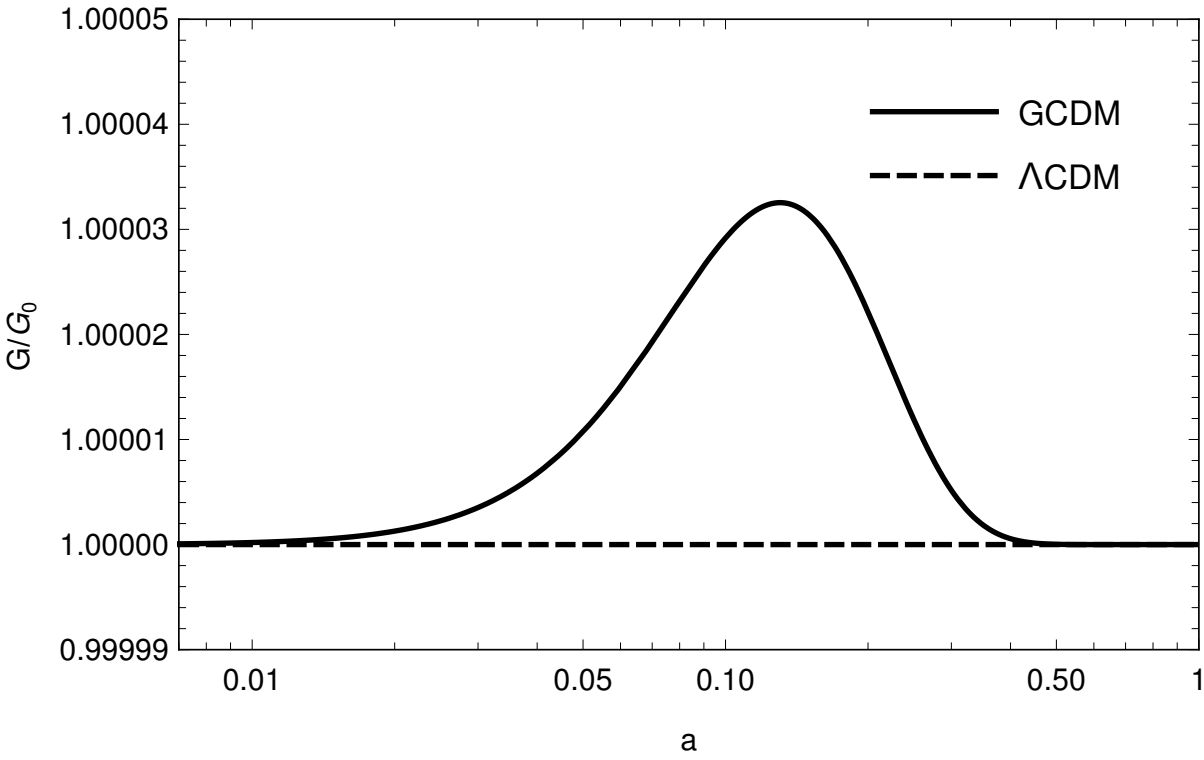

Figure 4.3: The solid line displays the variation in $G(a)$ with the best fit parameters $\Omega_{\rm m} = 0.28$, $g = 0.24$ using $n = 3$ and $m = 10$. The dashed line represents ΛCDM with $G(a) = 1$.

3σ to 1σ as shown in the left and right panels of Fig. 4.2, respectively.

4.4 Conclusion

Large scale measurements of structure growth such as, weak lensing, galaxy clustering, and RSD all exhibit hints of variations in the standard ΛCDM model predictions. The predicted value of ΛCDM based on the Planck 18 measurements show different magnitude for the strength of matter clustering on the comoving scale of $8h^{-1}$ Mpc and this problem is often called σ_8 tension. There are different ways to tackle this issue. While investigations of potential errors or biases in the data analysis is one of the approaches, modified gravity models is another active area of research.

As a first, we addressed the possible issues with the galaxy redshift measurement results by implementing dataset from Ref. [144]. These data are carefully selected against any bias which may occur due to various factors including the double counting of the same sample galaxies. Furthermore, we minimized the effects of different fiducial cosmologies using a method from Ref. [166]. This is significant as separate collaborations implemented

distinct fiducial values to determine the cosmological distances such as angular diameter distance.

The present work considers the simplest modification to GR – gravity-matter coupling, and investigates its implications on structure growth in the low-redshift universe. We derived the modified field equation containing time-varying gravitational constant, along with the background quantities, and conducted a full perturbation analysis. Proposing a parametrization for G with a single parameter, we conducted likelihood analysis. The main findings of this work suggests there is a minor dynamic in the so-called "gravitational constant" during matter domination, necessary to alleviate the σ_8 tension.

Chapter 5

Conclusion

Independent cosmological observations point unanimously to a Universe – expanding with acceleration at present and spatially flat consisting of around 70% dark energy, 26% dark matter, 4% baryons – modeled by the concordance ΛCDM model. Although, the bulk of the matter content in the universe belong to the dark sectors of this model, our limited knowledge of these components is represented in their very names – "dark" energy and "dark" matter. While crucial ingredients to the current cosmological framework, they pose pressing challenges and far-reaching questions both of theoretical origin. This thesis addresses the following questions that rest at the edge of ΛCDM validity.

- The observed dark energy Λ density is almost zero ($\sim 10^{-47}\text{GeV}^4$) in contrast to the unimaginably large number ($\sim 10^{71}\text{GeV}^4$) predicted by theory [171]. Does this hint towards a dynamical nature for dark energy? Furthermore, why does the standard model require two distinct mechanisms – inflation and dark energy – when they both serve the same purpose to explain the cosmic acceleration?

- The standard understanding suggests that dark matter is essentially the same as baryons except they are abundant compared to baryons and we can't see them with our eyes. The cold dark matter model implies that they can only interact gravitationally. If we assume distinct gravitational interactions and different evolutionary behavior for the energy density of dark matter, how tightly constrained are these assumptions?

- We have several inconsistencies between the observations and ΛCDM predictions, such as, the Hubble tension and σ_8 tension. Their persistence after several years of

data analysis may hint again to our lack of understanding of the dark sectors. Does the σ_8 tension arise from limitations in our knowledge of matter, or of gravity, or of their interplay? What would be the consequence of gravity-matter coupling on the structure growth?

In Chapter 2, we investigate the detectable signatures of α-attractor formalism that unifies two scalar fields, responsible for cosmic inflation and dark energy, as different manifestations of a single scalar field. This formalism introduces a non-trivial geometry to the field space portrayed by the Poincare disk and on the boundaries of this disk, the field potential becomes flat. So that any details of the potential are "washed away" when we approach the edges of the field space. We chose a potential that approaches one plateau (giving inflation) as an exponential and another plateau (giving dark energy) as a linear function. The advantage of this choice is twofold: the field is guaranteed to act as the thawing field, which freezes after inflation, explaining the large gap in time between the two cosmic accelerations, while linear part of the potential exhibits approximate shift symmetry giving protection against large quantum fluctuations. Pursuing this direction further, one finds the connection between the tensor-to-scalar ratio r and the asymptotic value of dark energy equation of state w_∞. Confirming via numerical analysis, we established our main result, $1 + w_0 \approx \frac{4}{3N^2 r}$ and $w_a \approx \frac{-6}{3N^2 r}$, a direct connection between thawing field dark energy and inflation observables. This is an important relation providing a "roadmap" for searching a feasible range of r and (w_0, w_a) for observation. To illustrate the impact of our findings, we can highlight several notable examples. Employing our result, Ref. [172] demonstrated that the α-attractor model outperforms the standard ΛCDM when fitted to CMB and low-redshift measurements such as BAO and SN. Likewise, the relation we found between the primordial gravitational wave and dark energy dynamics proved to be crucial in Ref. [173] when fitting α-attractor model to DESI data. Again, it leads to an improved fit over ΛCDM reinforcing the role of α-attractors as a better candidate to explain the cosmic events.

Chapter 3 studies the imprints of the deviations in dark matter clustering and equation of state on the structure growth. Preserving the early universe physics, we adopted four independent bins that span over $z = [0, 4]$. Cosmic growth is a powerful tool to probe any discrepancy from ΛCDM. However, a single redshift space distortion (RSD) measurement would not be enough in covering a wide range of redshift as $z = [0, 4]$.

Combining different RSD measurements with precisions similar to DESI, Euclid, and peculiar velocity measurements, we conducted information matrix analysis. Our findings impose $\sigma(c_i) = 0.03 - 0.14$ level constraints on the deviation in the clustering strength. While using the same four bins puts $\sigma(c_i) = 0.03 - 0.23$ level bounds on the equation of state deviations. This result shows how much dark matter can deviate from its standard behaviors predicted by ΛCDM. Although, this work provides insights into dark matter properties, it does not account for sound speed and viscous damping which occurs as a consequence of non-zero equation of state and we leave it for future work.

Chapter 4 considers the implications of a modified gravity model, with non-minimal gravity-matter coupling, on the large scale structure formation. We derived all the modified background quantities and perturbation equation. The appealing characteristic of this model is its intrinsic symmetries ensuring simplicity by canceling redundant terms. For instance, within this framework stress-energy tensor is conserved just like in general relativity (GR). Once more, we use RSD measurements for our analysis owing to its capacity to differentiate between modified gravity models and general relativity. Using a parametrization for running gravitational constant with a single parameter, we performed MCMC analysis. The result shows a significant decrease in σ_8 tension from 3σ to within 1σ. However, we note that there is a correlation between the σ_8 and H_0 tensions. Ref. [174] demonstrated that a proposal alleviating the H_0 tension ends up aggravating the σ_8 tension. However, we leave our model implications on the Hubble tension for future work.

This thesis contributes to investigations of the fundamental essence of dark sectors helping to understand the secrets of universe's most elusive components. While there still remain questions not addressed, the milestones achieved in this work may provide a stepping stone to further our understanding of the cosmos.

Appendix A

Fisher Matrix Analysis

With the onset of observational cosmology, the quality and quantity of the data are increasing very rapidly. There is a strong reason to believe that it will continue to dominate the cosmological conversations. Then, the fundamental question is how best to approach these data sets. There are two types of questions one can ask and the answers to which enable us to address this difficulty:

- Given the data, how well can we constrain our model parameters?
- Assuming a certain value for the uncertainty in the data (before collecting it), how well can we constrain our model parameters?

The answer to the first question lies at the heart of posterior distribution and it helps you investigate your theory's implications after collecting the data, in a sense, it is data-driven. The answer to the second question is at the center of Fisher matrix analysis and it can provide you with knowledge of how future experiments can constrain your parameters, in a sense, it is forecast-driven.

This section is devoted to the investigation of the Fisher matrix. The nicest thing about this approach is that it involves only the understanding of experimental design and possible noise characteristics, after which, one can extract information that a given experiment can provide about the model parameters.

In both approach, one often starts with the likelihood function,

$$L(\boldsymbol{p}) \equiv p(\mathbf{x}|\boldsymbol{p}) = \frac{1}{(2\pi)^{m/2}\sqrt{\det C(\boldsymbol{p})}} \exp\left[-\frac{1}{2}\left(\mathbf{x}-\boldsymbol{O}(\boldsymbol{p})\right)^T C(\boldsymbol{p})^{-1}\left(\mathbf{x}-\boldsymbol{O}(\boldsymbol{p})\right)\right], \quad \text{(A.1)}$$

where L tells us the probability of getting the value $\boldsymbol{x}$ given the parameter value $\boldsymbol{p}$ and m is the number of data points while $C(\boldsymbol{p})$ represents the noise matrix, lastly, $\boldsymbol{O}$ is the

observable (or model prediction). It is often more convenient to work with log-likelihood function,

$$\ln L(\boldsymbol{p}) = -\frac{1}{2}\ln\Big[(2\pi)^N \det C(\boldsymbol{p})\Big] - \frac{1}{2}\big(\mathbf{x} - \boldsymbol{O}(\boldsymbol{p})\big)^T C(\boldsymbol{p})^{-1}\big(\mathbf{x} - \boldsymbol{O}(\boldsymbol{p})\big).$$

Now, we Taylor expand the log-likelihood function around some fiducial value of the parameter $\boldsymbol{p}_0$ where the function is at its maximum, then the parameter displacement becomes

$$\delta\boldsymbol{p} = \boldsymbol{p} - \boldsymbol{p}_0, \tag{A.2}$$

allowing us to write

$$\ln L(\boldsymbol{p}) \approx \ln L(\boldsymbol{p}_0) + \frac{1}{2}\,\delta p_i\,\delta p_j\,\left.\frac{\partial^2 \ln L}{\partial p_i\,\partial p_j}\right|_{\boldsymbol{p}_0} + \dots. \tag{A.3}$$

where we neglected the first order term since it is zero at the extrema.

Now, the Fisher matrix is defined as the second order approximation to the Gaussian likelihood function,

$$F_{ij} \equiv -\left\langle \frac{\partial^2 \ln L}{\partial p_i\,\partial p_j}\right\rangle\Bigg|_{\boldsymbol{p}_0} = \left\langle \frac{\partial \ln L}{\partial p_i}\,\frac{\partial \ln L}{\partial p_j}\right\rangle\Bigg|_{\boldsymbol{p}_0}. \tag{A.4}$$

The last equality is called the Fisher identity and it comes from

$$\left\langle \frac{\partial \ln L}{\partial p}\right\rangle = \int \frac{\partial \ln L}{\partial p} L dx = \frac{\partial}{\partial p}\int L dx = \frac{\partial}{\partial p}(1) = 0, \tag{A.5}$$

where we used the fact that the total probability is equal to one. Taking another derivative yields the identity we used above. Substituting Eq. A.1 into Eq. A.4 and computing the expectation yields

$$F_{ij} = \sum_{\text{obs}} \frac{\partial O(z)}{\partial p_i}\,\mathrm{C}(z,z')^{-1}\,\frac{\partial O(z')}{\partial p_j},$$

here the derivatives are computed at the fiducial values of the parameters. If all measurements are independent of each other, i.e. there is no correlation between them then one can write $\mathrm{C}(z,z') = \sigma^2(z)\delta(z,z')$ further simplifying the expression

$$F_{ij} = \sum_{\text{obs}} \frac{\partial O(z)}{\partial p_i}\,\frac{1}{\sigma^2(z)}\,\frac{\partial O(z)}{\partial p_j}. \tag{A.6}$$

It is a symmetric matrix and obviously has the dimension equal to the number of parameters. If we have additional or prior information about certain parameter, we add it to the corresponding entry of the Fisher matrix. For example, if we know $\Omega_m = 0.3 \pm 0.02$

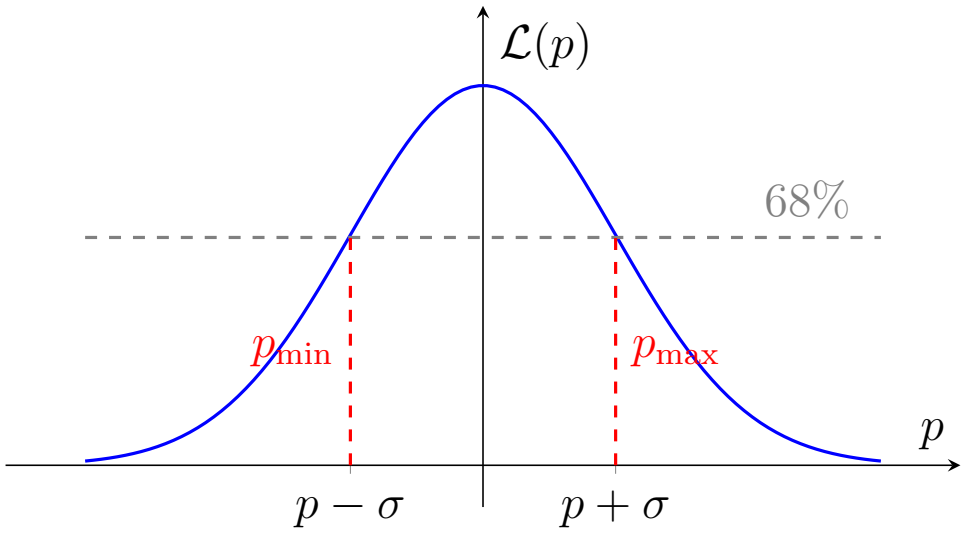

Figure A.1: Likelihood function $L = e^{-\frac{p^2}{2}}$. The gray dashed line represents 68% confidence level.

where 0.3 is the fiducial value and the uncertainty is $\sigma_{\Omega_m} = 0.02$ then we simply add it to $F_{\Omega_m\Omega_m}$. The smaller the prior in σ, the bigger the corresponding entry of the matrix – more information.

Once we determine the Fisher matrix, we can calculate the covariance matrix by simply taking the inverse $C_{ij} = F_{ij}^{-1}$. This last step is crucial since everything else will be given once we have the covariance matrix. For example, the diagonal entries of C_{ij} contains the uncertainties of each parameter while the off-diagonal terms provide the covariances between the parameters

$$\sigma(p_i) = \sqrt{C_{ii}}, \quad \text{cov}(p_i, p_j) = C_{ij}. \tag{A.7}$$

Usually, to visualize the result, we have to reduce the dimension of the covariance matrix down to 2D to obtain the confidence contours. For that purpose, we just keep the entries corresponding to the chosen parameters and remove the rest of the rows and columns. Thus, we end up with 2×2 matrix

$$C_{ij} = \begin{bmatrix} \sigma_x^2 & \sigma_{xy} \\ \sigma_{xy} & \sigma_y^2 \end{bmatrix}, \tag{A.8}$$

whose elements enable us to find the ellipse parameters

$$
\begin{aligned}
a^2 &= \frac{\sigma_x^2 + \sigma_y^2}{2} + \sqrt{\frac{(\sigma_x^2 - \sigma_y^2)^2}{4} + \sigma_{xy}^2} \\
b^2 &= \frac{\sigma_x^2 + \sigma_y^2}{2} - \sqrt{\frac{(\sigma_x^2 - \sigma_y^2)^2}{4} + \sigma_{xy}^2} \\
\tan 2\theta &= \frac{2\sigma_{xy}}{\sigma_x^2 - \sigma_y^2}
\end{aligned}
\tag{A.9}
$$

We then multiply the axis a and b by a factor α depending on the confidence level we are interested in ($\alpha = 1.52$ for 1σ level). This can effectively be understood as cutting the 3D surface of likelihood functions with a chosen confidence level. Usually, we take 68.3%, 95.4%, and 99.7% which comes from integrating the likelihood function over ranges $(p - \sigma, p + \sigma)$, $(p - 2\sigma, p + 2\sigma)$, and $(p - 3\sigma, p + 3\sigma)$, respectively. For example, in one dimension, the confidence level 68% cuts the function as a line as seen in Fig. A.1. In two dimensions, it will cut the 3D surface of the function as a plane producing the ellipse with parameters given in Eq. A.9.

Appendix B

Effective Fluid Approach

Evolved from the original Einstein's equation, the language and tools of the standard cosmology is dominated by the concept of a perfect fluid. Following this argument, it is practical to cast the modifications due to the gravity-matter coupling ξ into a perfect fluid form. The advantages of this approach are manifold: the observational compatibility, easier parametrization, and a standardized framework. However, this step comes at a cost of losing the fundamental insights into the origins of G and Λ variations. Since we don't aim to study the microscopic origins of these variables, we are content to have an exploratory model to investigate the cosmological consequences. In literature, this method is often called the effective fluid approach [175]. Below, we will "map" Eq. 4.2 into GR + DE (dark energy).

We write the r.h.s. of the modified Einstein's equation as

$$G_\mu^\nu = 8\pi G_0 T_\mu^\nu + 8\pi G_0 \left[(\frac{G}{G_0} - 1) T_\mu^\nu + \frac{\Lambda}{8\pi G_0} \delta_\mu^\nu \right] \ , \tag{B.1}$$

then identify the expression inside the square bracket as the energy-momentum tensor for the effective DE,

$$\tilde{T}_\mu^\nu = \begin{bmatrix} \rho_m \left(\frac{G(\rho)}{G_0} - 1 \right) + \frac{\Lambda}{8\pi G_0} & 0 \\ 0 & -\left[P_m \left(\frac{G(\rho)}{G_0} - 1 \right) - \frac{\Lambda}{8\pi G_0} \right] \delta_i^j \end{bmatrix} \ , \tag{B.2}$$

where ρ_m, P_m are matter energy density and pressure, respectively.

Next, we define the effective DE density and pressure from (B.2). By neglecting the matter pressure contribution P_m and using the relationship $\Lambda = \rho_\mathrm{m}(\xi - G)$ deduced from

Eq. 4.4, we obtain

$$\rho_{\rm de} = \rho_{\rm m}(\xi - 1) \ , \tag{B.3}$$

$$P_{\rm de} = -\rho_{\rm m}(\xi - \frac{G}{G_0}) \ . \tag{B.4}$$

where we used $\Lambda = \rho_{\rm m}(\xi - G)$ (from Eq. 4.4) and assumed that the matter content of the universe comprises of only dust and DE. Then the matter fractional density has a simple expression,

$$\Omega_{\rm m}(\rho_{\rm m}) = \frac{\rho_{\rm m}}{\rho_{\rm m} + \rho_{\rm de}} = \frac{1}{\xi(\rho_{\rm m})} \ , \tag{B.5}$$

while the DE equation of state is

$$w_{\rm de} = \frac{P_{\rm de}}{\rho_{\rm de}} = -1 + \frac{G(\rho_{\rm m}) - 1}{\xi(\rho_{\rm m}) - 1} \ , \tag{B.6}$$

finally, we can write the Friedmann's equations as

$$\begin{aligned} H^2 &= \frac{8\pi G_0}{3}\left(\rho_{\rm m} + \rho_{\rm de}\right) = \frac{8\pi G_0 \rho_{\rm m}}{3}\xi(\rho_{\rm m}) \ , \\ \frac{\ddot{a}}{a} &= -\frac{4\pi G_0}{3}(\rho_{\rm m} + \rho_{\rm de} + 3P_{\rm de}) = -\frac{4\pi G_0 \rho_{\rm m}}{3}(3\frac{G(\rho_{\rm m})}{G_0} - 2\xi) \ . \end{aligned} \tag{B.7}$$

These results are crucial to incorporate the GCDM parameters into the publicly available codes such as CAMB or CLASS to investigate its impact on the high redshift universe (for that we have to include radiation in our calculations, though). However, the present work focuses on the GCDM's influence on the σ_8 tension positioning these background quantities for future investigations with different goals.

Bibliography

[1] A. Einstein, "Cosmological considerations on the general theory of relativity," Cosmological Constants , 16 (1986).

[2] E. Hubble, "A relation between distance and radial velocity among extra-galactic nebulae," Proceedings of the national academy of sciences **15**, 168 (1929).

[3] G. Lemaître, "Un Univers homogène de masse constante et de rayon croissant rendant compte de la vitesse radiale des nébuleuses extra-galactiques," Annales de la Société Scientifique de Bruxelles, A47, p. 49-59 **47**, 49 (1927).

[4] A. A. Penzias and R. W. Wilson, "A measurement of excess antenna temperature at 4080 MHz," in *A Source Book in Astronomy and Astrophysics, 1900–1975* (Harvard University Press, 1979) pp. 873–876.

[5] Boggess *et al.*, "The COBE mission-Its design and performance two years after launch," Astrophysical Journal, Part 1 (ISSN 0004-637X), vol. 397, no. 2, p. 420-429. **397**, 420 (1992).

[6] C. L. Bennett *et al.*, "TheMicrowave Anisotropy ProbeMission," The Astrophysical Journal **583**, 1–23 (2003).

[7] D. N. Spergel *et al.*, "Three-Year Wilkinson Microwave Anisotropy Probe (WMAP) Observations: Implications for Cosmology," Astrophysical Journal Supplement Series **170**, 377 (2007).

[8] E. Komatsu *et al.*, "Five-Year Wilkinson Microwave Anisotropy Probe (WMAP) Observations: Cosmological Interpretation," Astrophysical Journal Supplement Series **180**, 330 (2009).

[9] P. A. R. Ade *et al.*, "Planck2013 results. I. Overview of products and scientific results," Astronomy amp; Astrophysics **571**, A1 (2014).

[10] F. J. Qu *et al.*, "The Atacama Cosmology Telescope: A Measurement of the DR6 CMB Lensing Power Spectrum and Its Implications for Structure Growth," The Astrophysical Journal **962**, 112 (2024).

[11] P. Ade *et al.*, "Improved Constraints on Primordial Gravitational Waves using Planck, WMAP, and BICEP/Keck Observations through the 2018 Observing Season," Physical Review Letters **127** (2021), 10.1103/physrevlett.127.151301.

[12] R. Chown *et al.*, "Maps of the Southern Millimeter-wave Sky from Combined 2500 deg2 SPT-SZ and Planck Temperature Data," The Astrophysical Journal Supplement Series **239**, 10 (2018).

[13] R. Croft *et al.*, "Towards a Precise Measurement of Matter Clustering: Lyman-alpha Forest Data at Redshifts 2-4," The Astrophysical Journal **581**, 20 (2002).

[14] M. Viel, M. Haehnelt, and V. Springel, "Inferring the Dark Matter Power Spectrum from the Lyman-alpha Forest in High-Resolution QSO Absorption Spectra," Monthly Notices of the Royal Astronomical Society **354**, 684 (2004).

[15] T. Jena *et al.*, "The Lyman-alpha Forest Power Spectrum from the Sloan Digital Sky Survey," Monthly Notices of the Royal Astronomical Society **361**, 70 (2005).

[16] U. Seljak *et al.*, "Cosmological Constraints from the Lyman-alpha Forest Power Spectrum and Cosmological Parameters," Physical Review D **71**, 103515 (2005).

[17] N. Dalmasso, M. Trenti, and N. Leethochawalit, "Galaxy clustering measurements out to redshift z ~ 8 from Hubble Legacy Fields," Monthly Notices of the Royal Astronomical Society **528**, 898–908 (2023).

[18] D. Bacon, R. Massey, A. Refregier, and R. Ellis, "Cosmic shear measurements as a probe of large-scale structure," Monthly Notices of the Royal Astronomical Society **344**, 673 (2003).

[19] C. Heymans *et al.*, "Cosmic shear measurements with the COMBO-17 survey," Monthly Notices of the Royal Astronomical Society **361**, 160 (2005).

[20] E. Semboloni *et al.*, "Cosmic shear analysis with the Hubble Space Telescope: A Bayesian approach," Astronomy and Astrophysics **452**, 51 (2006).

[21] A. G. Riess *et al.*, "Observational Evidence from Supernovae for an Accelerating Universe and a Cosmological Constant," The Astronomical Journal **116**, 1009 (1998).

[22] S. Perlmutter *et al.*, "Measurements of Omega and Lambda from 42 High-Redshift Supernovae," The Astrophysical Journal **517**, 565 (1999), arXiv:astro-ph/9812133 [astro-ph] .

[23] DESI Collaboration, "DESI 2024 VI: Cosmological Constraints from the Measurements of Baryon Acoustic Oscillations," (2024), arXiv:2404.03002 [astro-ph.CO] .

[24] DES Collaboration, "Dark Energy Survey: A 2.1% Measurement of the Angular Baryonic Acoustic Oscillation Scale at Redshift $z_{eff} = 0.85$ from the Final Dataset," (2024), arXiv:2401.12345 [astro-ph.CO] .

[25] A. H. Guth, "The Inflationary Universe: A Possible Solution to the Horizon and Flatness Problems," Phys. Rev. D **23**, 347 (1981).

[26] A. D. Linde, "A New Inflationary Universe Scenario: A Possible Solution of the Horizon, Flatness, Homogeneity, Isotropy and Primordial Monopole Problems," Phys. Lett. B **108**, 389 (1982).

[27] P. J. E. Peebles, "The Large-Scale Structure of the Universe," The Astronomical Journal **75**, 13 (1970).

[28] T. Zhumabek, M. Denissenya, and E. V. Linder, "Connecting primordial gravitational waves and dark energy," Journal of Cosmology and Astroparticle Physics **2023**, 013 (2023).

[29] NASA/LAMBDA, "NASA's Legacy Archive for Microwave Background Data (LAMBDA)," `https://lambda.gsfc.nasa.gov/`, accessed: 2024-11-28.

[30] N. W. S. Team, "WMAP 9-Year CMB Image," (2012), accessed: 2024-11-30.

[31] A. H. Guth, "Inflationary Universe: A Possible Solution to the Horizon and Flatness Problems," Physical Review D **23**, 347 (1981).

[32] A. Albrecht and P. J. Steinhardt, "Cosmology for Grand Unified Theories with Radiatively Induced Symmetry Breaking," Physical Review Letters **48**, 1220 (1982).

[33] A. D. Linde, "A New Inflationary Universe Scenario: A Possible Solution of the Horizon, Flatness, Homogeneity, Isotropy and Primordial Monopole Problems," Physics Letters B **108**, 389 (1982).

[34] Y. Akrami *et al.*, "Planck 2018 results. X. Constraints on inflation," Astronomy Astrophysics **641**, A10 (2020), arXiv:1807.06211 [astro-ph.CO] .

[35] P. Ade *et al.*, "BICEP2 / Keck Array X: Constraints on Primordial Gravitational Waves Using Planck, WMAP, and New BICEP2/Keck Observations through the 2015 Season," Physical Review Letters **121**, 221301 (2018), arXiv:1810.05216 [astro-ph.CO] .

[36] A. D. Linde, "Chaotic Inflation," Physics Letters B **129**, 177 (1983).

[37] D. Baumann, *Cosmology* (Cambridge University Press, 2022).

[38] M. Tristram *et al.*, "Improved constraints on the tensor-to-scalar ratio using BICEP/Keck, Planck, and other datasets," Astronomy Astrophysics **647**, A128 (2022), published May 2022., https://arxiv.org/abs/2205.05617 .

[39] S. Podariu, R. A. Daly, M. P. Mory, and B. Ratra, "Radio Galaxy Redshift-Angular Size Data Constraints on Dark Energy," The Astrophysical Journal **584**, 577 (2003).

[40] R. A. Daly and E. J. Guerra, "High-Redshift Radio Galaxies as a Cosmological Tool: Exploration of a Key Assumption and Comparison with Supernova Results," The Astronomical Journal **124**, 1831 (2002).

[41] D. Hooper and S. Dodelson, "What Can Gamma Ray Bursts Teach Us About Dark Energy?" Astroparticle Physics **27**, 113 (2007), arXiv:astro-ph/0512232 [astro-ph] .

[42] K. Xu, Y. P. Jing, G.-B. Zhao, and A. J. Cuesta, "Precise Measurement of Baryon Acoustic Oscillations as a Standard Ruler in Cosmology," Nature Astronomy **6**, 796 (2022).

[43] R. Jimenez, P. Thejll, U. Jørgensen, J. MacDonald, and B. Pagel, "Ages of Globular Clusters: A New Approach," Monthly Notices of the Royal Astronomical Society **282**, 926 (1996).

[44] H. B. Richer, B. M. S. Hansen, J. Brewer, G. G. Fahlman, M. Rich, I. Saviane, M. M. Shara, and P. B. Stetson, "The Main Sequence and Mass Function of the Globular Cluster Messier 4," The Astrophysical Journal **574**, L151 (2002).

[45] B. M. S. Hansen, H. B. Richer, J. Brewer, G. G. Fahlman, M. Rich, I. Saviane, M. M. Shara, and P. B. Stetson, "The Lower Main Sequence and Mass Function of the Globular Cluster Messier 4," The Astrophysical Journal **574**, L155 (2002).

[46] N. Aghanim *et al.* (Planck), "Planck 2018 results. VI. Cosmological parameters," Astron. Astrophys. **641**, A6 (2020), [Erratum: Astron.Astrophys. 652, C4 (2021)], arXiv:1807.06209 [astro-ph.CO] .

[47] A. G. Riess *et al.*, "A Comprehensive Measurement of the Local Value of the Hubble Constant with 1 km/s/Mpc Uncertainty from the Hubble Space Telescope and the SH0ES Team," The Astrophysical Journal **934**, L7 (2024).

[48] D. N. Spergel *et al.*, "Wilkinson Microwave Anisotropy Probe (WMAP) Three Year Results: Implications for Cosmology," The Astrophysical Journal Supplement Series **170**, 377 (2007), arXiv:astro-ph/0603449 [astro-ph] .

[49] M. Tegmark *et al.*, "Cosmological Parameters from SDSS and WMAP," Physical Review D **69**, 103501 (2004), arXiv:astro-ph/0310723 [astro-ph] .

[50] U. Seljak *et al.*, "Cosmological Parameter Analysis Including SDSS Lyα Forest and Galaxy Bias: Constraints on the Primordial Spectrum of Fluctuations, Neutrino Mass, and Dark Energy," Physical Review D **71**, 103515 (2005), arXiv:astro-ph/0407372 [astro-ph] .

[51] G. Aldering *et al.*, "Overview of the SuperNova/Acceleration Probe (SNAP)," in *Future Research Direction and Visions for Astronomy*, Vol. 4835 (SPIE, 2002) p. 146.

[52] A. Linde, "Inflation and Quantum Cosmology," in *Three Hundred Years of Gravitation*, edited by S. W. Hawking and W. Israel (Cambridge University Press, 1987) pp. 604–630.

[53] P. J. E. Peebles and A. Vilenkin, "Quintessential Inflation," Physical Review D **59**, 063505 (1999).

[54] B. Spokoiny, "Deflationary Universe Scenario," Physics Letters B **315**, 40 (1993), arXiv:gr-qc/9306008 [gr-qc] .

[55] A. Riazuelo and J.-P. Uzan, "Quintessence and Gravitational Waves," Physical Review D **62**, 083506 (2000).

[56] H. Andernach and F. Zwicky, "English and Spanish Translation of Zwicky's (1933) The Redshift of Extragalactic Nebulae," arXiv e-prints (2017), arXiv:1711.01693 [astro-ph.CO] .

[57] F. Zwicky, "On the Masses of Nebulae and of Clusters of Nebulae," The Astrophysical Journal **86**, 217 (1937).

[58] V. C. Rubin and W. K. Ford, Jr., "Rotation of the Andromeda Nebula from a Spectroscopic Survey of Emission Regions," Astrophys. J. **159**, 379 (1970).

[59] N. Dalal and A. Kravtsov, "Excluding Fuzzy Dark Matter with Sizes and Stellar Kinematics of Ultrafaint Dwarf Galaxies," Physical Review D **106**, 063517 (2022), arXiv:2203.05750 [astro-ph.CO] .

[60] T. D. Brandt, "Constraints on MACHO Dark Matter from Compact Stellar Systems in Ultra-Faint Dwarf Galaxies," The Astrophysical Journal Letters **824**, L31 (2016), arXiv:1605.03665 [astro-ph.GA] .

[61] S. D. McDermott, H.-B. Yu, and K. M. Zurek, "Turning off the Lights: How Dark is Dark Matter?" Physical Review D **83**, 063509 (2011), arXiv:1011.2907 [hep-ph] .

[62] E. V. Linder, "Testing Dark Matter Clustering with Redshift Space Distortions," Journal of Cosmology and Astroparticle Physics **2013**, 031 (2013), arXiv:1302.4754 [astro-ph.CO] .

[63] T. Zhumabek, M. Denissenya, and E. V. Linder, "Model independent dark matter properties from cosmic growth," Journal of Cosmology and Astroparticle Physics **2024**, 018 (2024).

[64] T. Zhumabek, A. Mukhamediya, H. Chakrabarty, and D. Malafarina, "Running gravitational constant induced dark energy as a solution to σ_8 tension," (2024), arXiv:2411.05965 [astro-ph.CO] .

[65] R. Kallosh and A. Linde, "Universality Class in Conformal Inflation," JCAP **07**, 002 (2013), arXiv:1306.5220 [hep-th] .

[66] R. Kallosh, A. Linde, and D. Roest, "Superconformal Inflationary α-Attractors," JHEP **11**, 198 (2013), arXiv:1311.0472 [hep-th] .

[67] M. Galante, R. Kallosh, A. Linde, and D. Roest, "Unity of Cosmological Inflation Attractors," Phys. Rev. Lett. **114**, 141302 (2015), arXiv:1412.3797 [hep-th] .

[68] E. V. Linder, "Dark energy from α-attractors," Physical Review D **91** (2015), 10.1103/physrevd.91.123012, arXiv:1505.00815 [astro-ph.CO] .

[69] M. Braglia, W. T. Emond, F. Finelli, A. E. Gümrükçüoğlu, and K. Koyama, "Unified framework for early dark energy from α-attractors," Physical Review D **102** (2020), 10.1103/physrevd.102.083513, arXiv:2005.14053 [astro-ph.CO] .

[70] K. Dimopoulos and C. Owen, "Quintessential Inflation with α-attractors," JCAP **06**, 027 (2017), arXiv:1703.00305 [gr-qc] .

[71] K. Dimopoulos, L. Donaldson Wood, and C. Owen, "Instant preheating in quintessential inflation with α-attractors," Phys. Rev. D **97**, 063525 (2018), arXiv:1712.01760 [astro-ph.CO] .

[72] Y. Akrami, R. Kallosh, A. Linde, and V. Vardanyan, "Dark energy, α-attractors, and large-scale structure surveys," JCAP **2018**, 041 (2018), arXiv:1712.09693 [hep-th] .

[73] C. García-García, E. V. Linder, P. Ruíz-Lapuente, and M. Zumalacárregui, "Dark energy from α-attractors: phenomenology and observational constraints," JCAP **08**, 022 (2018), arXiv:1803.00661 [astro-ph.CO] .

[74] Y. Akrami, S. Casas, S. Deng, and V. Vardanyan, "Quintessential α-attractor inflation: forecasts for Stage IV galaxy surveys," JCAP **2021**, 006 (2021), arXiv:2010.15822 [astro-ph.CO] .

[75] L. Aresté Saló, D. Benisty, E. I. Guendelman, and J. de Haro, "α-attractors in quintessential inflation motivated by supergravity," Phys. Rev. D **103**, 123535 (2021), arXiv:2103.07892 [astro-ph.CO] .

[76] K. Dimopoulos, "Jointly modelling Cosmic Inflation and Dark Energy," J. Phys. Conf. Ser. **2105**, 012001 (2021), arXiv:2106.14966 [gr-qc] .

[77] W. Giarè, S. Pan, E. Di Valentino, W. Yang, J. de Haro, and A. Melchiorri, "Inflationary potential as seen from different angles: model compatibility from multiple CMB missions," Journal of Cosmology and Astroparticle Physics **2023**, 019 (2023).

[78] R. de Putter and E. V. Linder, "Calibrating dark energy," JCAP **2008**, 042 (2008), arXiv:0808.0189 [astro-ph] .

[79] Y. Tang and Y.-L. Wu, "Conformal -attractor inflation with Weyl gauge field," Journal of Cosmology and Astroparticle Physics **2020**, 067–067 (2020).

[80] D. F. Carneiro, E. A. Freiras, B. Gonçalves, A. G. de Lima, and I. L. Shapiro, "On Useful Conformal Tranformations In General Relativity," (2023), arXiv:gr-qc/0412113 [gr-qc] .

[81] R. Kallosh, A. Linde, and D. Roest, "Large field inflation and double -attractors," Journal of High Energy Physics **2014** (2014), 10.1007/jhep08(2014)052.

[82] C. T. Hill and G. G. Ross, "Gravitational contact interactions and the physical equivalence of Weyl transformations in effective field theory," Physical Review D **102** (2020), 10.1103/physrevd.102.125014.

[83] R. Kallosh, A. Linde, and D. Roest, "Large field inflation and double α-attractors," JHEP **08**, 052 (2014), arXiv:1405.3646 [hep-th] .

[84] S. Ferrara and R. Kallosh, "Seven-disk manifold, α-attractors, and B modes," Phys. Rev. D **94**, 126015 (2016), arXiv:1610.04163 [hep-th] .

[85] R. Kallosh, A. Linde, T. Wrase, and Y. Yamada, "Maximal Supersymmetry and B-Mode Targets," JHEP **04**, 144 (2017), arXiv:1704.04829 [hep-th] .

[86] R. Kallosh and A. Linde, "Dark energy and the fate of the Universe," Journal of Cosmology and Astroparticle Physics **2003**, 002–002 (2003).

[87] J. Martin, C. Ringeval, and V. Vennin, "Encyclopedia Inflationaris," Phys. Dark Univ. **5-6**, 75 (2014), arXiv:1303.3787 [astro-ph.CO] .

[88] B. Broy, M. Galante, D. Roest, and A. Westphal, "Pole inflation — Shift symmetry and universal corrections," Journal of High Energy Physics **2015**, 1–18 (2015).

[89] E. Allys *et al.* (LiteBIRD), "Probing Cosmic Inflation with the LiteBIRD Cosmic Microwave Background Polarization Survey," PTEP **2023**, 042F01 (2023), arXiv:2202.02773 [astro-ph.IM] .

[90] E. J. Copeland, M. Sami, and S. Tsujikawa, "Dynamics of dark energy," International Journal of Modern Physics D **15**, 1753 (2006), arXiv:hep-th/0603057 .

[91] R. R. Caldwell and E. V. Linder, "Limits of Quintessence," Physical Review Letters **95** (2005), 10.1103/physrevlett.95.141301, arXiv:astro-ph/0505494 .

[92] E. V. Linder, "Paths of quintessence," Physical Review D **73** (2006), 10.1103/physrevd.73.063010, arXiv:astro-ph/0601052 .

[93] E. V. Linder, "Exploring the Expansion History of the Universe," Physical Review Letters **90** (2003), 10.1103/physrevlett.90.091301, arXiv:astro-ph/0208512 .

[94] A. Aghamousa *et al.* (DESI), "The DESI Experiment Part I: Science,Targeting, and Survey Design," (2016), arXiv:1611.00036 [astro-ph.IM] .

[95] R. Mandelbaum *et al.* (LSST Dark Energy Science), "The LSST Dark Energy Science Collaboration (DESC) Science Requirements Document," (2018), arXiv:1809.01669 [astro-ph.CO] .

[96] K. Abazajian *et al.*, "CMB-S4 Science Case, Reference Design, and Project Plan," (2019), arXiv:1907.04473 [astro-ph.IM] .

[97] A. Blanchard *et al.* (Euclid), "Euclid preparation: VII. Forecast validation for Euclid cosmological probes," Astron. Astrophys. **642**, A191 (2020), arXiv:1910.09273 [astro-ph.CO] .

[98] N. Aghanim *et al.* (Planck), "Planck 2018 results. VI. Cosmological parameters," Astron. Astrophys. **641**, A6 (2020), arXiv:1807.06209 [astro-ph.CO] .

[99] D. Clowe, M. Bradač, A. H. Gonzalez, M. Markevitch, S. W. Randall, C. Jones, and D. Zaritsky, "A Direct Empirical Proof of the Existence of Dark Matter," The Astrophysical Journal **648**, L109–L113 (2006), arXiv:astro-ph/0608407 .

[100] N. Aghanim *et al.*, "Planck 2018 results: VI. Cosmological parameters," Astronomy and Astrophysics **641**, A6 (2020), arXiv:1807.06209 [astro-ph.CO] .

[101] L. Baudis and S. Profumo, "Dark Matter in R. L. Workman et al., (Particle Data Group), Review of Particle Physics," PTEP **2022**, 083C01 (2022), `https://pdg.lbl.gov/2023/reviews/rpp2022-rev-dark-matter.pdf`.

[102] R. H. Wechsler and J. L. Tinker, "The Connection Between Galaxies and Their Dark Matter Halos," Annual Review of Astronomy and Astrophysics **56**, 435–487 (2018), arXiv:1804.03097 [astro-ph.CO] .

[103] E. Di Valentino, O. Mena, S. Pan, L. Visinelli, W. Yang, A. Melchiorri, D. F. Mota, A. G. Riess, and J. Silk, "In the realm of the Hubble tension—a review of solutions," Classical and Quantum Gravity **38**, 153001 (2021), arXiv:2103.01183 [astro-ph.CO] .

[104] A. Ashoorioon and Z. Davari, "Dark Matter Cosmology with Varying Viscosity: A Possible Resolution to the S_8 Tension," The Astrophysical Journal **959**, 120 (2023), arXiv:2303.06627 [astro-ph.CO] .

[105] P. Arabameri, Z. Davari, and N. Khosravi, "$k-$Dependent Dark Matter," arXiv:2307.08495 [hep-ph] .

[106] K. Naidoo, "Signs of a non-zero equation-of-state for Dark Matter," arXiv:2308.13617 [astro-ph.CO] .

[107] A. Lapi, L. Boco, M. M. Cueli, B. S. Haridasu, T. Ronconi, C. Baccigalupi, and L. Danese, "Little Ado about Everything: ηCDM, a Cosmological Model with Fluctuation-driven Acceleration at Late Times," Astrophys. J. **959**, 83 (2023), arXiv:2310.06028 [astro-ph.CO] .

[108] W. Hu, "Structure Formation with Generalized Dark Matter," The Astrophysical Journal **506**, 485–494 (1998), arXiv:astro-ph/9801234 .

[109] K. Naidoo, M. Jaber, W. A. Hellwing, and M. Bilicki, "Dark matter solution to the H_0 and S_8 tensions, and the integrated Sachs-Wolfe void anomaly," Phys. Rev. D **109**, 083511 (2024).

[110] V. Yadav, S. K. Yadav, and A. K. Yadav, "Observational Constraints on generalized dark matter properties in the presence of neutrinos with the final Planck release," Phys. Dark Univ. **42**, 101363 (2023), arXiv:2307.05155 [astro-ph.CO] .

[111] M. Meiers, L. Knox, and N. Schöneberg, "Exploration of the Pre-recombination Universe with a High-Dimensional Model of an Additional Dark Fluid," Phys. Rev. D **108**, 103527 (2023), arXiv:2307.09522 [astro-ph.CO] .

[112] E. V. Linder, "Testing dark matter clustering with redshift space distortions," Journal of Cosmology and Astroparticle Physics **2013**, 031 (2013), arXiv:1302.4754 [astro-ph.CO] .

[113] M. Denissenya and E. V. Linder, "Cosmic growth signatures of modified gravitational strength," Journal of Cosmology and Astroparticle Physics **2017**, 030 (2017), arXiv:1703.00917 [astro-ph.CO] .

[114] Euclid Collaboration *et al.*, "Euclid preparation: VII. Forecast validation for Euclid cosmological probes," Astronomy and Astrophysics **642**, A191 (2020), arXiv:1910.09273 [astro-ph.CO] .

[115] A. G. Kim and E. V. Linder, "Complementarity of peculiar velocity surveys and redshift space distortions for testing gravity," Physical Review D **101**, 023516 (2020), arXiv:1911.09121 [astro-ph.CO] .

[116] A. Palmese and A. G. Kim, "Probing gravity and growth of structure with gravitational waves and galaxies' peculiar velocity," Physical Review D **103**, 103507 (2021), arXiv:2005.04325 [astro-ph.CO] .

[117] C. Saulder *et al.*, "Target selection for the DESI Peculiar Velocity Survey," Monthly Notices of the Royal Astronomical Society **525**, 1106–1125 (2023), arXiv:2302.13760 [astro-ph.CO] .

[118] C. M. Müller, "Cosmological bounds on the equation of state of dark matter," Physical Review D **71**, 047302 (2005), arXiv:astro-ph/0410621 .

[119] C. Armendariz-Picon and J. T. Neelakanta, "How cold is cold dark matter?" Journal of Cosmology and Astroparticle Physics **2014**, 049 (2014), arXiv:1309.6971 [astro-ph.CO] .

[120] D. B. Thomas, M. Kopp, and C. Skordis, "Constraining the properties of dark matter with observations of the cosmic microwave background," The Astrophysical Journal **830**, 155 (2016), arXiv:1601.05097 [astro-ph.CO] .

[121] M. Kopp, C. Skordis, D. B. Thomas, and S. Ilić, "Dark Matter Equation of State through Cosmic History," Physical Review Letters **120**, 221102 (2018), arXiv:1802.09541 [astro-ph.CO] .

[122] S. Ilić, M. Kopp, C. Skordis, and D. B. Thomas, "Dark matter properties through cosmic history," Physical Review D **104**, 043520 (2021), arXiv:2004.09572 [astro-ph.CO] .

[123] E. V. Linder and R. N. Cahn, "Parameterized beyond-Einstein growth," Astroparticle Physics **28**, 481–488 (2007), arXiv:astro-ph/0701317 .

[124] D. J. Schlegel *et al.*, "The MegaMapper: a stage-5 spectroscopic instrument concept for the study of inflation and dark energy," arXiv:2209.04322 [astro-ph.IM] .

[125] D. J. Schlegel *et al.* (DESI), "A spectroscopic road map for cosmic frontier: DESI, DESI-II, stage-5," arXiv:2209.03585 [astro-ph.CO] .

[126] E. Aubourg *et al.* (BOSS), "Cosmological implications of baryon acoustic oscillation measurements," Phys. Rev. D **92**, 123516 (2015), arXiv:1411.1074 [astro-ph.CO] .

[127] T. Delubac *et al.* (BOSS), "Baryon acoustic oscillations in the Lyα forest of BOSS DR11 quasars," Astron. Astrophys. **574**, A59 (2015), arXiv:1404.1801 [astro-ph.CO] .

[128] E. Baxter *et al.*, "Joint measurement of lensing–galaxy correlations using SPT and DES SV data," Mon. Not. Roy. Astron. Soc. **461**, 4099 (2016), arXiv:1602.07384 [astro-ph.CO] .

[129] A. A. Starobinsky, "A New Type of Isotropic Cosmological Models Without Singularity," Phys. Lett. B **91**, 99 (1980).

[130] E. Abdalla *et al.*, "Cosmology intertwined: A review of the particle physics, astrophysics, and cosmology associated with the cosmological tensions and anomalies," JHEAp **34**, 49 (2022), arXiv:2203.06142 [astro-ph.CO] .

[131] C. Heymans *et al.*, "CFHTLenS tomographic weak lensing cosmological parameter constraints: Mitigating the impact of intrinsic galaxy alignments," Mon. Not. Roy. Astron. Soc. **432**, 2433 (2013), arXiv:1303.1808 [astro-ph.CO] .

[132] E. Macaulay, I. K. Wehus, and H. K. Eriksen, "Lower Growth Rate from Recent Redshift Space Distortion Measurements than Expected from Planck," Phys. Rev. Lett. **111**, 161301 (2013), arXiv:1303.6583 [astro-ph.CO] .

[133] S. Alam *et al.* (BOSS), "The clustering of galaxies in the completed SDSS-III Baryon Oscillation Spectroscopic Survey: cosmological analysis of the DR12 galaxy sample," Mon. Not. Roy. Astron. Soc. **470**, 2617 (2017), arXiv:1607.03155 [astro-ph.CO] .

[134] R. C. Nunes and S. Vagnozzi, "Arbitrating the S8 discrepancy with growth rate measurements from redshift-space distortions," Mon. Not. Roy. Astron. Soc. **505**, 5427 (2021), arXiv:2106.01208 [astro-ph.CO] .

[135] R. A. Battye, T. Charnock, and A. Moss, "Tension between the power spectrum of density perturbations measured on large and small scales," Phys. Rev. D **91**, 103508 (2015), arXiv:1409.2769 [astro-ph.CO] .

[136] N. MacCrann, J. Zuntz, S. Bridle, B. Jain, and M. R. Becker, "Cosmic Discordance: Are Planck CMB and CFHTLenS weak lensing measurements out of tune?" Mon. Not. Roy. Astron. Soc. **451**, 2877 (2015), arXiv:1408.4742 [astro-ph.CO] .

[137] M. Lucca, "Dark energy–dark matter interactions as a solution to the S8 tension," Phys. Dark Univ. **34**, 100899 (2021), arXiv:2105.09249 [astro-ph.CO] .

[138] V. Poulin, J. L. Bernal, E. D. Kovetz, and M. Kamionkowski, "Sigma-8 tension is a drag," Phys. Rev. D **107**, 123538 (2023), arXiv:2209.06217 [astro-ph.CO] .

[139] E. Di Valentino, A. Melchiorri, O. Mena, and S. Vagnozzi, "Nonminimal dark sector physics and cosmological tensions," Phys. Rev. D **101**, 063502 (2020), arXiv:1910.09853 [astro-ph.CO] .

[140] M. Asghari, J. Beltrán Jiménez, S. Khosravi, and D. F. Mota, "On structure formation from a small-scales-interacting dark sector," JCAP **04**, 042 (2019), arXiv:1902.05532 [astro-ph.CO] .

[141] J. Beltrán Jiménez, D. Bettoni, D. Figueruelo, F. A. Teppa Pannia, and S. Tsujikawa, "Probing elastic interactions in the dark sector and the role of S8," Phys. Rev. D **104**, 103503 (2021), arXiv:2106.11222 [astro-ph.CO] .

[142] J. B. Jiménez, D. Bettoni, D. Figueruelo, and F. A. Teppa Pannia, "On Evidence for Elastic Interactions in the Dark Sector," (2024), arXiv:2410.18645 [astro-ph.CO] .

[143] J. Hamann and J. Hasenkamp, "A new life for sterile neutrinos: resolving inconsistencies using hot dark matter," JCAP **10**, 044 (2013), arXiv:1308.3255 [astro-ph.CO] .

[144] S. Nesseris, G. Pantazis, and L. Perivolaropoulos, "Tension and constraints on modified gravity parametrizations of $G_{\rm eff}(z)$ from growth rate and Planck data," Phys. Rev. D **96**, 023542 (2017).

[145] E. N. Saridakis, "Solving both H_0 and σ_8 tensions in $f(T)$ gravity," (2023), arXiv:2301.06881 [gr-qc] .

[146] L. Heisenberg, H. Villarrubia-Rojo, and J. Zosso, "Can late-time extensions solve the H0 and σ8 tensions?" Phys. Rev. D **106**, 043503 (2022), arXiv:2202.01202 [astro-ph.CO] .

[147] M. A. Markov and V. F. Mukhanov, "De Sitter initial state of the universe and asymptotic freedom," JETP Lett. **40**, 1043 (1984).

[148] A. Zholdasbek, H. Chakrabarty, D. Malafarina, and A. Bonanno, "An emergent cosmological model from running Newton constant," (2024), arXiv:2405.02636 [gr-qc] .

[149] J. Hou, J. Bautista, M. Berti, C. Cuesta-Lazaro, C. Hernández-Aguayo, T. Tröster, and J. Zheng, "Cosmological probes of structure growth and tests of gravity," Universe **9**, 302 (2023).

[150] J. G. Williams, S. G. Turyshev, and D. H. Boggs, "Progress in Lunar Laser Ranging Tests of Relativistic Gravity," Phys. Rev. Lett. **93**, 261101 (2004).

[151] C. Bambi, M. Giannotti, and F. L. Villante, "Response of primordial abundances to a general modification of $G_{\rm N}$ and/or of the early universe expansion rate," Physical Review D **71** (2005), 10.1103/physrevd.71.123524.

[152] Y.-S. Song and W. J. Percival, "Reconstructing the history of structure formation using redshift distortions," Journal of Cosmology and Astroparticle Physics **2009**, 004–004 (2009).

[153] D. Huterer, D. L. Shafer, D. M. Scolnic, and F. Schmidt, "Testing ΛCDM at the lowest redshifts with SN Ia and galaxy velocities," Journal of Cosmology and Astroparticle Physics **2017**, 015–015 (2017).

[154] S. J. Turnbull, M. J. Hudson, H. A. Feldman, M. Hicken, R. P. Kirshner, and R. Watkins, "Cosmic flows in the nearby universe from Type Ia supernovae: Cosmic flows from SNIa," Monthly Notices of the Royal Astronomical Society **420**, 447–454 (2011).

[155] M. J. Hudson and S. J. Turnbull, "The growth rate of cosmic structure from peculiar velocities at low and high redshifts," The Astrophysical Journal **751**, L30 (2012).

[156] M. Davis, A. Nusser, K. L. Masters, C. Springob, J. P. Huchra, and G. Lemson, "Local gravity versus local velocity: solutions for β and non-linear bias: Gravity versus velocity," Monthly Notices of the Royal Astronomical Society **413**, 2906–2922 (2011).

[157] M. Feix, A. Nusser, and E. Branchini, "Growth Rate of Cosmological Perturbations at $z \sim 0.1$ from a New Observational Test," Physical Review Letters **115** (2015), 10.1103/physrevlett.115.011301.

[158] C. Howlett, A. J. Ross, L. Samushia, W. J. Percival, and M. Manera, "The clustering of the SDSS main galaxy sample – II. Mock galaxy catalogues and a measurement of the growth of structure from redshift space distortions at z = 0.15," Monthly Notices of the Royal Astronomical Society **449**, 848–866 (2015).

[159] C. Blake *et al.*, "Galaxy And Mass Assembly (GAMA): improved cosmic growth measurements using multiple tracers of large-scale structure," Monthly Notices of the Royal Astronomical Society **436**, 3089–3105 (2013).

[160] L. Samushia, W. J. Percival, and A. Raccanelli, "Interpreting large-scale redshift-space distortion measurements: Large-scale redshift-space distortions," Monthly Notices of the Royal Astronomical Society **420**, 2102–2119 (2012).

[161] A. G. Sánchez *et al.*, "The clustering of galaxies in the SDSS-III Baryon Oscillation Spectroscopic Survey: cosmological implications of the full shape of the clustering wedges in the data release 10 and 11 galaxy samples," Monthly Notices of the Royal Astronomical Society **440**, 2692–2713 (2014).

[162] C.-H. Chuang *et al.*, "The clustering of galaxies in the SDSS-III Baryon Oscillation Spectroscopic Survey: single-probe measurements from CMASS anisotropic galaxy clustering," Monthly Notices of the Royal Astronomical Society **461**, 3781–3793 (2016).

[163] C. Blake *et al.*, "The WiggleZ Dark Energy Survey: joint measurements of the expansion and growth history at $z < 1$: WiggleZ Survey: expansion history," Monthly Notices of the Royal Astronomical Society **425**, 405–414 (2012).

[164] A. Pezzotta *et al.*, "The VIMOS Public Extragalactic Redshift Survey (VIPERS) - The growth of structure at $0.5 < z < 1.2$ from redshift-space distortions in the clustering of the PDR-2 final sample," Astronomy & Astrophysics **604**, A33 (2017).

[165] T. Okumura *et al.*, "The Subaru FMOS galaxy redshift survey (FastSound). IV. New

constraint on gravity theory from redshift space distortions at z $\sim$ 1.4," Publications of the Astronomical Society of Japan **68** (2016), 10.1093/pasj/psw029.

[166] E. Macaulay, I. K. Wehus, and H. K. Eriksen, "Lower Growth Rate from Recent Redshift Space Distortion Measurements than Expected from Planck," Physical Review Letters **111** (2013), 10.1103/physrevlett.111.161301.

[167] D. Foreman-Mackey, D. W. Hogg, D. Lang, and J. Goodman, "emcee: The MCMC Hammer," PASP **125**, 306 (2013), 1202.3665 .

[168] A. Lewis, "GetDist: a Python package for analysing Monte Carlo samples," (2019), arXiv:1910.13970 [astro-ph.IM] .

[169] W. Zhang, C. Cheng, Q. Huang, M. Li, S. Li, X. Li, and S. Wang, "Testing modified gravity models with recent cosmological observations," Science China Physics, Mechanics and Astronomy **55**, 2244–2258 (2012).

[170] R. Arjona, W. Cardona, and S. Nesseris, "Designing Horndeski and the effective fluid approach," Physical Review D **100** (2019), 10.1103/physrevd.100.063526.

[171] S. Weinberg, "The cosmological constant problem," Rev. Mod. Phys. **61**, 1 (1989).

[172] W. Giarè, E. Di Valentino, E. V. Linder, and E. Specogna, "Testing α-attractor quintessential inflation against CMB and low-redshift data," Phys. Dark Univ. **46**, 101713 (2024), arXiv:2402.01560 [astro-ph.CO] .

[173] G. Alestas, M. Caldarola, S. Kuroyanagi, and S. Nesseris, "DESI constraints on α-attractor inflationary models," (2024), arXiv:2410.00827 [astro-ph.CO] .

[174] E. Di Valentino *et al.*, "Cosmology Intertwined III: $f\sigma_8$ and S_8," Astropart. Phys. **131**, 102604 (2021), arXiv:2008.11285 [astro-ph.CO] .

[175] W. Cardona, R. Arjona, A. Estrada, and S. Nesseris, "Cosmological constraints with the Effective Fluid approach for Modified Gravity," Journal of Cosmology and Astroparticle Physics **2021**, 064 (2021).